UNIVERSIDADE DA BEIRA INTERIOR
Engenharia

The influence of jet fuels on the emission of pollutants

Inês Isabel Ascenção Costa Morão

Dissertação para obtenção do Grau de Mestre em
Engenharia Aeronáutica
(Ciclo de Estudos Integrado)

Orientador: Prof. Doutor Francisco Miguel Ribeiro Proença Brójo

Covilhã, outubro de 2019

Dedication

To my parents and brother, for their encouragement, patience, affection and faith, without them I could not have completed this course.

Acknowledgements

Thank you to my parents for all the kind words in difficult moments and all the support that they gave me. There are no words in the world to express how thankful I am.

My deepest thank you to my supervisor, Professor Dr Francisco Brójo. I am forever grateful for all the advises and knowledge transmitted, patience and encouragement which always demonstrated, but mainly the availability to this study.

Resumo

No presente trabalho foi realizada uma simulação de CFD, sendo o componente de estudo uma câmara de combustão do motor CFM56-3. Simulou-se a combustão e analisou-se as emissões de poluentes de diferentes combustíveis (Jet A, Jet B e TS-1).

Sendo este um estudo de continuidade, foi usado o CAD elaborado por Jonas Oliveira. Para a elaboração da malha o usado o software HELYX-OS e para o cálculo numérico foi utilizado o ANSYS Fluent 16.2.

O modelo viscoso usado foi Large Eddy Simulation (LES). Este modelo é mais eficiente que os outros modelos para perceber o processo de formação dos poluentes. A atomização foi considerada neste estudo.

Conclui-se que, entre todos os combustíveis simulados, com o aumento da potência as emissões de NO_x aumentaram também. Verificou-se um comportamento errático nas emissões de UHC e *CO*, devido ao facto de se ter utilizado um modelo empírico e não um modelo químico detalhado.

O combustível que apresentou os melhores resultados ao longo de todo o ciclo de potência da ICAO, com respeito às emissões NO_x e UHC, foi o Jet B, uma vez que foi previsto valores de emissões inferiores, quando comparados com os restantes combustíveis. Jet A apresentou os valores mais baixos de emissões de *CO* em cruzeiro, aproximação e taxi.

TS-1 apresentou os valores mais baixos de emissões de CO_2 ao longo do ciclo LTO da ICAO.

Palavras-chave

CFM56-3, Câmara de combustão, Emissão de poluentes, Jet Fuel, CFD, HELYX-OS, ANSYS Fluent

Abstract

In the present work a CFD simulation was performed, the study component was a CFM56-3 combustor. It was intended to simulate the combustion and emission of pollutants from the different jet fuels (Jet A, Jet B and TS-1), when burning these through ICAO's LTO cycle.
Being this a continuity study, the CAD made by Jonas Oliveira was used. The mesh was constructed with HELYX-OS software and the numerical study was made using the commercial software ANSYS Fluent 16.2.
Large Eddy Simulation (LES) was used as viscous model. This model is a more efficient than other models to better understand the processes of pollutant formation and to provide their quantitative prediction. The atomization was considered in this study.
It can be concluded, amongst all the fuels simulated that increasing the power produces higher NOx. There was also an erratic behaviour in the emissions of UHC and *CO* results, because an empiric model was used and not a detailed chemical model.
The jet fuel that presented the best performance in ICAO's LTO cycle regarding NO_x and UHC emissions was Jet B, as these emissions were lower when compared to all the fuels. Jet A presented the lowest emissions of *CO* at cruise, approach and idle.
TS-1 presented the lowest emissions of CO_2 throughout the entire ICAO´s LTO cycle.

Keywords

CFM56-3, Combustion Chamber, Emission Pollutants, Jet Fuel, CFD, HELYX-OS, ANSYS Fluent

Contents

List of Figures

List of Tables

List of Acronyms

ACARE	Advisory Council for Aviation Research and Innovation in Europe
AFR	Air-fuel ratios
AGB	Accessory Gear Box
APU	Auxiliary power unit
ARC	Analytically Reduced Chemistry
BAM	Beta-attenuation mass monitor
CAD	Computer-Aided Design
CAEP	Committee on Aviation Environmental Protection
CC	Combustor Chamber
CFD	Computational Fluid Dynamics
CFL	Courant-Friedrichs-Levy
CPC	Condensation particle counter
CPU	Central processing unit
Da	Damkohler number
DAC	Dual Annular Combustor
DES	Detached eddy simulation
DMA	Differential mobility analyser
DNS	Direct Numerical Simulation
DO	Discrete Ordinates
EI	Emission index
ELPI	Electrical low-pressure impactor
EFC	Engine Flight Cycles
EFH	Engine Flight Hours
ERF	Explicit Relaxation Factor
FAR	Fuel-to-air ratios
FID	Flame ionization detector
FSRFL	Fuel Stream Rich Flammability Limit
FTIR	Fourier transform infrared spectroscopy
GC	Gas chromatography
GE	General Electric
GHG	Greenhouse Gas
GTC	Gas Turbine Combustor
GTE	Gas turbine engine
HDS	Horizontal Drive Shaft
HHV	Higher heating value
HPC	High-pressure compressor
HPT	High-pressure turbine

ICAO	International Civil Aviation Organization
IGB	Inlet Gear Box
IGV	Inlet Guide Vanes
LEC	Low emission combustor
LES	Large eddy simulation
LHV	Low heating value
LPC	Low-pressure compressor
LPT	Low-pressure turbine
LTO	Landing and take-off
MAAP	Multi-angle absorption photometer
NASA	National Aeronautics and Space Administration
Oh	Ohneserge Number
OGV	Outlet Guide Vanes
OP-FTIR	Open-path Fourier transform infrared spectroscopy
OPR	Overall Pressure Ratio
P&W	Pratt and Whittney
PDF	Probability Density Function
PLF	Pressure low factor
PRESTO!	PREssure STaggering Option
PZ	Primary Zone
RAM	Random Access Memory
RANS	Reynolds Averaged Navier-Stokes
RNG	Renormalization group
RSM	Reynolds Stress Model
RQL	Rich-Quench-Lean
SCS	Surface Cell Size
SFC	Specific Fuel Consumption
SGS	Sub-grid scale
SIMPLE	Semi-Implicit Method for Pressure Linked Equations
SMD	Sauter mean diameter
SMPS	Scanning mobility particle sizer spectrometer
SN	Smoke Number
STL	Stereo Lithography
SST	Shear-stress transport
TAP	Transportes Aéreos Portugueses
TAPS	Twin Annular Premixing Swirler
TDLAS	Tunable diode laser absorption spectroscopy
TFLES	Thickened Flame model
TGB	Transfer Gear Box
TILDAS	Tunable infrared differential absorption spectroscopy

TIM	Time- in- mode
TTQ	Temperature Traverse Quality
UBI	Universidade da Beira Interior
UHC	Unburned hydrocarbons
USA	United States of America
URF	Under Relaxation Factor
VBV	Variable Bleed Valves
VOC	Volatile organic compounds

Nomenclature

$\frac{1}{2}v^2$	Mass specific system kinetic energy	$[J/kg]$
A	Area	$[m^2]$
C	Heat capacity	$[J/K]$
C_μ	$k-\varepsilon$ model constant	[-]
c_p	Specific heat at constant pressure	$[J/kg.K]$
C_D	Discharge coefficient	[-]
D	Drop diameter	[m]
d_0	Discharge orifice diameter	[m]
F	Engine thrust	$[kN]$
F_{00}	Engine take-off thrust	$[kN]$
gz	Mass-specific system potential energy	$[J]$
H/C	Hydrogen to carbon ratio	[-]
L	Characteristic length	[m]
m	Mass	$[kg]$
$\dot{m}$	Mass flow rate	$[kg/s]$
M	Molecular weight	$[kg/kmol]$
n	Number of moles in a gas	$[kmol]$
n_{fuel}	Moles of fuel combusted	$[kmol]$
n_l	Number of layers	[-]
n_{water}	Moles of water vaporized	$[kmol]$
p	Pressure	$[Pa]$
Q	Heat transfer	$[W]$
q_{cv}	Heat transferred across the control surface from the surroundings to the control volume	$[W/m^2]$
Re	Reynolds number	[-]
r_p	Pressure ratio p_2/p_1	[-]
SN	Smoke Number	[-]
T	Temperature	$[K]$
T_{ad}	Adiabatic flame temperature	$[K]$
TSFC	Thrust specific fuel consumption	$[g/kN]$
U	Characteristic mean flow velocity	$[m/s]$
v	Velocity	$[m/s]$
V	Volume	$[m^3]$
W_{cv}	Work done by the control volume	$[J]$
We	Weber number	[-]

k	Kinetic energy per unit mass	$[m^2/s^2]$

Greek Letters

α	Azimuthal Start Angle	[deg]
β	Azimuthal Stop Angle	[deg]
γ	Mass fraction	$[kg/kg]$
δ_f	Final layer thickness	[-]
δ_s	Layer stretching	[-]
ε	Eddy viscosity	$[m^2/s]$
η_{joule}	Efficiency of the air-standard Brayton-Joule cycle	[-]
$\eta_{combustion}$	Efficiency of combustion	[-]
θ	Cone Angle	[deg]
μ	Absolute viscosity	$[Pa.s]$
μ_T	Turbulent viscosity	$[m^2/s]$
π_{00}	Engine pressure ratio at take-off	[-]
ρ	Density	$[kg/m^3]$
σ	Stress tensor	$[Pa]$
τ	Sheer stress	$[Pa]$
ϕ	Equivalence ratio	[-]
	Scalar such as pressure, energy or species concentration	[-]
Δt	Time step size	$[s]$
Δx	Smallest edge length	$[m]$

Subscripts

0	Engine inlet stage
1	Compressor inlet stage
2	Combustion chamber inlet stage
3	HPT inlet stage
4	LPT outlet stage
5	Engine exit stage
a	Air
c	Combustion chamber
f	fuel
i	Element/Molecule
	Inlet
ref	Reference state
	Reference data
o	Outlet
i,j	Coordinate directions

Chapter 1

Introduction

1.1 Motivation

During the past decade, the consumption of fuel by civil aviation has increased to the extent that air transport is now perceived as one of the world's fastest growing energy-use sectors [1]. Worldwide demand of jet fuel has been steadily increasing since 1980. Consumption more than tripled in 30 years from 1,837,000 barrels/day in 1980, to 5,220,000 in 2010 [2].

Emissions resulting from the combustion of fossil fuels are usually considered as the main responsible for Greenhouse Gas (GHG[1]) emissions, which are appointed as the primary factor that leads to global warming [3]. There are two main sources of aircraft emissions, the jet engines and the auxiliary power unit (APU). Most jet fuel is burned in flight so most of the emissions occur at altitude, not at ground level. Air traffic is the major contributor to high altitudes emissions, which induce strong impact on atmospheric chemistry [4].

Therefore, it has a significant impact both on local air quality and global atmospheric changes, which leads to the introduction of more drastic regulations of pollutant emissions [5]. The Committee on Aviation Environmental Protection (CAEP) and the Advisory Council for Aviation Research and Innovation in Europe (ACARE) have set up ambitious targets for 2020 [6]. There are multiple objectives [5]:

1. ACARE has a target of 20% reduction of carbon dioxide emissions and fuel consumption for the engine alone (and 50% for the overall aircraft) compared to the reference of 2000, which requires the development of engines with very high efficiency [5].
2. New environmental standards require mitigation of pollutant emissions (smoke, *CO*, UHC) with great effort towards NO_x. The CAEP has a midterm goal of 45% and a long-term goal of 60% NO_x reduction compared to the standard of 2008 [4]. Today, most engines on the market are 20 % below CAEP 6 regulations. However, for engines with high overall pressure ratio (OPR) (such as GE90 engine, with OPR $\simeq$ 45), this margin is reduced [5]. The ACARE has an overall target of 80% NO_x reduction compared to the reference of 2000, with 60% for the combustor only [5].

There are technology and practical solutions to reduce the amount of heat-trapping emissions resulting from the continued increase in traffic in the aviation industry. For example, changes

[1] The GHG is a gas atmosphere that absorbs and emits radiation within the thermal infra-red range. This process is the fundamental cause of global warming.

in the structure of aircraft have been held to decrease fuel consumption thus reducing the emissions of GHG. An example of this is the blended winglets, the new design feature in the wing tips. In the blended winglets the drag is reduced which consequently increases fuel efficiency. Other solution that have also taken part in the quest to reduce GHG emissions is the modification in the engines. The most significant change in the engine configuration was an increase in its bypass ratio[2]. This increased greatly the fuel efficiency in civil aviation when compared to its predecessor low-bypass engine, which is more compact but less fuel efficient and much noisier [7].

The exhaust from an aircraft gas turbine is composed of *CO* (carbon monoxide), carbon dioxide (CO_2), water vapor (H_2O), unburned hydrocarbons (UHC), particulate matter (mainly carbon), NO_x (nitrogen oxides) and excess atmospheric oxygen and nitrogen. Carbon dioxide and water have not always been regarded as pollutants because they are the natural consequence of complete combustion of a hydrocarbon fuel [1]. However, they both contribute to global warming and can only be reduced by burning less fuel [1].

Aircraft engines have two quite different requirements [8]. The first is for very high combustion efficiency at low power, because of the large amounts of fuel burned during taxiing and ground manoeuvring. The primary problem here is the reduction of UHC [8]. At take-off power, climb and cruise the main concern is NO_x [8]. The International Civil Aviation Organization[3] (ICAO) sets standards on a worldwide basis, for both the take-off and landing cycles and also for cruise at high altitude; the first is concerned with air quality in the vicinity of airports and the second with ozone depletion in the upper atmosphere [8].

1.2 Objectives

1.2.1 General Objectives

Within the context mentioned in the previous section, the work presented in this thesis has as main objective to simulate the combustion and emission of pollutants from the major civil jet fuels grades (Jet A, Jet B and TS-1) in a CFM56-3 combustor, while burning them throughout ICAO's LTO (landing and take-off) [4] cycle.

[2] The bypass ratio defines the amount of air that bypasses the core of the engine, from the air that goes through the core.
[3] The International Civil Aviation Organization is a specialized agency for the safe and orderly development of civil aviation worldwide, by establishing standards and regulations necessary for the proper functioning of the aviation industry, safely and efficiently.
[4] LTO cycle is defined by ICAO. It covers four modes of engine operation, namely idle, approach, climb out and take-off, each of which is associated with a specific engine thrust setting and a time in mode [95]. It is explained in detail in the section 2.6.1.

1.2.2 Specific Objectives

To achieve the objective described previously is necessary:

1. Understand the process of combustion and formation of pollutants in annular chambers.
2. Select usual jet fuels and engine operating points (take-off, cruise, approach and idle).
3. Simulate the various jet fuels at the points considered.
4. Perform a comparative study of the various jet fuels.
5. Analyse the flow and justify possible malfunctions.

1.3 Thesis Structure

This thesis is divided into five chapters.

In the first chapter, the current chapter, the author expresses his motivation behind the development of this thesis. In this chapter, the problems are presented, as well as respective solutions. The objectives proposed for this thesis are also presented, divided into general objectives and specific objectives. This chapter also contains the structure of the thesis and some studies of other authors are presented.

Chapter two presents the fundamentals and systems behind Gas Turbine Emissions (GTE) because the combustor's performance is hugely dependent on these. And in this chapter, will be presented a close-up on the main requirements, types of chambers, fundaments of combustion and the mechanisms of pollutants formation.

The third chapter presents the CFD simulation process and is composed of several processes. Before starting the process of numerical simulation is necessary a whole set of steps: geometry, generation of the mesh and the numerical simulation. In this chapter are also selected the fuels to be used.

In the fourth chapter are presented the results and discussion, as well as explained what is expected and what is new. Deviations are also justified.

The fifth chapter is the last chapter and presents the main conclusions of this thesis research and some thoughts for future work, respectively.

1.4 Historical Review

Sir Isaac Newton was the first to theorize, in the 18th century, that a rearward- channelled explosion would propel an aircraft forward at a great rate of speed, in other words, as the hot air blast backwards through the nozzle, the plane moves forward [9]. This theory was based on his third law of motion [9]. Since then, several attempts have been made in order to build an

engine that would work on this principle [9]. The first attempt was made by Henry Giffard in 1852 who developed a three-horsepower steam engine to propel his airship. Although this flight was counted as a success, the airship lacked the power to navigate properly [10].

Bearing in mind the pressures and exigencies of wartime Britain and Germany, and the lack of knowledge and experience available to the designer, it is perhaps hardly surprising that the first generation of gas turbine combustors were characterized by wide variations in size, geometry, and the mode of fuel injection [1]. With the passage of time and the post-war lifting of information exchange, some commonalities in design philosophy began to emerge [1]. By around 1950, most of the basic features of conventional gas turbine combustors, as we know them today, were firmly established [1]. Since that time, combustor technology has developed gradually and continuously, rather than through dramatic change, which is why most of the aero-engine combustors now in service tend to resemble each other in size, shape, and general appearance [1].

Gas turbine combustion during the last half century

During the past half century, combustion pressures have risen from 5 to 50 atmospheres, inlet air temperatures from 450 to 900 K, and outlet temperatures from 1100 to 1850 K [1]. Despite the continually increasing severity of operating conditions, which are greatly exacerbated by the concomitant increases in compressor outlet velocity, today's combustors exhibit close to 100% combustion efficiency over their normal operating range, including idling, and demonstrate substantial reductions in pollutant emissions [1].

For both British and German engineers, the development of a workable combustor was an obstacle that had to be overcome in their independent and concurrent efforts to achieve a practical turbojet engine [1]. The following abridged account of the early history of gas turbine combustion in Britain, Germany, and the United States is intended to cover the period from the start of World War II until around 1950, by which time it was generally accepted that the piston engine had reached its limit as a propulsion system for high-speed flight and the gas turbine was firmly established as the powerplant of choice for aircraft applications [1].

Britain

The method adopted by Whittle, for his first turbojet engine, was to heat the liquid fuel for combustion to above the boiling point of its heaviest hydrocarbon ingredient, so that it is entirely converted into vapor before combustion [1]. This engine employed 10 separate tubulars combustors in a reverse-flow arrangement to permit a short engine shaft. Whittle tried several vaporizer tube configurations, more than 30 in all [1], as show in figure 1.1.

The fuel was maintained at high pressure so that vaporization could not occur until it had been injected through a nozzle and its pressure reduced to that of the combustion zone [1]. Whittle experienced considerable difficulties with this system, due mainly to problems of thermal cracking and coking up of the vaporizer tubes, as well as difficulties in controlling the fuel flow rate [1].

After many trials and setbacks, Whittle adopted a combustor whose main attraction was the replacement of vaporizer tubes by a pressure-swirl atomizer having a wide spray cone angle [1].

Another early British engine was the De Havilland Goblin, which was the first engine to power the Lockheed P-40 [1]. The Goblin is of historical interest because it was the first British engine to use "straight-through" combustors, as opposed to the "reverse-flow" type employed on all previous engines [1]. The first British annular combustor appeared on the Metropolitan Vickers Beryl engine [1]. The invention of this annular combustor came with the use of upstream fuel injectors, and the introduction of downstream dilution air; the upstream fuel injectors were claimed to have the fuel droplets at a higher residence time in the combustion zone, providing more time for fuel evaporation [1]. The downstream dilution air served two purposes; firstly, air is introduced through a first row of scoops, supplying the needs of air to complete the combustion process, with the remaining of this air serving for dilution purposes; the second row of scopes was for dilution purposes [9].

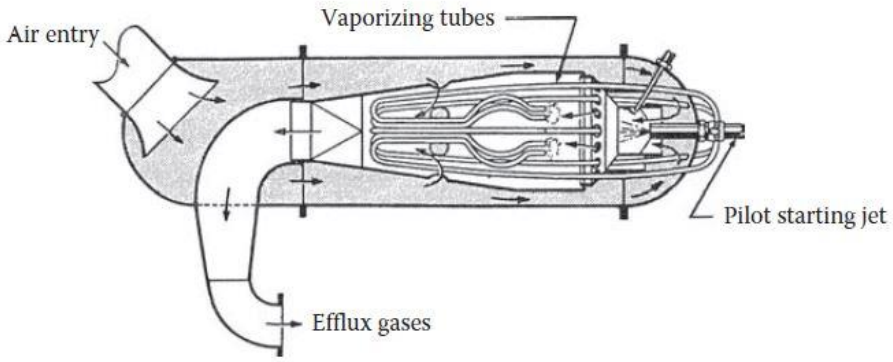

Figure 1.1 Early Whittle vaporizer combustor [1].

Germany

The Jumo 004, as show in figure 1.2, and its contemporary BMW 003 were the only axial-flow turbojet engines to go into production during World War II. The Jumo 004 was developed by Anselm Franz, and it was among the first engines to employ axial flow turbomachinery and straight through combustors [1].

Franz was the first to recognize the superiority of an annular combustor design, but he opted for the can configuration because it would present less of a problem and allow bench testing

with a single can [11]. The primary air flowed into the liner through six swirl vanes, the amount of air being sufficient to achieve near-stoichiometric combustion at the engine design point [1]. Mixing between combustion products and dilution air was achieved using an assembly of stub pipes that were welded to a ring at their upstream end and to the outer perimeter of a 10 cm diameter dished baffle at their downstream end [1]. The hot combustion products flowed radially outward through the gaps between the stub pipes to meet and mix with part of the cold secondary air [1]. The remaining secondary air flowed through the stub pipes, incidentally serving to protect them from burnout because of their immersion in the hot combustion gases, to provide further mixing of hot and cold gases in the recirculation zone created by the presence of the baffle [1].

The BMW 003 employed an annular combustor fitted with 16 equispaced, downstream-spraying, pressure atomizers [1]. Each fuel nozzle was surrounded by a baffle and the primary combustion air flowed both through and around it [1]. Dilution air flowed through 40 scoops attached to the outer liner, alternating in circumferential locations with 40 similar scoops attached to the inner liner [1]. The result was a combustor having a relatively low-pressure loss, but also a high length/ratio, which led to a long engine [1].

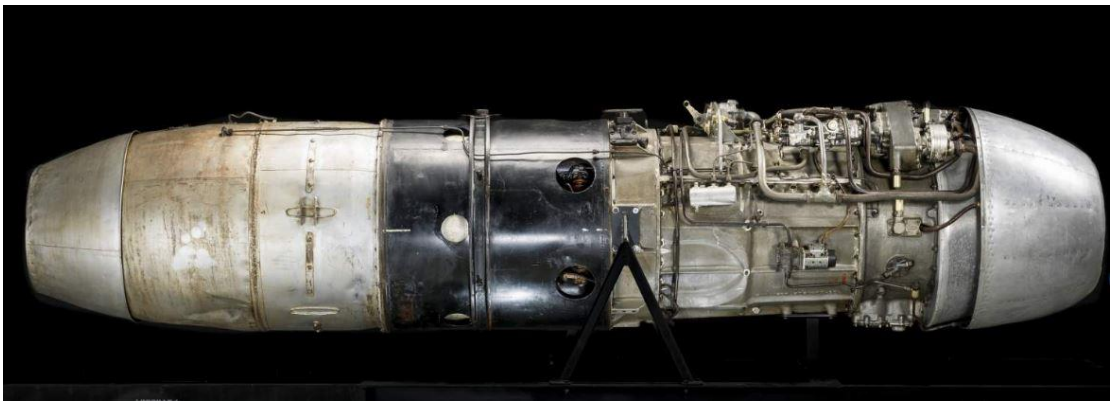

Figure 1.2 Jumo 004B Engine [12].

The United States

In 1947, Pratt and Whitney (P&W), having been fully preoccupied with piston engine production throughout the war, made its first entry into the turbojet arena by licensing the Nene engine from Rolls Royce [1]. For example, GE's Whittle-derived J31 engine employed a reverse-flow combustor, but a straight-through version, as shown in figure 1.3, was adopted for the J33 and for subsequent engines such as the J35 and J47 [1]. For its J57 engine, employed eight tubular liners located within an annular casing [1].

By the end of the 1940s, the development work carried out in the UK, Germany, and the United States had established the basic design features of aero-engine combustors that have remained largely unchanged [1].

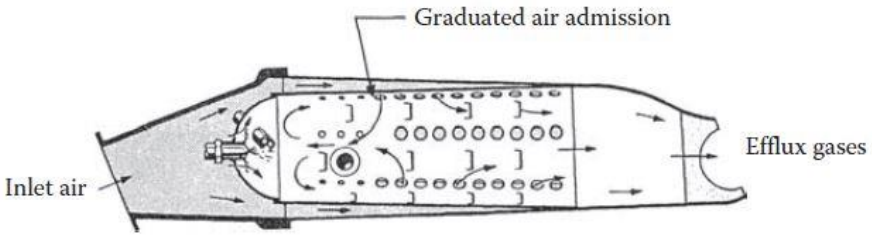

Figure 1.3 General Electric J33 tubular combustor [1] .

GE Low Emissions Combustor Evolution

Most current fielded products use the GE rich-burn LEC concept [13]. This is an adaption of the RQL (rich quench lean) concept where there is a rich combustor primary zone to provide low CO and HC emissions and good ignition capability [13]. NO_x formation rates are low in the primary zone because the flame temperature of the rich primary mixture is relatively low, and there is little free oxygen available to form NO_x [13]. Flow exiting the primary zone is rapidly diluted, or "quenched", to a uniform lean mixture. With this concept, fast and uniform mixing during the quenching process is critical in order to minimize the time available for NO_x formation as the mixture goes through stoichiometric fuel air ratio, where maximum flame temperatures lead to maximum NO_x formation rates [13]. Over the past 35 years, the LEC combustor has been developed to reduce NO_x by 25-50% relative to first generation combustors [13].

Figure 1. 4 shows the evolution of low emissions combustors at GE.

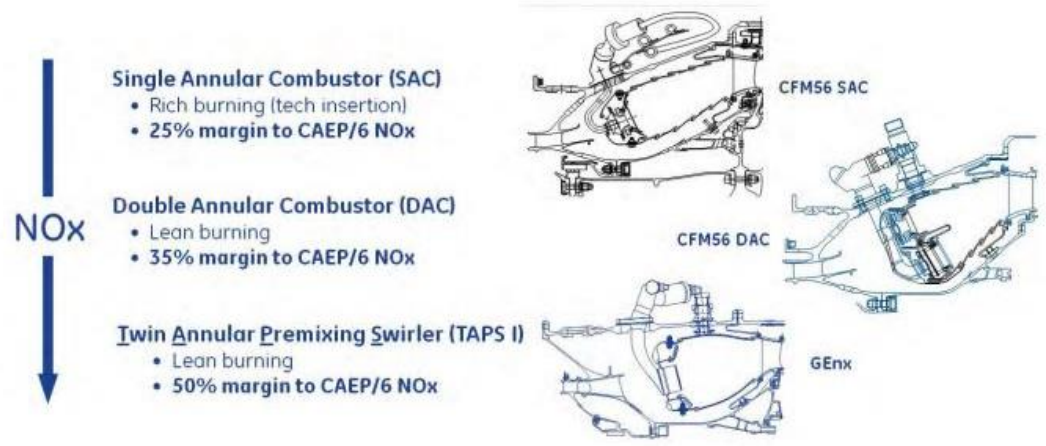

Figure 1.4 GE Low Emissions Combustor Evolution [13].

Programs to develop new low emission combustor concepts for aircraft engines have been underway since the mid-1970s [13]. One of the first large aircraft engine emissions reduction programs was the NASA Experimental Clean combustor program, which sponsored early development of the Dual Annular Combustor (DAC) at GE [13]. After many years of intermittent development, the DAC entered service in the CFM56-5B and CFM56–7B engines in the mid-1990s. The DAC was designed with two stages: a pilot stage in the outer annulus of the burner, and a main stage in the inner annulus [13]. Only the outer (pilot) stage was fuelled during light-off and at low power. The pilot was designed with low airflow and low through-flow velocity to achieve good ignition and low *CO* and HC emissions [13]. The main stage was designed with high airflow and high velocity to provide a lean flame with minimal time for NO_x formation [13]. Although the DAC flame was lean, the fuel and air were inserted through a conventional fuel nozzle and swirl cup, so it was not a premixed flame. An issue with the DAC was the combustor exits temperature profile could be non-uniform during the different staging conditions [13].

Twin Annular Premixing Swirler (TAPS) Combustor

Another effort in reducing emissions resultant from the combustion process, was the invention of Twin Annular Premixing Swirler (TAPS) combustor. The TAPS combustor evolved based on lessons learned with fuel staging of the DAC, and also benefitted from extensive experience with Dry Low Emissions lean-premixing combustors in aero-derivative industrial gas turbines [13]. The TAPS combustor concept is a lean burn system where each fuel injector contains a centre pilot and concentric outer main [13], as shown in figure 1.5.

The central pilot tip is a rich burn configuration similar to traditional combustors [13]. At starting and low power operation fuel is 100% in the pilot [13]. At higher power fuel is split between the pilot and main. The main injection is a set of radial jets that enter a larger main air swirler [13]. The main is a large effective area swirler to burn fuel lean [13]. At high power most of the fuel is injected through the main [13]. This makes both the pilot and main mixers fuel lean with approximately 70% of combustor total air flow through those 2 mixers [13]. TAPS combustor development started in 1995 as a GE/NASA emissions reduction technology program.

The TAPS system is used in the GEnx engine[5] which entered service in 2010. Figure 1.6 shows the TAPS development program [13].

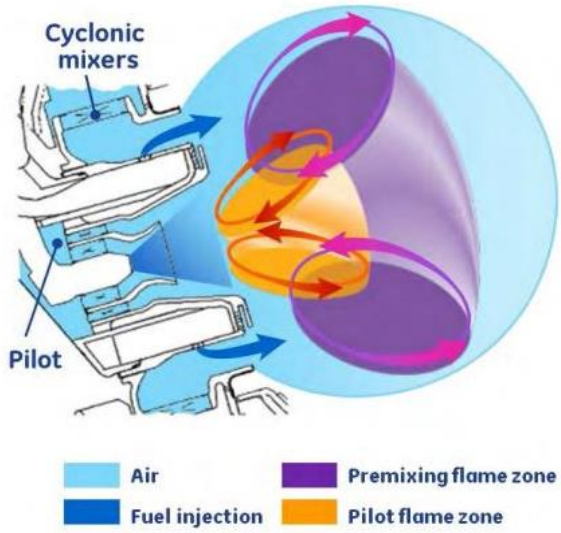

Figure 1.5 TAPS Fuel Injection Concept [13].

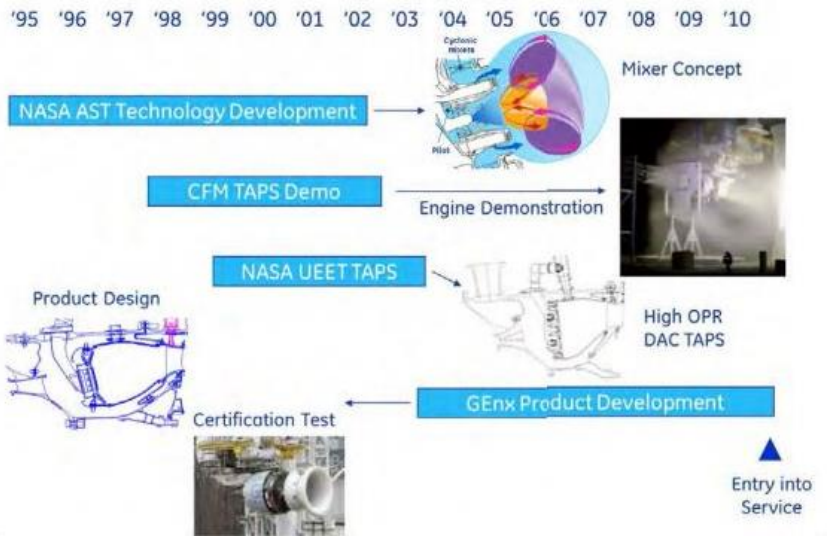

Figure 1.6 TAPS Development History [13].

Aviation Fuel

Aviation fuel is the fuel used to power aircraft in flight. Currently the great majority (more than 99%) of aviation fuel used in both civil and military aircraft is jet fuel [14]. A small quantity of aviation gasoline is still used in small aircraft [14]. In recognition of aviation's more stringent requirements compared to ground transportation, separate specifications for aviation gasoline were developed after World War I [14]. Subsequent aircraft spark ignition engine developments

[5] The GEnx is the fastest-selling, high-thrust jet engine in GE Aviation history with more than 1,600 engines on order. In addition to powering the four-engine Boeing 747-8, the GEnx engine is also the best-selling engine for the Boeing 787 Dreamliner [96].

as World War II approached identified the need for high octane in aviation fuel for improved performance [14].

Beginning in the 1930, research was initiated in both Great Britain and Germany on the development of a gas turbine aircraft engine, which was radically different from the spark-ignition [14]. During this development, illuminating kerosene used as a fuel for lamps, was chosen as the liquid fuel for the jet engine because it did not conflict with the very strong military demand for high-octane aviation gasoline [14]. This use for jet engines of distillate-based fuels different in composition from high-octane gasoline has continued to this day [14].The first operational use of jet-engine-powered aircraft occurred in a military aircraft late in World War II [14]. The development and rapid growth of higher-speed commercial transport aircraft using jet engines began in the late 1950s [14]. As a result of the switch of both military and commercial aircraft to jet engines from spark ignition engines, jet fuel demand rose rapidly, and jet fuel over time displaced aviation gasoline as the dominant fuel for aviation use [14].

Major Civil Jet Fuel grades

The kerosene type fuels most used worldwide in civil aviation are of Jet A and Jet A-1 grades: Jet A (kerosene), used in the USA, and Jet A-1 used in the majority of the rest of the world [15]. Jet A has a flash point minimum of 38^oC and a freeze point maximum of -40^oC [16]. Jet A-1 has same flash point as Jet A but a lower freeze point (maximum of -47^oC) [16]. Table A .1, in Appendix A, shows some of the required specification properties of Jet A and Jet A-1.

Other fuels can be used as an alternative to Jet A-1 [16]. Jet B is called wide cut fuel because it is a blend of gasoline & kerosene fractions [17] and is used in very cold climates, e.g. in northern Canada where its thermodynamic characteristics are suitable for handling and cold starting [16].

TS-1 is the main jet fuel grade available in Russia and the Commonwealth of Independent States. It is a kerosene type fuel with slightly higher volatility and lower freeze point compared with Jet A-1 [18].

The main fuel used in China is RP-3 (renamed No 3 Jet Fuel) and is basically as Western Jet A-1, produced as an export grade [19].

1.5 Bibliographic Review

Experimental Studies/Methods

Since aircraft emissions are related to engine thrust (e.g. Anderson et al. [20] , Kinsey et al. [21] [22], Timko et al. [23], Whitefield et al. [24] and Lobo et al. [25]) and engines are designed

for high performance while cruising at high altitudes, some aircraft operations within airports require that engines operate outside of their optimal regimes, ranging from maximum thrust during take-off to low power settings during operations on the ground [16]. This fact was clearly highlighted during the APEX-1 campaign by Onasch et al. [26], who reported that a CFM56 engine is less efficient at the low thrust levels usually used at airports. This may result in potentially higher emissions on the ground than that during cruising for those pollutants mainly emitted at low power, such as *CO* and hydrocarbons [16].

An interesting study was held by Spicer et al. [27], about comprehensive measurements of the organic and inorganic gaseous emissions, and the particle emissions from two turbine engines. Emissions measurements were made at five engine power settings, including Idle, stage 1 augmentation (afterburner), Intermediate (approximately 100 percent of rated thrust), and three other thrust settings. This study has characterized the organic chemical emissions from an F110 and an F101 turbine engine. The engines were operated in an indoor test cell using JP-4 fuel. Engine operating parameters and environmental conditions were monitored during all emission tests. This study has shown that the organic emissions from these two engines are very low compared with several other turbine engines. Methane is the dominant organic chemical in the exhaust at all power levels reported [27]. Much of the methane in the exhaust may be due to atmospheric methane that was present in the ambient air used for combustion [27]. Other than methane, four compounds (ethane, formaldehyde, acetylene, and propene) account for 20- 40 percent of the volatile organic emissions from these engines at Idle [27]. These four chemicals are products of combustion [27]. Aldehydes, which also are products of the combustion process, were measured at significant concentrations in the exhaust [27]. Several dicarbonyl compounds were observed in the exhaust. These chemicals are significant because they are photochemically reactive; they have not been reported by others who have studied turbine engine exhaust [27]. The distribution of emissions by compound class has been reported for four power settings. Alkanes were the most significant class of organic chemicals by concentration at all power levels. Alkenes, aldehydes, and ketones were generally products of incomplete combustion and were present at much higher concentrations at low power [27].

Subsequent study made by Spicer et al. [28] added further information and provided detailed information on the organic component of turbine engine emissions. Following from these pioneering studies, the scientific literature now comprises many studies and most have concluded that aircraft exhausts are responsible for significant emissions of a series of gaseous, semi-volatile and non-volatile species [16].

The use of standard LTO cycles as a surrogate for typical aircraft operations close to the ground represents an approximation and is not always representative of operations at airports [16]. Patteron et al. [29] and Khadilkar and Balakrishnan [30] observed that total fuel burn during departures and arrivals at airports is generally overestimated by ICAO method with respect to emissions computed from real-time aircraft flight data. Other studies have also reported

measured TIM [6] at airports: Unique [31] reported TIM in Zurich airport and detected differences in all the LTO phases: idle (-43%), approach (+10%), climb(-77%) and take-off(+129%) which have been estimated to have a strong impact on the calculation of emissions, resulting in reduced fuel flow (-38%) and NO_x emissions (-31%) [16].

Recent studies assessing airport emissions have proposed and used LTO cycles which are much more complex than those standardised by the ICAO [16]. For example, in a study of the air quality and public health impacts of UK airports, Stettler et al. [32] used specific TIMs composed of 12 phases, namely approach, landing roll, reverse thrust, taxi-in, taxiway acceleration, APU, taxi-out, taxiway acceleration, hold, take-off, initial climb and climb-out [16].

Currently, the scientific literature includes several studies aiming to give EIs[7], for comparison with reported ICAO databank certification data and for many other components, including particulate matter, elements, ions and speciated hydrocarbons [16]. However, such data are often sparse and results poorly comparable [16]. Carls et al. [33] noticed that EIs do not give indication of the absolute contribution of aircraft emissions to ground-level concentration, which is important for assessing air quality at airports. Furthermore, they commented that the value of EIs may be substantially affected by limited knowledge of some important aircraft operational factors [16]. Table B.1, in Appendix B, provides a list of recent studies which measured EIs during real aircraft operations at airports. This table also reports supplementary information about the target of the study, period and location of experiments, tested aircraft or engine models, measured pollutants, analysed LTO phases and sampling methodologies [16].

Some studies have derived EI (CO) directly from measurements during normal operation of idle and taxi at airports and have revealed some considerable differences compared to ICAO data, with results generally higher than those certified [16]. Heland and Schäfer [34] reported an EI(CO) of 51.8 ± 4.6 $g\ /kg_{fuel}$ at idle for a CFM56-3 engine, which was about 27-48% higher than the ICAO data. Herndon et al. [35] reported that EI (CO) observed in ground idle plumes was 943 greater (up to 100%) than predicted by engine certification data for the 7% thrust condition. Since CO emissions increase with decreasing thrust, these studies seem to confirm that normal idle and taxi operations at airports occur at lower thrust than the standardised ICAO LTO cycle, resulting in more CO emitted than certified values [16].

The relative amount of exhaust emissions depends upon combustor temperature and pressure, fuel to air ratio and the extent to which fuel is atomised and mixed with inlet air [20]. It is well recognised that the amounts of many pollutants may vary considerably with the engine

[6] Time-in-mode (TIM) is the time period, usually measured in minutes, that the aircraft engines actually spend at an identified power setting; typically pertaining to one of the LTO operating modes of the operational flight cycle [99].
[7] The emissions during standardised LTO cycles are then reported as emission indices (EIs) expressed as mass of pollutant emitted per unit mass of fuel burned [16].

technology, model and especially with the thrust [16]. For example, Spicer et al. [28] reported that hydrocarbon emissions can be dependent upon engine type, use and maintenance history as well as fuel composition [16].

Computational Studies/Analyses

Stari et al. [36] developed a study that was focused on the numerical analysis of pollutant formation in an aviation gas turbine engine at different values of power setting. The analysis was conducted on the basis of a comprehensive approach treating the reactor net model for description of nonequilibrium chemical processes inside the combustor and the quasi-one-dimensional model to compute the evolution of species concentrations in the post combustor flow. Special attention was paid to the study of the formation of volatile aerosol precursors: sulfuric and nitrous acids and organic compounds. The applied approach provided a reasonable agreement between predictions and measurements of emission indices for main pollutants NO_x, CO, C_xH_y, SO_2 and HNO. It was shown that, whereas the concentrations of the main components of combustion exhaust, NO_x, CO, CO_2 and H_2O vary only slightly in the turbine and nozzle flow, the concentrations of sulfur compounds and other condensable species can change noticeably. The simulation also demonstrated that the concentration of organic condensable matter in the engine exhaust can be comparable to (or even greater than) the concentration of sulfuric acid at 85 and 30% power setting, even at a moderate value of sulphur fuel content (400 mg/kg) [36].

A study was performed by Mueller and Piitsh [37] about an integrated kinetics-based Large Eddy Simulation (LES) approach for soot evolution in turbulent reacting flows was applied to the simulation of a Pratt & Whitney aircraft gas turbine combustor. The integrated approach included detailed models for soot, combustion, and the unresolved interactions between soot, chemistry, and turbulence. The soot model was based on the Hybrid Method of Moments and detailed descriptions of soot aggregates and the various physical and chemical processes governing their evolution. The detailed kinetics of jet fuel oxidation and soot precursor formation were described with the Radiation Flamelet/Progress Variable model, which has been modified to account for the removal of soot precursors from the gas-phase [37]. Two fuel-to-air ratios (FAR) were simulated in order to access the ability of the model to perform predictions at the chosen operating points and to perform predictions when a parameter is varied. The detailed soot model used in this study was obtained from Mueller et al. [38]. For the combustor simulation, the integrated approach was combined with a Lagrangian parcel method for the liquid spray and state-of-the-art unstructured LES technology for complex geometries. Two overall fuel-to-air ratios were simulated to evaluate the ability of the model to make not only absolute predictions but also quantitative predictions of trends. The Pratt & Whitney combustor is a Rich-Quench-Lean combustor in which combustion first occurs in a fuel-rich primary zone characterized by a large recirculation zone. Dilution air was then added downstream of the recirculation zone, and combustion continues in a fuel-lean secondary zone [37].

Quantitatively, the soot emissions from the combustor were overpredicted by about 50%, which was a substantial improvement over previous works utilizing RANS (Reynolds Averaged Navier-Stokes) to predict such emissions, and the FAR predicted by LES compared very favourably with experimental measurements.

Chapter 2

Combustor Basic Considerations

2.1 The CFM56-3 Engine

The CFM56-3 engine was developed in the 70's and was certified in 1984 to be incorporated in Boeing 737 [39]. The CFM56-3 exists in four different versions [40] as summarized in table 2.1.

Table 2.1 Versions of the CFM56-3 [39].

Version	Thrust	Application
CFM56-3-B1	20000lb	Boeing 737-300 Boeing 737-500
CFM56-3-B2	22000lb	Boeing 737-300 Boeing 737-500
CFM56-3-C1	23500lb	Boeing 737-400
CFM56-3-B1 Derated	18500lb	Boeing 737-500

About 4,500 CFM56-3s operate globally with 195 different airlines [39]. The CFM56-3 fleet has accumulated more than 150 million Engine Flight Hours (EFH) and 108 million Engine Flight Cycles (EFC) and has an average EFC time of 1.4EFH (average of 1 hour and 24 minutes per flight) [41]. A resume of the specifications of the CFM56-3 are presented in table C.1 (see Appendix C).

2.1.1 General Constitution

The CFM56-3 is a dual - shaft[8] engine with an engine with a thrust rating between 18,500 lbs and 23,500 lbs and compression ratio of 27.5-30:1. This particular variant has a bypass ratio of 6:1 with a 60 inches fan diameter, and a dry weight of a 4,300 lbs [42].
The CFM56-3 is constituted by three main parts [42]:

1. Low pressure system.
2. High pressure system.
3. Accessory drive section.

[8]Dual-shaft design consists of a fan and booster (low pressure compressor), high pressure compressor, annular combustion chamber and a high and low -pressure turbine section [42].

The constitution of each part is summarized in the table 2.2. Figure 2.1 shows the schematic overview of the CFM56 of the engine components.

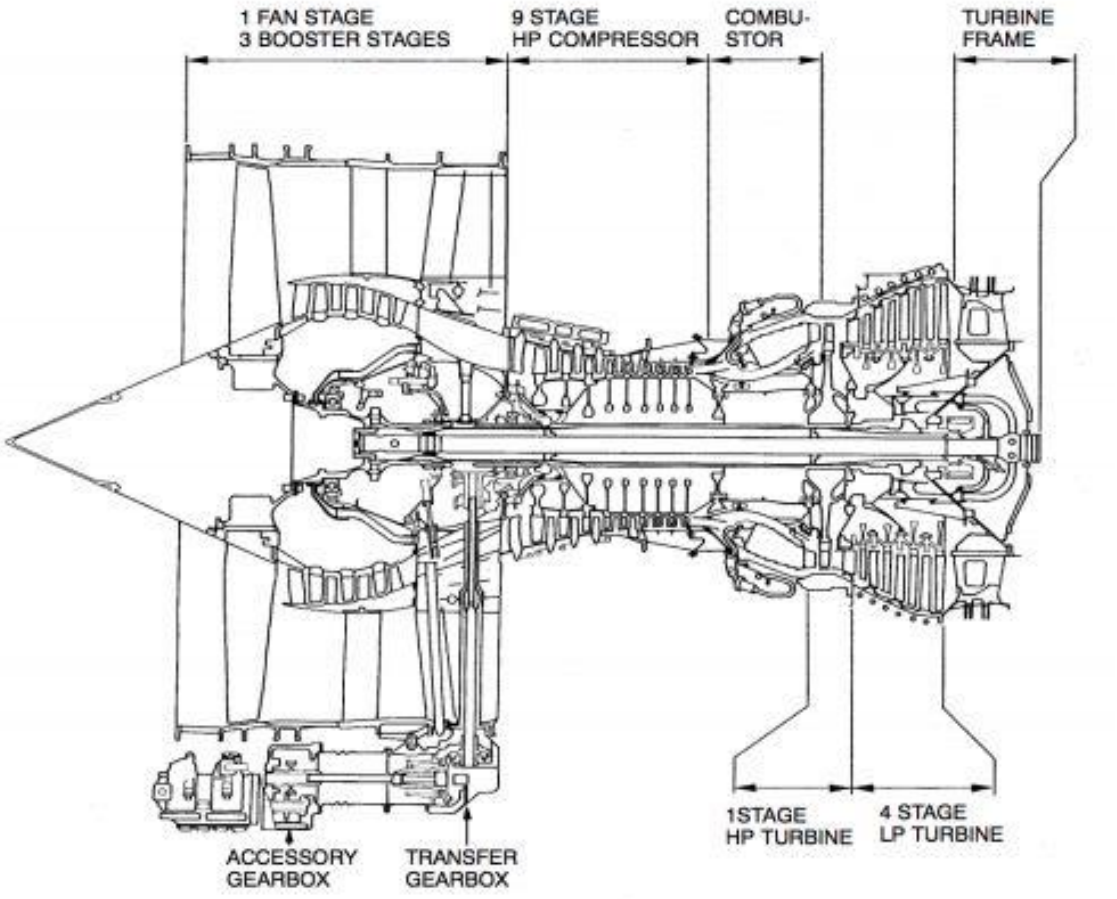

Figure 2.1 CFM56 schematic overview of engine components [42].

Table 2.2 Summary of the components of the 3 main parts of the CFM56-3.

Main Parts	Components
Low- pressure system	Single-stage Fan, to which the Booster rotor is coupled. Three-stage Booster, with 4 stator stages. Outlet Guide Vanes (OGV), used for guiding the Fan discharge air. 12 Variable Bleed Valves (VBV), used to control the flow of air to the engine core. Low Pressure Turbine (LPT), with 4 rotors and 3 stators.
High- pressure system	Nine-stage HPC rotor. Single-stage Inlet Guide Vanes (IGV), to guide the incoming air to the HPC. Three stages of Variable Stator Vanes together they make the variable stator system of the HPC. Five stages of fixed geometry stators in the HPC's following stages. Outlet Guide Vanes (OGV)[9] used to make the air enter the combustion chamber axially. Annular combustion chamber, with 20 fuel injectors; High Pressure Turbine (HPT) nozzles, for guiding the incoming air flow. HPT rotor coupled with the HPC rotor. Nozzles of the LPT's first stage.
Accessory drive section[10]	Inlet Gear Box (IGB). Transfer Gear Box (TGB). Horizontal Drive Shaft (HDS). Accessory Gear Box (AGB).

2.2 Jet engine principles and mechanics

The aircraft gas turbine engine is a complex machine using advanced technology based on many engineering disciplines such as aerodynamics, materials science, combustion, mechanical design, and manufacturing engineering.

The air is sucked by the engine inlet. Some of the incoming air passes through the fan and continues into the core compressor and then the burner, where it is mixed with fuel and

[9] The outlet Guide Vanes is often referred as the stator of the 9^{th} stage of the HPC.

[10] The accessory drive section is used in two different moments. First, at engine start, it is used to move the high-pressure compressor. Once the engine starts, it is used to extract energy from the high-pressure compressor for the multiple accessories in the engine and airplane.

combustion occurs [43]. The hot exhaust passes through the core and fan turbines and then out the nozzle, as in a basic turbojet [43]. The rest of the incoming air passes through the fan and bypasses, or goes around the engine, just like the air through a propeller. The air that goes through the fan has a velocity that is slightly increased from free stream. So, a turbofan gets some of its thrust from the core and some of its thrust from the fan [43]. The ratio of the air that goes around the engine to the air that goes through the core is called the bypass ratio. Because the fuel flow rate for the core is changed only a small amount by the addition of the fan, a turbofan generates more thrust for nearly the same amount of fuel used by the core [43]. This means that a turbofan is very fuel efficient. In fact, high bypass ratio turbofans are nearly as fuel efficient as turboprops [43].

This chapter will describe a deeper insight in each of these systems, and a very detailed view of the combustor.

2.2.1 The working Cycle

Figure 2.2 shows the ideal Brayton cycle on which all modern gas turbines are based. The explanation of the cycle is as follows:

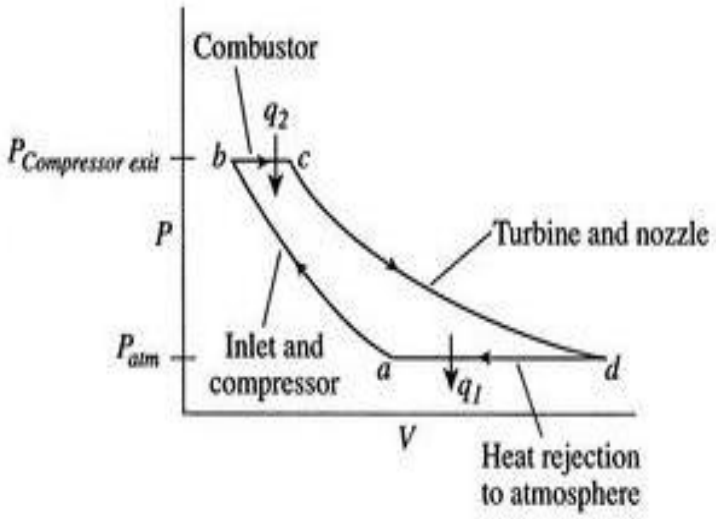

Figure 2.2 Pressure-Volume diagram of the Brayton Cycle [100].

Process A to B: is an isentropic compression process, where the compressor increases the pressure and the air temperature from the input values.

Process B to C: heat is added to the air by introducing and burning fuel at constant pressure, thereby considerably increasing the volume of air [44].

Process C to D: isentropic expansion, occurs in the turbine, where the gases from the combustion chamber are expanded and the energy extracted in the expansion of the gases is

transformed into mechanical energy, the remaining energy being expanded in the propulsive nozzle.

Process D a A: heat rejection at constant pressure.

2.2.2 The compressors

The compressor is the first component of a gas turbine, in its constitution are two or more shafts where several sets of blades are fixed. Each of these blade assemblies (rotor and shaft) has the function of compressing the air coming from the diffuser and, consequently, also increasing the temperature.

Mechanical energy from the turbine section is transferred by a shaft to the rotor where it adds kinetic energy to the airflow. The increase of kinetic energy is then transferred into potential energy (static pressure) by the stators. The stator blades are designed as small diffusers and they convert the kinetic energy into potential energy by decelerating the air [42].

The compressor section consists of the following components [42]:

1. a single stage fan.
2. a three-stage low-pressure compressor.
3. a nine-stage high-pressure compressor.

The fan and three stage low-pressure compressor are driven by the low-pressure turbine and the high-pressure compressor is driven by the high-pressure turbine [42]. A diagram of the CFM56-5A compressor section is shown in figure 2.3.

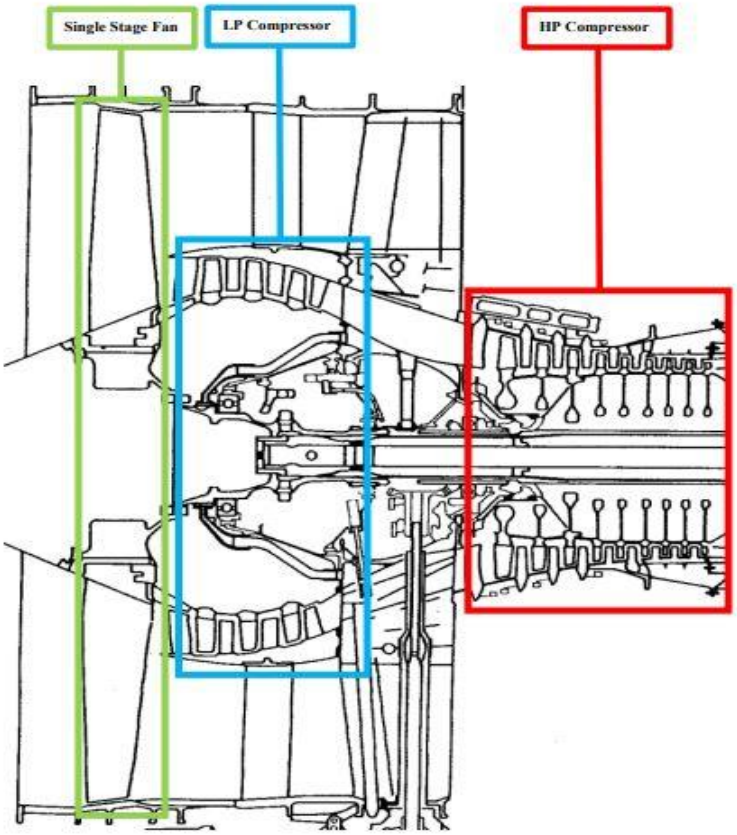

Figure 2.3 Outline of compressor sections in the CFM56-5A [42].

The axial low-pressure compressor (LPC) is also defined as the "Booster Assembly" for the CFM56.

The LPC section consists of the following components [42]:

1. Spinner front and rear cone.
2. Single stage outlet guide vane in the secondary airflow.
3. Fan disk and fan blades.
4. Four stage booster stage stator assembly in primary airflow.
5. Twelve variable bleed valves.
6. Booster stator vanes.

The high-pressure compressor (HPC) assembly is designed to compress the air further for combustion preparation [42]. Some characteristics of the HPC structure are constant internal diameter, 9-stage, high speed, drum-disc, axial design [42]. It is understood that compression ratio (π) and energy transferred to the air decreases with every stage because compressed air is more difficult to compress, creating diminishing compression across the length of the system [42].

The benefits of having a constant internal diameter system include the idea that blades are longer than a constant external diameter would be, and thus less losses are induced by the boundary layer thickness. It also has a smaller size element allowing more volume for the secondary airflow and bleed air distribution. The smaller size also allows more space for the variable stator vane assembly which are configured across the first 4 stages of the HPC [42], as shown in figure 2.4.

The components of the high-pressure compressor (HPC) consists of [42]:

1. The compressor rotor.
2. The compressor front stator.
3. The compressor rear stator.
4. Variable stator vane assembly.
5. 4^{th}, 5^{th} and 9^{th} stage bleed air ducts.

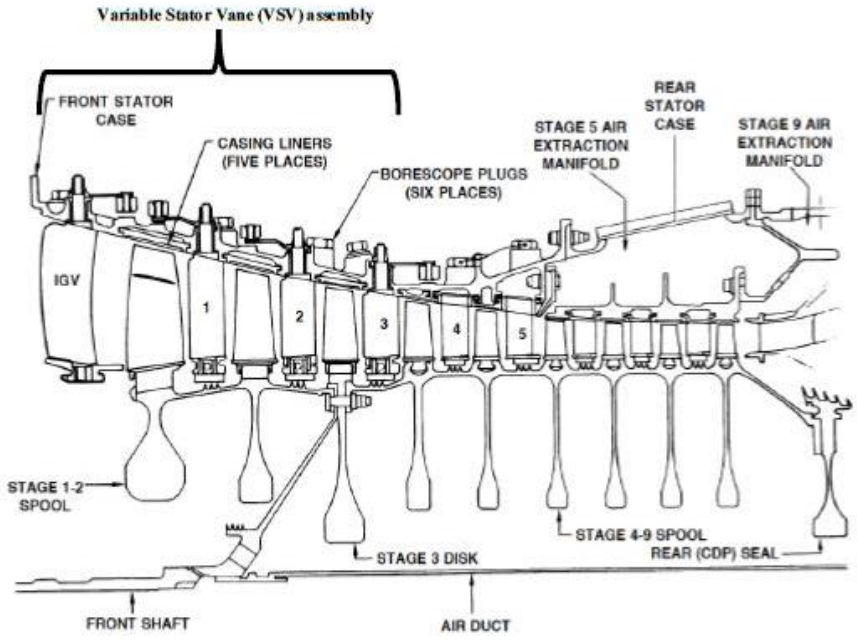

Figure 2.4 Outline of compressor sections in the CFM56-5A [42].

2.2.3 The turbines

The principal task of the turbine section is providing the power to drive the compressor and accessories, and in the case of applications that do not require solely the propulsive jet, the turbine can provide shaft power for a propeller or rotor [42]. Likewise, the compressor, the turbine is formed by several sets of static and movable blades [42]. Also, as in the compressor, for the CFM56-3, there are two turbines, the low-pressure turbine (LPT) feeds the low-pressure compressor (LPC), and the high-pressure turbine (HPT) feeds the high-pressure compressor [42].

When the hot gases resultant from the combustion process, force their way through the discharge nozzles of the turbine, they are accelerated close to the speed of sound, due to the convergent shape of the nozzle. Simultaneously, the gas flow is given a spin in the direction of rotation of the turbine blades by the nozzle guide vanes. During the expansion of these gases through the vanes, energy is absorbed which causes the turbine to rotate at high speed, and so providing the power necessary to drive the turbine shaft and its corresponding compressor. This process however involves high stresses in the turbine blades, and in order to achieve efficient operation, the turbines may be exposed to temperatures between 850^oC and 1700^oC , and may reach a velocity of $762\ m/s$ in certain parts of the turbine [44].

What defines this turbine inlet temperature, is the temperature resultant from the combustion process. In theory, in order to achieve the best performance, the burning temperature should be as high as that can be achieved from the complete combustion of the fuel and oxygen in the air [9]. Despite the advances in nickel alloys for the turbine's blades, these cannot fully withstand this high complete combustion temperature, so blade cooling techniques have been developed, with the aim of provide a film of cool air that protects the blade wall from the hot gases.

2.2.4 The Nozzle

The nozzle is the exhaust duct of the engine and has the function of providing thrust for the aircraft. The energy of the aircraft that passed the turbine stages, in addition to the cooler air that bypassed the engine core, meet at the exit of the nozzle and produce a force that acts to propel the engine forward, which is called thrust [9]. Thrust is generated in the propelling nozzle through a convergent duct. As the exhaust gases pass to the atmosphere through this propelling nozzle, the velocity of the gases increases, creating thrust.

The Bernoulli principle explains how the velocity of the flow is increased in a convergent nozzle; a convergent nozzle is a nozzle that starts big and then progressively its cross-sectional area gets smaller. As the fluid (air) enters the smaller cross-section, it must increase its velocity due to the conservation of mass [9].

2.2.5 Diffuser

To reduce the compressor outlet velocity to a value at which the combustor pressure loss is tolerable, it is customary to use a diffuser. It is also using to recover as much of the dynamic pressure as possible, and to present the liner with a smooth and stable flow. Until quite recently, there were two different philosophies regarding diffuser design, and both are illustrated in figure 2.5.

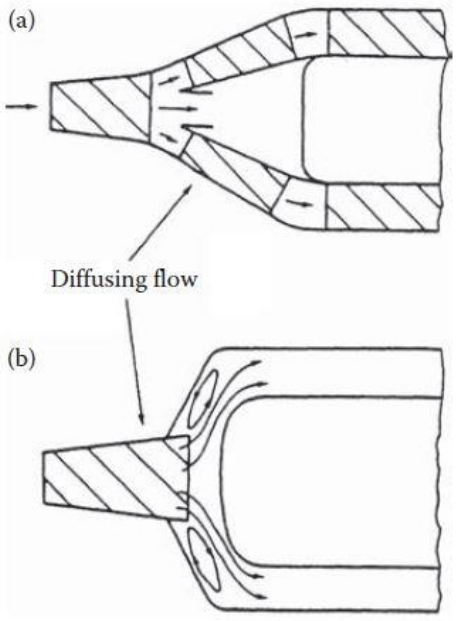

Figure 2.5 Two basic types of annular diffusers: (a) aerodynamic, (b) dump [1].

One is to employ a relatively long aerodynamic diffuser to achieve maximum recovery of dynamic pressure. The first section of the diffuser is located at or near the compressor outlet. Its purpose is to achieve some reduction in velocity, typically about 35%, before the air reaches the snout, at which point it divides and flows into three separate diffusing passages. The central diffuser passage discharges the remaining air into the dome region, which provides air for atomization and dome cooling [1].

The other main diffuser type is the “dump” or “step” diffuser. It consists of a short conventional diffuser in which the air velocity is reduced to almost half its inlet value. At exit, the air is then “dumped” and left to divide itself between air for the inner and outer annuli and dome air [1]. In table 2.3, are presented the merits and the drawbacks of the two types of diffusers describe above.

Table 2.3 Merits and drawbacks of the diffuser types.

Diffuser type	Merits	Drawbacks
Aerodynamic or faired	Low pressure loss.	Relatively long. Performance susceptible to thermal distortion and manufacturing tolerances. Performance and stability sensitive to variations in inlet velocity.
Drump	Relatively short. Insensitive to variations in inlet flow conditions.	Pressure loss about 50% higher than for faired type.

2.2.6 Jet Engine Performance

The engine thrust is proportional to the mass flow rate that goes through the engine, and the excess of the jet velocity over flight velocity. Hence, the specific thrust is an important engine design parameter for scaling engine size with thrust, at a given flight conditions. The specific thrust is defined as the ratio of the engine thrust to its mass flow rate. The equation 2.1 represents this relation:

$$\frac{F}{\dot{m}} = (V_5 - V_0) + (p_5 - p_0)A_5/\dot{m} \tag{2.1}$$

Another important parameter is the thrust specific fuel consumption (TSFC), which is the fuel efficiency of an engine design with respect to thrust output, in other words, the TSFC represents the ratio of mass flow rate of fuel consumption to the engine thrust, as shown in Eq. 2.2:

$$TSFC = \dot{m}_f/F \tag{2.2}$$

The efficiency of the air-standard Brayton-Joule cycle (η_{joule}), presented in figure, is given by Eq.2.3:

$$\eta_{joule} = 1 - \frac{1}{r_p^{(\gamma-1)/\gamma}} \tag{2.3}$$

2.3 The Combustor

The goal of the combustor is to convert the chemical energy bound in the fuel into thermal energy. This thermal energy will be used by the turbine to produce the power required to operate the various stages of compressors or in the case of an industrial GTE, the turbine produces the power required to turn a generator, which in turn produces electricity. [9]. It is important to understand the difference between the Combustor Chamber (CC) and the combustor [9]. The combustor includes all of the combustion systems, i.e. the diffuser, the

combustion chamber, the inner and outer casing, the spark plugs and the fuel injectors whereas the CC[11] refers to the exact place in which combustion takes place [9].

The combustor is a critical component in the GTE, because it must operate reliably at extreme temperature. It has to provide a suitable temperature for the turbine inlet, and it must produce a minimum amount of pollutants over a long operating life [9]. Figure 2.6 shows the CFM56-3 combustor.

Figure 2.6 CFM56-3 combustor photograph [9].

2.3.1 Combustor Performance Requirements

A gas turbine combustor must satisfy a wide range of requirements whose relative importance varies among engine types. The main requirements of all combustors may be listed following [1]:

1. The fuel should be completely burned so that all its chemical energy is liberated as heat.
2. Reliable and smooth ignition, both on the ground and, in the case of aircraft engines, after a flameout at high altitude.
3. The flame should stay alight over wide ranges of pressure and air/fuel ratio.
4. Low-pressure loss.
5. An outlet temperature distribution that is tailored to maximize the lives of the turbine blades and nozzle guide vanes.
6. Clean exhaust, i.e., low emissions of smoke and gaseous pollutant species.
7. Freedom from pressure pulsations and other manifestations of combustion- induced instability.
8. Size and shape compatible with engine envelope.

[11] In some literatures, the authors adopt names as flametube, liner or even burner for the CC [9].

9. Maintainability, durability and should be design for minimum cost and ease of manufacturing.
10. Petroleum, synthetic, and biomass-based multifuel capability.

For aircraft engines, size and weight are important considerations, whereas with industrial GTE's, a long operating life is the biggest consideration. However, for all the types of aircrafts, the priority requirements are the low fuel consumption and low pollutant emissions.

2.3.2 Basic Design features

In order to define the essential components needed to carry out the primary function of a combustion chamber [9]. It is of interest to begin by examining the simplest possible combustor, and then discuss the modifications that have to be made in order to produce a combustor that meets the performance requirements presented in section 2.3.1.

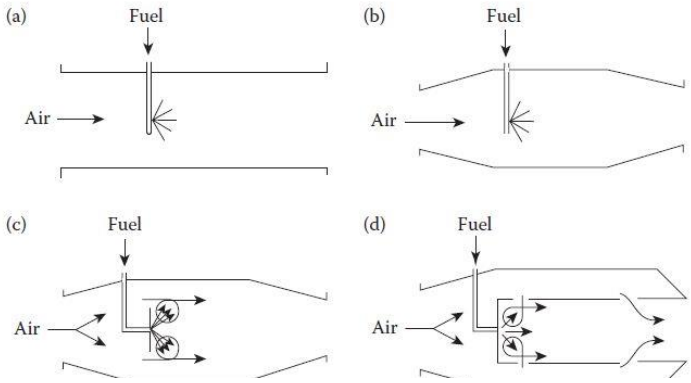

Figure 2.7 Stages in the evolution of the conventional aircraft combustor [1].

Figure 2.7.a shows the simplest possible form of combustor—a straight walled duct connecting the compressor to the turbine. Unfortunately, this simple arrangement is impractical because the pressure loss incurred would be excessive [1]. The fundamental pressure loss because of combustion is proportional to the square of the air velocity and, for compressor outlet velocities of the order of $170\ m/s$ this loss could amount to almost one-third of the pressure rise achieved in the compressor [1].

To reduce this pressure loss to an acceptable level, a diffuser is used to lower the air velocity by a factor of about 5 [1], as shown in figure 2.7 b.

Having fitted a diffuser, a flow reversal must then be created to provide a low-velocity region in which to anchor the flame. Figure 2.7.c shows how this may be accomplished with a plain baffle [1]. The only remaining defect in this arrangement is that to produce the desired temperature rise, the overall chamber air/fuel ratio must normally be between 30 and 40, which is well outside the limits of flammability for hydrocarbon–air mixtures. Ideally, the

air/fuel ratio in the primary combustion zone should be around 18, although higher values (around 24) are sometimes preferred if low emissions of nitric oxides is a prime consideration [1]. To deal with this problem, combustion is sustained by a recirculatory flow of burned products that provide a continuous source of ignition for the incoming fuel air mixture. The air not required for combustion is admitted downstream of the combustion zone to mix with the hot burned products, thereby reducing their temperature to a value that is acceptable to the turbine [1].

Figure 2.7 thus illustrates the logical development of the conventional gas turbine combustion chamber in its most widely used form. As would be expected, there are many variations on the basic pattern, shown in figure 2.7.d, but, in general, all chambers incorporate an air casing, diffuser, liner, and fuel injector as key components [1].

2.3.3 Combustor Types

The choice of a particular combustor type and layout is determined largely by the overall engine design, and by the need to use the available space as effectively as possible [1]. There are two basic types of combustor, tubular and annular. A compromise between these two extremes is the “tubo-annular” or “can-annular” combustor, in which a number of equispaced tubular liners are placed within an annular air casing [1]. The three combustor types are illustrated in figure 2.8.

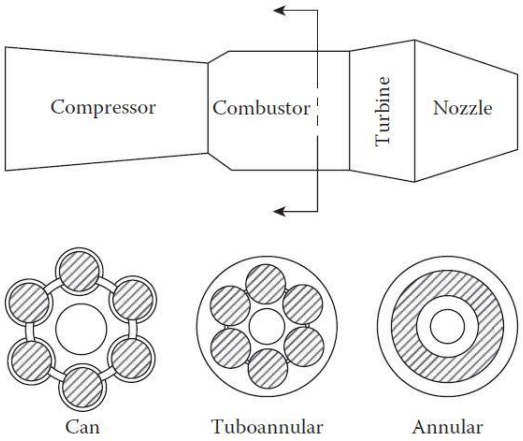

Figure 2.8 Illustration of three main combustor [1].

Can type

Can combustors, as known as a tubular combustor, are the simples form of the combustor and was used in early jet engines. A tubular chamber comprises a cylindrical flame-tube mounted concentrically inside a cylindrical casing [45], as shown in figure 2.9. Most of the early jet engines features tubular chambers, usually in numbers varying from eight to sixteen per engine, and even today a single of low power output [45]. However, for the big majority of aircraft

applications, the tubular system is too long and heavy and results in an engine of large frontal area and high drag [45].

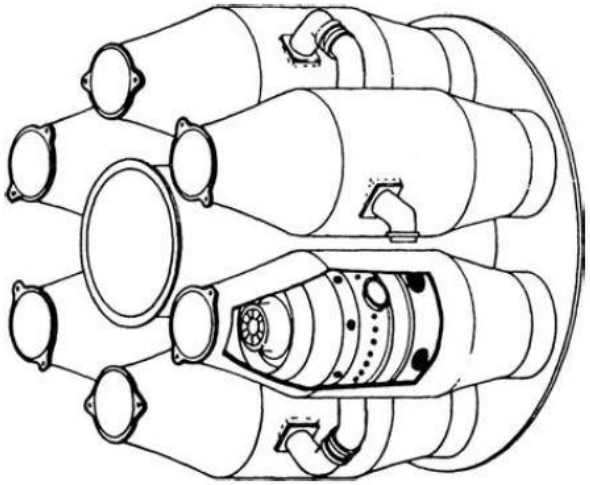

Figure 2.9 Can combustor arrangement [1].

Can Annular type

The can annular chamber (or “tubo-annular”) comprises a group of cylindrical flame tubes arranged inside a single annular casing [45], as illustrated in figure 2.10. It represents an attempt to combine the compactness of the annular chamber with the best features of the tubular system [45]. Compared with the annular design, the tubo-annular chamber has an important advantage in that much useful chamber development can be carried out with very modest air supplies , using just a small segment of the total chamber containing one or more flame – tubes [45].The main problem with tubo-annular chambers is that of achieving a satisfactory and consistent air-flow pattern; in particular the design of the diffuser can present serious difficulties [45]. Tubo- annular chambers are used extensively on large engines and engines of high-pressure ratio, although the current trend is towards a more widespread use of annular system [45].

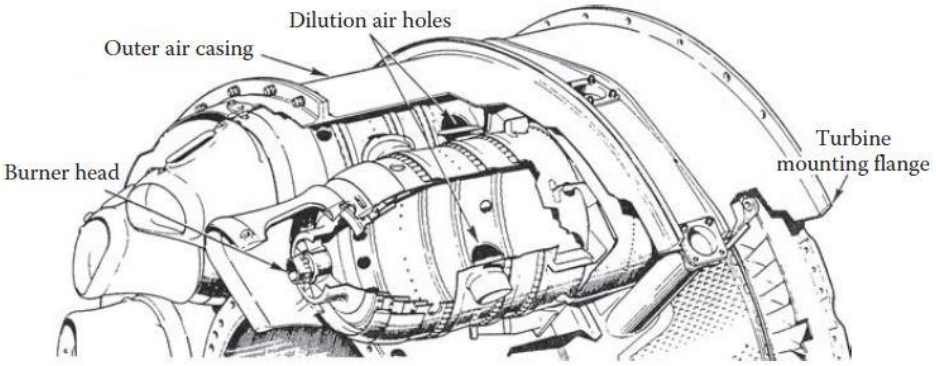

Figure 2.10 Can Annular combustor arrangement [1].

Annular type

The annular configuration is used by most modern jet engines because of its lighter design. The CFM56-3 combustor has an annular configuration. The annular combustor arrangement is illustrated in figure 2.11. In this type an annular flame -tube is mounted concentrically inside an annular casing [45]. It is an ideal form of chamber since its "clean " aerodynamic layout results in a compact unit of lower pressure loss than other camber design [45]. Unfortunately, one undesirable outcome of the annular system´s excellent aerodynamic characteristics is that a slight variation in the velocity profile of the inlet air can produce a significant change in the temperature distribution of the outlet gases [45].

Another problem with large annular chambers stems from the heavy buckling load on the outer flame -tube [45]. Distortion of the flame-tube disrupt the flow of cooling air and changes the outlet temperature distribution [45]. Test-bed development of annular chambers presents serious difficulties because there are very few facilities anywhere in the world that can supply air at the levels of pressure and temperature and in the amounts requires to test large annular combustion chambers at take-off conditions [45]. Here is a new field for research. In the past considerable time and ingenuity was spent in devising methods of simulation low combustion pressure in order to reproduce combustion conditions corresponding to high altitudes [45]. Today, with the trend towards more widespread use of annular designs, the urgent need is for methods of simulating high combustion pressures in chambers that are actually operating at lower and more convenient level of pressure. Figure 2.12 shows a cut-away of the annular combustion chamber [45].

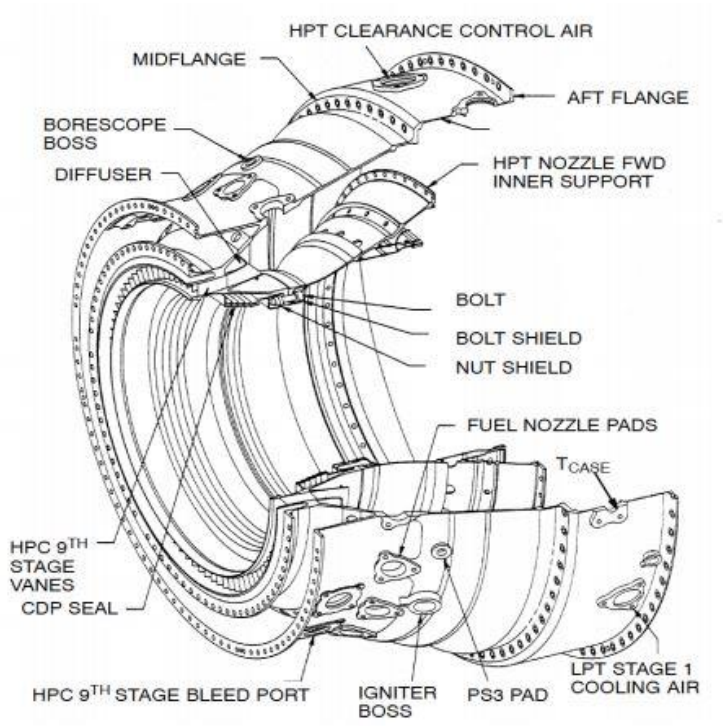

Figure 2.11 Annular combustor arrangement [42].

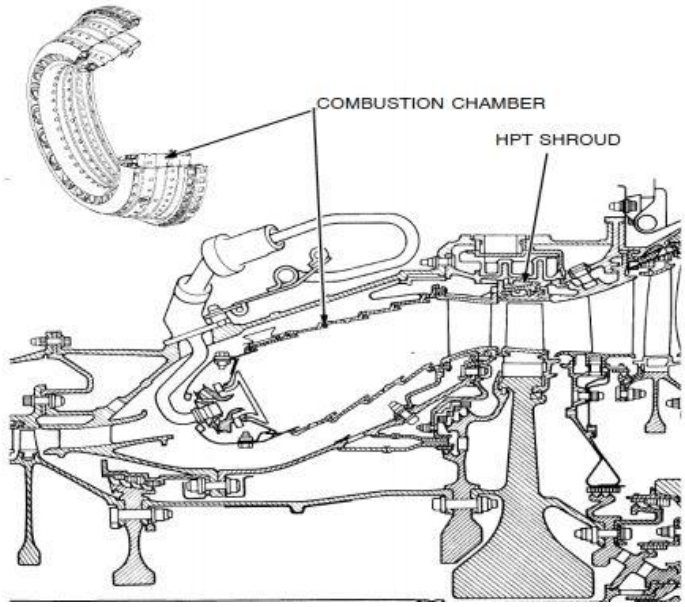

Figure 2.12 Combustion chamber cut-away [42].

Table 2.4. shows the advantages and disadvantages of the various combustor types.

Table 2.4 Advantages and disadvantages of the various combustor types [45].

Combustor types	Advantages	Disadvantages
Tubo-annular	Mechanically robust. Fuel-flow and airflow patterns are easily matched. Rig testing necessitates only small fraction of total engine air mass flow. Low pressure loss. Shorter and lighter than tubular chamber.	Less compact than annular. Requires connectors. Incurs problem of light-round.
Annular	Minimum length and weight. Minimum engine frontal area. Minimum pressure loss. Easy light-round.	Serious buckling problem on outer liner. Rig testing necessitates full engine air mass flow. Difficult to match fuel -flow and airflow patterns. Difficult to maintain stable outlet temperature traverse.
Tubular	Mechanically robust. Fuel-flow and airflow patterns are easily matched. Rig testing necessitates only small fraction of total engine air mass flow.	Bulky and heavy. High pressure loss. Requires interconnectors. Incurs problem of light-round.

2.3.4 Combustion process

The combustion of a given liquid fuel like kerosene, involves the mixing of a fine spray of droplets with air, the vaporisation of these droplets, the breaking down of heavy hydrocarbons into lighter fractions, the mixing of hydrocarbon molecule with oxygen molecules and the chemical reaction within themselves, completing the combustion process [9]. In order to make possible that such combustion with a moving air stream, occurs in a small place, a high temperature, such as is provided by the combustion of an approximately stoichiometric mixture is necessary. As mentioned before, the overall air-fuel ratios (AFR) at which GTC operate at full power is between 30 and 40, it is necessary to introduce the air through three stages, which are so named primary, secondary and dilution zones [9].

2.3.4.1 Primary zone

The main function of the primary zone is to anchor the flame and provide enough time, temperature, and turbulence in order to enable the complete combustion of the incoming fuel-air mixture. The air that exists from the compressor, is injected through four injection points, in which two are used to inject the air into the primary zone [9], these are the swirler and primary air walls jets and they have the function to control the structure as well as the mixing within the primary zone, as shown in figure 2.13.

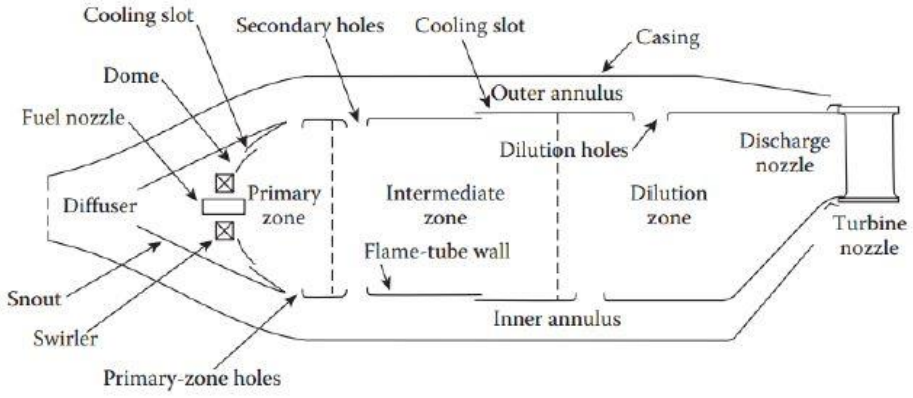

Figure 2.13 Nomenclature of the interior of the combustion chamber [42].

The Swirler

The swirler has a main objective to keep combustion steady and continuous. In this study, the swirler is of the Twin Annular Premixing Swirler (TAPS) type. The swirler vanes are positioned at the front face of the combustor and typically surround the fuel injection points and are the first entry point for the air that comes from the compressor [9], as shown in figure 2.14. The swirler induces air recirculation, where the fuel is mixed and forces the gases to circulate to ensure that the combustion is to be continued. A reverse flow zone is produced in the primary combustion zone [43].

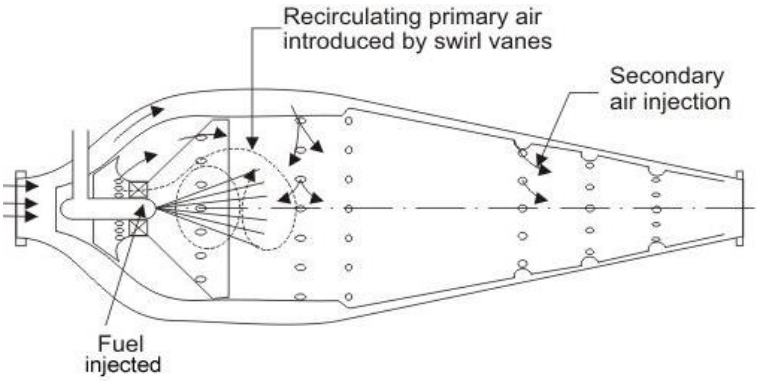

Figure 2.14 Combustion chamber with swirl vanes [43].

Primary air jets

The air jets for the primary zone have two functions: the first to force the toroidal flow in staying within the limits of the primary zone, by providing a strong force against which the primary zone cannot easily penetrate; secondly, the primary air jets bifurcate with a substantial percentage of the flow directed upstream, in order to mix with the toroidal flow that contains the fuel -air mixture, and the remainder air mixes downstream into the secondary zone [9].

The fluid mixing and the chemical kinetics occurs in parallel in the primary zone, with a range of scales [9]. In the zone of recirculation and within the macro scale, exists and persists a range of turbulent eddy scales, during a finite lifetime, before breaking up and mixing with adjacent eddies, and forming a new eddy [9]. Some of these eddies contain unreacted fuel and air, but will ignite; however, and those who will not ignite, have to mix with other eddies, in order to acquire the necessary mixture ratio, that is required for ignition [9].

2.3.4.2 Secondary Zone

The secondary zone, also known as intermediate zone, has as main functions to oxidize the CO to CO_2 and reduce dissociation losses by allowing recombination of dissociated species before the dilution zone. The principal elementary kinetic reaction that governs the oxidation is represented in 2.4:

$$CO + OH \Rightarrow CO_2 + H \tag{2.4}$$

If the primary-zone temperature is higher than $2000\,K$, dissociation reactions will result in the appearance of significant concentrations of CO and H_2 in the efflux gases [1]. Should these gases pass directly to the dilution zone and be rapidly cooled by the addition of massive amounts of air, the gas composition would be “frozen,” and CO, which is both a pollutant and a source of combustion inefficiency, would be discharged from the combustor unburned [1].

To avoid such situation and improve the combustion efficiency, three strategies were adopted for the secondary zone [46]:

1. An overall lean mixture ratio, through the primary jet bifurcation was established.
2. The temperature was dropped to an intermediate level by the addiction of small amounts of air, encouraging the burnout of soot and allowing the combustion of CO and UHC to proceed to completion.
3. A residence time was provided to promote the oxidation.

The length of the secondary zone is ideally dictated partly by the minimum length needed to mix the intermediate air with gas flow and by the minimum residence time needed for complete combustion [9]. The typical length is then ½ of the total length of the combustion chamber [46].

2.3.4.3 Dilution zone

The dilution zone is located at the end of the combustor chamber and is the zone in which the gases resultant from the combustion process exit [9]. This zone has as main function to admit air and mix it with the gases remaining after the combustion, allowing wall-cooling requirements to be met, and to provide an outlet stream with a temperature distribution that is acceptable to the turbine. The temperature distribution is described by terms "Pattern Factor" or "Temperature Traverse Quality" (TTQ).

The amount of air available for dilution is usually between 20 and 40% of the total combustor airflow. It is introduced into the hot gas stream through one or more rows of holes in the liner walls. The size and shape of these holes are selected to optimize the penetration of the air jets and their subsequent mixing with the main stream [1].

In theory, any given traverse quality can be achieved either using a long dilution zone or by tolerating a high liner pressure-loss factor. The gases may leave a modern combustor at a temperature around 1873K, and the materials used in the turbine blades melt at a temperature of 1473K [44]. For this temperature, an ideal Pattern Factor would be one that gives minimum temperature at the turbine blade root. A Pattern Factor, represented by Eq. 2.5, reflects the extent to which the maximum temperature diverges from the average temperature rise across the combustor and is the parameter of most significance to the design of nozzle guide vanes.

$$Pattern\ Factor = \frac{T_{max} - T_4}{T_4 - T_3} \tag{2.5}$$

Temperature Traverse Quality (TTQ), also known as the temperature profile, is characterized by various indices, which include the "Pattern Factor", "Profile Factor" and "Turbine Profile Factor". Achieving a satisfactory and consistent distribution of temperature in the efflux gases discharging into the turbine. is the most important, and at the same time, the most difficult problems in the design and development of gas turbine combustion chambers; in fact, the actual temperature traverse quality profile can deviate from the design profile, as shown in figure 2.15.

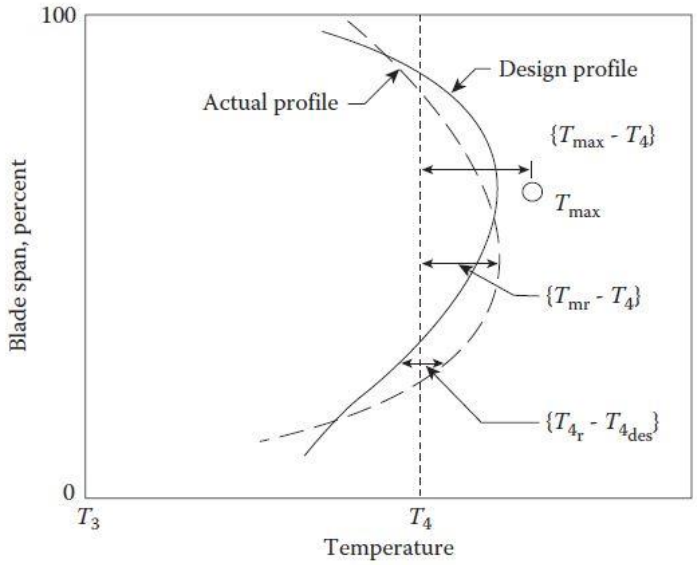

Figure 2.15 Explanation of terms in exit-temperature profile parameters [1].

The temperature with most significance for the turbine blades, are those that constitute the average radial profile. The profile factor, as shown in Eq. 2.6, characterizes the extent to which the maximum circumferential mean temperature, T_{mr}, deviates from the average temperature rise across the combustor.

$$Profile\ Factor = \frac{T_{mr}-T_4}{T_4-T_3} \tag{2.6}$$

The pattern factor and profile factor are best suited for situations where a perfectly uniform exit-temperature distribution would be considered ideal [9]. However, in modern high-performance engines, which employ extensive air cooling of both nozzle guide vanes and turbine blades, the desired average radial distribution of temperature at the combustor exit plane is far from flat; instead, it usually has a profile that peaks above the midheight of the blade [1].

A parameter that takes the design profile into account is the turbine profile factor, as shown in Eq. 2.7, is the maximum temperature difference between the average temperature at any given radius around the circumference, $T_{3,r}$, and the design temperature for that same radius, $T_{3,des}$.

$$Turbine\ Profile\ Factor = \frac{(T_{4,r}-T_{4,des})ma}{T_4-T_3} \tag{2.7}$$

2.3.5 The ignition process

Most common fuel and oxidisers combine at a slow rate when subjected to ambient conditions, thus if an activation energy is not externally supplied, the acceleration of the reaction will not happen [9].

Regarding CTG´s, the ignition process occurs in 3 phases according to the following description:

- Phase 1 is the formation of a kernel of flame of enough size and temperature to be capable of propagation. This phase is also affected by the design of the igniter plug—*flush fire* or *sunken fire*, by its location, and by the extent to which the plug tip protrudes through the liner wall. Survival of the kernel of flame depends entirely on whether or not the rate of heat release by combustion within the kernel exceeds the rate of heat loss to the surroundings by radiation and turbulent diffusion [1].
- Phase 2 is the subsequent propagation of flame from this kernel to all parts of the primary zone. The location of the igniter is important in this phase because it determines whether the hot kernel is entrained into the primary-zone reversal or is swept away downstream. This phase is also governed by all the factors that control flame stability. Thus, an increase in pressure and/or temperature, or a reduction in primary-zone velocity, or any change in fuel/air ratio toward the stoichiometric value, all of which are beneficial to stability, will also improve phase 2 [1].
- Phase 3, which applies only to tubular and tubo-annular designs of chamber, is the spread of flame from a lighted liner to an adjacent unlighted liner. The present phase is aided using interconnectors, in which the flow area is made large in order to facilitate the passage of flame, and whose length is kept short to minimize heat loss by external convection to the annulus air [1].

If the ignition performance of a combustion chamber is unsatisfactory, the first step is to find out in which phase the bottleneck is arising. This information can be obtained quite readily by examining the position of the ignition loop in relation to the stability limits [1].

Since the flow properties that control stability exercise a similar influence on ignition behaviour, it might be expected that ignition and stability limits should coincide. Stability limits, however, relate essentially to burning conditions and high metal temperatures, whereas ignition is inevitably associated with cold liner walls and comparatively high heat losses [1]. For this reason, the two limits can never be the same, but the object of ignition development is to ensure that they are separated only by the effects of heat loss.

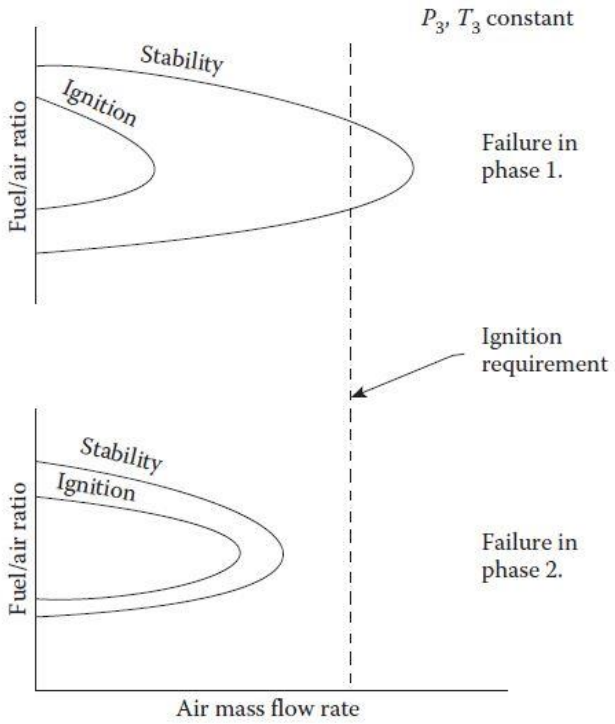

Figure 2.16 Curves illustrating the two main types of ignition failure [1].

If the ignition loop lies well inside the stability loop, this indicates that the limitation on ignition performance is arising in phase 1. This may be checked by changing the spark energy, which should produce a corresponding change in the ignition loop. If the ignition and stability loops lie in proximity, the bottleneck on performance is almost certainly in phase 2. These points are illustrated in figure 2.16. Failure in phase 3 is indicated when the maximum relighting altitude is significantly less than the value predicted from rig tests carried out on a single liner [1].

2.3.6 Atomization

The atomization process represents a disruption of the consolidating influence of surface tension by the action of internal and external forces [1]. In the absence of such disruptive forces, surface tension tends to pull the liquid into the form of a sphere, which has the minimum surface energy. Liquid viscosity has an adverse effect on atomization because it opposes any change in system geometry [1].

The atomization process is generally regarded as comprising two separate processes; primary atomization, in which the fuel stream is broken up into shreds and ligaments, and secondary atomization, in which the large drops and globules produced in primary atomization are further disintegrated into smaller droplets.

2.3.6.1 Breakup of Drops

The balance between dynamic pressure, surface tension and viscous forces controls the breakage of the drop. Weber's number relates this balance, We, which is the ratio of the disruptive aerodynamic force, represented by Eq.2.8:

$$We = \rho_A U_R^2 D/\sigma \tag{2.8}$$

The higher the Weber number, the larger the deforming external pressure forces, compared with the restoring surface tension forces [1]. The critical condition for drop breakup is achieved when the aerodynamic drag is just equal to the surface tension force, as show in Eq.2.9:

$$C_D \frac{\pi D^2}{4} 0.5 \rho_A U_R^2 = \pi D \sigma_L \tag{2.9}$$

Through this equation we can come to the number of Weber, as represented in Eq.2.10 and Eq.211, and the critical conditions that will cause drop instability.

$$\left(\frac{\rho_A U_R^2 D}{\sigma_L}\right)_{crit} = \frac{8}{C_D} \tag{2.10}$$

$$We_{crit} = \frac{8}{C_D} \tag{2.11}$$

For a drop to remain stable relates the surface tension of the liquid to external factors, the maximum stable drop size is obtained from Eq.2.12:

$$D_{max} = \frac{8\sigma_L}{C_D \rho_A U_R^2} \tag{2.12}$$

The Ohnesorge number (Oh) is a dimensionless number that relates the viscous forces to inertial and surface tension forces, as represented in Eq.2.13. This number is fundamental in understanding of atomization processes in viscous liquids.

$$\frac{\sqrt{We}}{R_e} = \frac{\mu_L}{(\rho_L \sigma_L d_0)^{0.5}} \tag{2.13}$$

The effect of viscosity on the critical Weber number can be expressed as Eq.2.14:

$$We_{crit} = We_{crit} + 14Oh^{1.6} \tag{2.14}$$

In Eq. 2.14, We_{crit} symbolizes the critical Weber number for zero viscosity.

When there is an increase in viscosity, the number of Oh will increase, and Weber's number will increase as well, making the atomization process more difficult [47].

2.3.6.2 Breakup of Fuel Jets

It is verified that, for invariant liquids under laminar flow conditions, disturbances with wavelengths greater than the perimeter of the liquid jet cause deformations, which eventually lead to the disintegration of the jet [47].

When the wavelength of the disturbances is less than the minimum length, the surface forces dampen the disturbances and stabilize the jet. When the opposite occurs, the wavelength of the perturbations is greater than the minimum length, represented in Eq.2.15, the surface forces increase the perturbations, causing instability and consequent disintegration of the jet [47]. So, it is possible calculate an optimum wavelength for the formation of new drops, as represented in Eq. 2.16.

$$\gamma_{min} = \pi d_0 \tag{2.15}$$

$$\gamma_{opt} = \sqrt{2\pi d_0}\left(1 + \frac{3\mu_L}{\sqrt{\rho_L \sigma_L d_0}}\right)^{0.5} \tag{2.16}$$

In the jet disintegration process the effect of increasing the relative velocity between the liquid and the air in the development and induction of perturbations is also verified. Some studies have shown results on the breaking of liquid jets at high viscosities, and it was concluded that, the ratio of the optimum wavelength to the outlet diameter of liquid, varies between 30 and 40, while for non-viscous liquids does not exceed 5 [47].

The disintegration mechanisms of the jet are complex, unstable and depend greatly on the conditions and operating regimes. These mechanisms are divided into three independent jet disintegration regimes, and these are expressed by the numbers Re and Oh, as shown in figure 2.17.

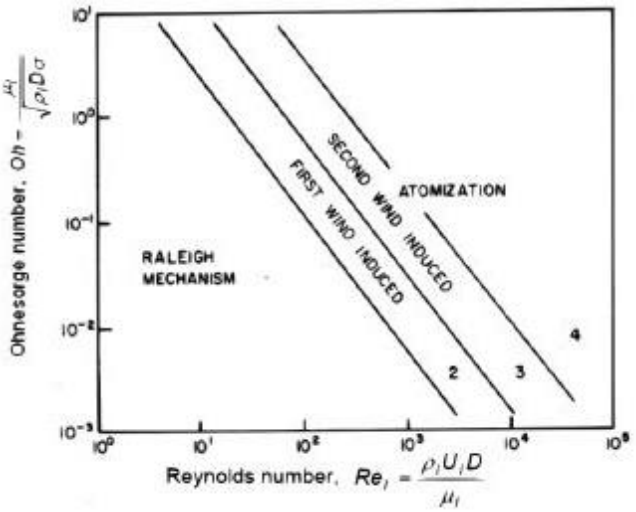

Figure 2.17 Influence of Reynolds number on jet disintegration [48].

2.3.7 Fuel Injection

There are two different methods in which fuel can be supplied to the airstream, in order to form the fuel-air mixture; these are through vaporizers and fuel spray nozzles. The fuel spray nozzles compromise the two main types of pressure-jets and air spray injectors and are the type of fuel injection adopted for the CFM56-3 combustor. Due to this fact, in this section will give a general view on the vaporizers and focus on the fuel spray nozzles.

2.3.7.1 Vaporizers

An alternative method of preparing a liquid fuel for combustion is by heating it above the boiling point of its heaviest hydrocarbon ingredient, so that it is entirely converted to vapor before combustion. This method is applicable only to such high-grade fuels as can be completely vaporized, leaving no solid residue.

An alternative and much simpler method of vaporization is to inject the fuel, along with some air, into tubes that are immersed in the flame [1]. The injected fuel–air mixture is heated by the tube walls and, under ideal conditions, emerges as a mixture of vaporized fuel and air. The remainder of the combustion air is admitted through apertures in the liner wall and reacts with the fuel–air mixture issuing from the tubes [1].

Vaporizing systems have useful advantages in terms of low cost, modest fuel-pump pressure requirements, and low soot formation. Their drawbacks include risk of thermal damage to the vaporizing elements and sensitivity to variation in fuel type [1].

Some of the early designs were generally known as “walking stick”, as represented in figure 2.18, or “candy cane” vaporizers.

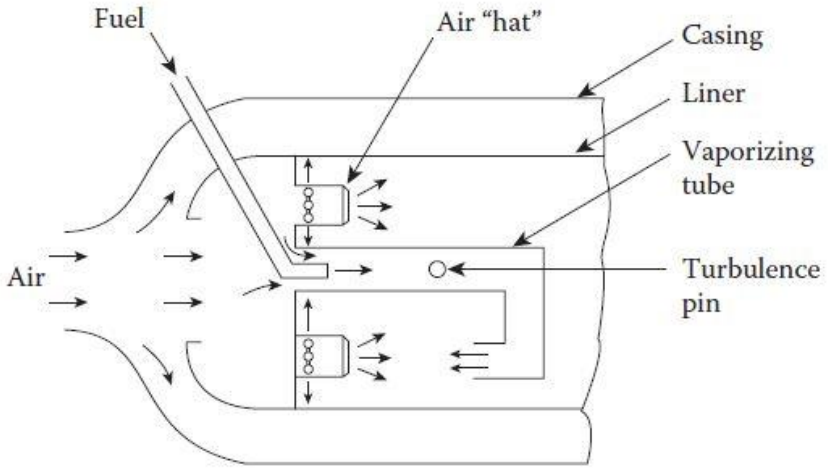

Figure 2.18 “Walking stick” vaporizing system [1].

2.3.7.2 Fuel spray nozzles

Liquid fuels such as kerosene, have to be atomized and well mixed with air, before combustion [9]. The process of atomization is one in which a liquid jet or sheet is disintegrated by the kinetic energy of the liquid itself or by exposure to high velocity air or gas [9]. To achieve this, fuel spray nozzles are used, which can be distinguished by pressure, air-blast and air-assist atomizers [9].

Pressure atomizers

The main function of the pressure atomizers is the conversion of pressure into kinetic energy to achieve a high relative velocity between the fuel and the surrounding air or gas. Many of the atomizers in general use are of this type. They include plain-orifice and simplex nozzles, as well as the dual-orifice injector. These various types of pressure atomizers are discussed below.

In the plain orifice the atomization, of a low-viscosity fuel, is most easily accomplished by passing it through a small circular hole, as illustrated in figure 2.19 a. If the velocity is low, the liquid emerges as a thin distorted pencil, but if the liquid pressure exceeds the ambient gas pressure by about 150 kPa [1], a high-velocity fuel jet is formed, which rapidly disintegrates into a well-atomized spray. Disintegration of the jet is promoted by an increase in fuel-injection pressure, which increases both the level of turbulence in the fuel jet and the aerodynamic forces exerted by the surrounding medium [1]. Perhaps the best known application of plain-orifice atomizers is to afterburners (reheat systems), where the fuel-injection system normally consists of one or more circular manifolds supported by struts inside the jet pipe [1].

Fuel is supplied to the manifolds by feed pipes in the support struts and is sprayed into the flame zone from holes drilled in the manifolds [1]. Sometimes “stub pipes” are used instead of manifolds, and many fuel injector arrays consist of stub pipes mounted radially on circular manifolds. In all cases, the objective is to provide a uniform distribution of well-atomized fuel throughout the portion of the gas stream that flows into the combustion zone [1].

The simplest form of pressure-swirl atomizer is the *simplex* atomizer, as illustrated in figure 2.19.b. Fuel is fed into a swirl chamber through tangential ports that give it a high angular velocity, thereby creating an air-cored vortex. The rotating fuel flows through the final orifice, i.e. the outlet from the swirl chamber, under both axial and radial forces to emerge from the atomizer in the form of a hollow conical sheet [1].

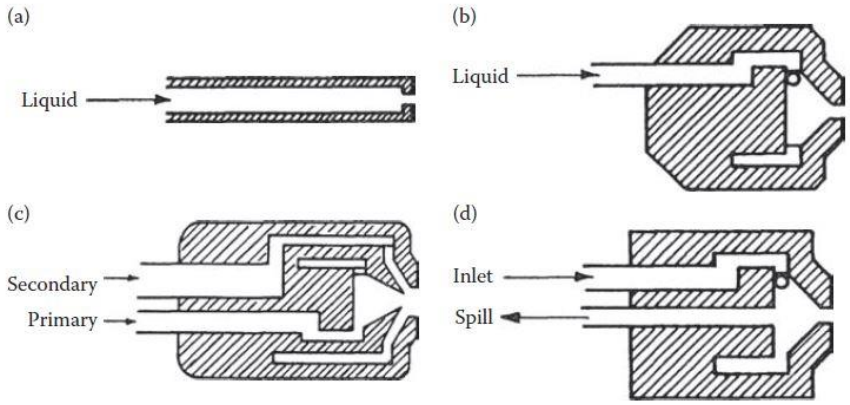

Figure 2.19 Schematic drawings of pressure-swirl atomizers: (a) plain orifice; (b) simplex; (c) dual orifice; (d) spill return [1].

The development of the spray passes through several stages as the fuel injection pressure is increased from zero [1]. These stages are then the following [1]:

1. Fuel dribbles from the orifice.
2. Fuel leaves as a thin distorted pencil.
3. A cone forms at the orifice but is contracted by surface tension forces into a closed bubble.
4. The bubble opens into a hollow “tulip” shape, where the fuel disintegrates into large drops.
5. The curved surface straightens to form a conical sheet. As the sheet expands, its thickness diminishes, and it soon becomes unstable and disintegrates into ligaments and then drops in the form of a well-defined hollow-cone spray.

The dual orifice fuel nozzle, as shown in figure 2.19. c is the one that can be most found in modern-day engine. The essential features of a dual-orifice atomizer, also known as duplex nozzle, because comprises two simplex nozzles that are fitted concentrically, one inside the other. The primary nozzle is mounted on the inside, and the juxtaposition of primary and secondary is such that the primary spray does not interfere with either the secondary orifice or the secondary spray within the orifice, as shown in figure 2.20. This arrangement allows the atomizer to offer an effective atomization over a wide flow range than the simplex spray nozzle, for the same fuel pressure [49].

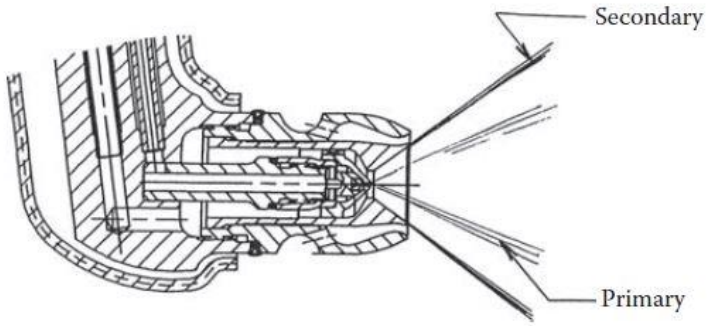

Figure 2.20 Dual-orifice atomizer [1].

The spill return is basically a simplex atomizer, except that the rear wall of the swirl chamber, contains a passage through which the fuel that is surplus to combustion requirements enters the spill line and is returned to the fuel tank. In this system the fuel-injection pressure is always high, even at the lowest fuel flow rate, thus atomization quality is always excellent. Other characteristic of the spill return is the absence of moving parts and, because the flow passages are designed to handle large flows all the time, freedom from "plugging" by contaminants in the fuel. The spill return is disadvantageous because the problems of metering the flow rate are more complicated than with other types of atomizer, and a larger-capacity pump is needed to handle the large recirculating flows.

Air assist atomizers

An alternative approach to atomizing fuel, is to use air to assist with the atomization process. Unlike simplex atomizers which purely depend on the fuel injection pressure, air assist nozzles use a small quantity of high velocity air supplied from a pump to help with atomization. In this design, a slow-moving stream of liquid is exposed to a high velocity stream of air, where a large difference in the relative velocity results in a shearing process, tearing up the fluid and atomizing it [50]. The two different types of air assist nozzles are: internal and external mixing air assist nozzles, as shown in figure 2.21.

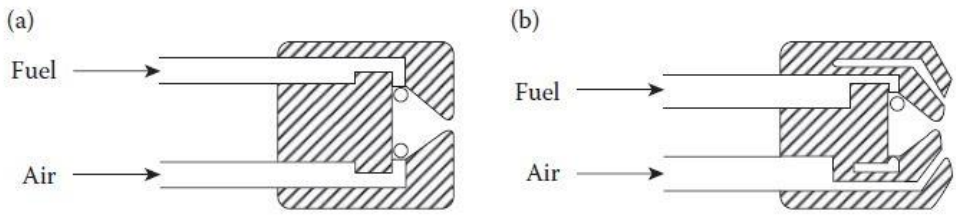

Figure 2.21 Schematic drawings of air-assist atomizers: (a) internal mixing; (b) external mixing [1].

In the internal-mixing configuration, shown schematically in figure 2.21.a, air and fuel mix within the nozzle before exiting through the outlet orifice. The fuel is sometimes supplied through tangential slots to encourage a conical spray pattern. However, the maximum spray angle is usually about 60° [1]. As its name suggests, in the external-mixing form of the air-assist nozzle, the high-velocity air impinges on the fuel downstream of the discharge orifice, as illustrated in figure 2.21.b. Its advantage over the internal-mixing type is that problems of back pressure are avoided because there is no internal communication between air and fuel [1]. However, it is less efficient than the internal-mixing concept, and higher airflow rates are needed to achieve the same degree of atomization. Both types of nozzles can effectively atomize high-viscosity liquids [1].

Air blast atomizers

In principle, the air blast atomizer functions in the same manner as the air-assist atomizer because both employ the kinetic energy of a flowing airstream to shatter the fuel jet or sheet into ligaments and then drops [49]. The main difference between the two systems lies in the quantity of air used and its atomizing velocity [49].

With the air-assist nozzle, where the air is supplied from a compressor or a high-pressure cylinder, it is important to keep the airflow rate down to a minimum [1]. However, as there is no special restriction on air pressure, the atomizing air velocity can be made very high. Thus, air-assist atomizers are characterized by their use of a relatively small quantity of very high-velocity air. However, because the air velocity through an air blast atomizer is limited to a maximum value (usually around 120 m/s), corresponding to the pressure differential across the combustor liner, a larger amount of air is required to achieve good atomization [1]. However, this air is not wasted because after atomizing the fuel, it conveys the drops into the combustion zone, where it meets and mixes with the additional air employed in combustion. Air blast atomizers have many advantages over pressure atomizers, especially in their application to combustion systems operating at high pressures [1].

They require lower fuel-pump pressures and produce a finer spray. Moreover, because the air blast atomization process ensures thorough mixing of air and fuel, the ensuing combustion process is characterized by very low soot formation and a blue flame of low luminosity, resulting in relatively low flame radiation and a minimum of exhaust smoke [1]. The merits of the air blast atomizer have led to its installation in a wide range of aircraft, marine, and industrial gas turbines [1].

2.3.8 Film cooling

The temperature of the gases released by combustion is about 1800^oC to 2000^oC , which is far too hot for entry to the nozzle guide vanes of the turbine. The air not used for combustion, which amounts to about 60% of the total airflow, is therefore introduced progressively into the

flame tube. Approximately a third of this is used to lower the gas temperature in the dilution zone before it enters the turbine and the remainder is used for cooling the walls of the flame tube [44]. The most common way of cooling the combustion chamber is by film cooling. The film cooling is usually reserved for methods of supplementing the removal of heat from the liner involve a film of cooling air on the inner surface of the liner wall that employ a few annular slots through which air is injected axially along the inner wall of the liner to provide a protective film of cooling air between the wall and the hot combustion gases.

The cool film is gradually destroyed by turbulent mixing with the hot gas stream, so normal practice is to provide a succession of slots at about 40–80 mm intervals along the length of the liner [1]. At the downstream end of the liner, the flow acceleration in the nozzle tends to suppress the hot stream turbulence, and the cooling film can persist for a much greater distance. There are few film-cooling techniques, however, this section will focus on the film-cooling techniques applied to the CFM56-3 combustor, as represented in figure 2.22.

The primary film cooling techniques applied in the CFM56-3 combustor, is the stacked ring device. This device uses total pressure feed[12]. The air-admission holes are drilled or punched, their dimensional accuracy is higher than other film-cooling devices, resulting in smaller variations in cooling airflow rate. The total flow area of these holes is calculated to meter the required amount of cooling air. The aft end of the previous liner panel provides a plenum in which turbulence is dissipated and the individual jets coalesce to form a single annular sheet of air. At its downstream end, the gap width is dimensioned to give the required cooling-air velocity [1]. The CFM56-3 combustor presents 5 slots of stacked rings in each side of the combustor chamber wall, with an average of 600 holes in each slot [9].

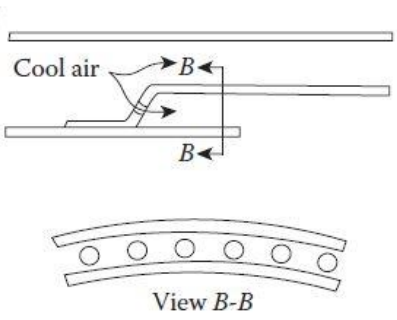

Figure 2.22 Stacked ring [1].

One slot of machined rings is also implemented in CFM56-3 combustor. Conduction of heat through brazed joints is essential to liner-wall cooling, and voids in the braze filler material can lead to local hot spots. This problem does not arise in the “machined ring” liner, which is machined either from a single piece of metal or from several rings welded together. As shows

[12] The difference between the total and static pressure feed can be notice in figure 2.23.

the figure 2.23, rows of holes are then drilled to allow annulus air to enter the cooling slot by either total-head feed, static pressure differential, or a combination of both.

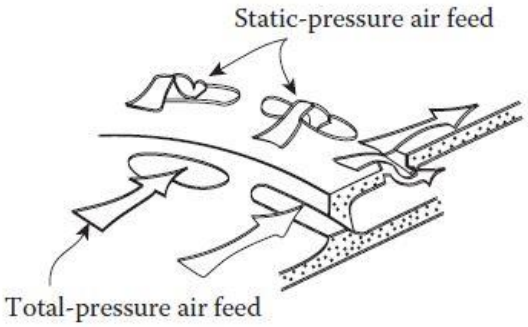

Figure 2.23 Machined ring [1].

2.4 Combustion Chamber performance

2.4.1 Pressure loss

A combustion chamber must be capable of allowing fuel to burn efficiently over a wide range of operating conditions without incurring a large pressure loss. In addition, if flame extinction occurs, then it must be possible to relight, so the flame tube and spray nozzle atomizer components must be mechanically reliable. The gas turbine engine operates on a constant pressure cycle, therefore any loss of pressure during the process of combustion must be kept to a minimum. In providing adequate turbulence and mixing, a total pressure loss varying from about 3 to 8% of the air pressure at entry to the chamber is incurred [44].

Saravanamuttoo et al. [8] states that when the pressure loss is expressed non-dimensionally in terms of the dynamic head, it will not vary much over the range of the Reynolds number, under which combustion system operate. Thus, the overall Pressure Loss Factor (PLF) can be expressed by Eq. 2.17:

$$PLF = \frac{\Delta p_0}{m^2/(2\rho_1 A_{max}^2)} = K_1 + K_2\left(\frac{T_{02}}{T_{01}} - 1\right) \quad (2.17)$$

In Eq.2.17, K_1 and K_2 are determined from combustion chamber on a test rig from a cold run and a hot run, respectively. Table 2.5 represents the PLF in the various type of CC´s, representing the losses that arise from turbulence and friction that can be measured with accuracy from cold flow.

Table 2.5 PLF in CC´s [1].

Type of chamber	PLF
Annular	20
Tubo-annular	28
Tubular	37

2.4.2 Combustion Intensity

The heat released by a combustion chamber or any other heat generating unit is dependent on the volume of the combustion zone. Thus, to obtain the required high-power output, a comparatively small and compact gas turbine combustion chamber must release heat at exceptionally high rates [44].

The combustion intensity is a very important parameter because it evaluates the maximum possible conversion rate of reactants for a given volume of combustion chamber [9]. The combustion intensity is also important for aero GTE´s, due to the need of their maximum size reduction [9]. The combustion intensity $(f(\xi))$ is expressed in Eq.2.18:

$$f(\xi) = \frac{\dot{Q}}{Vp^n} \tag{2.18}$$

In which $\dot{Q}$ is the heat release rate and p is the pressure and may employ p^{1-8} with the units $kW/m^3 atm^{1-8}$. In aircraft systems, the combustion intensity lies between 2×10^4 and $5 \times 10^4\ kW/m^3 atm$.

2.4.3 Combustion Efficiency

Failure to achieve high levels of combustion efficiency is generally regarded as unacceptable, partly because combustion inefficiency represents a waste of fuel, but mainly because it is manifested in the form of pollutant emissions, such as unburned hydrocarbons and carbon monoxide [1]. That is why current emissions regulations call for combustion efficiencies in excess of 99% [1]. The combustion efficiency of most gas turbine engines at sea-level take-off conditions is almost 100%, reducing to 98% at altitude cruise conditions, as shown in fig 2.24.

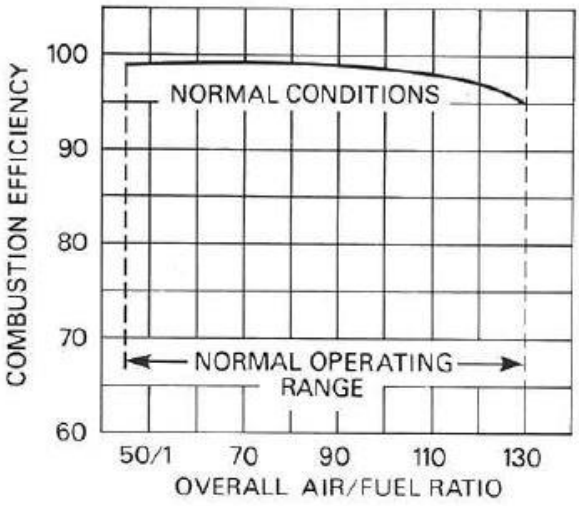

Figure 2.24 Combustion efficiency and air/fuel [44].

To avoid the production of "white" smoke, efficiency must exceed 96% and at no point in the operating cycle it is less than 90%. High combustion efficiency is necessary at this "off design" point because, with the engine windmilling, the pressure and temperature of the air flowing through the combustor are close to ambient values [1].

An important requirement, from a design viewpoint, is a means of relating combustion efficiency to the operating variables of air pressure, temperature, and mass flow rate, and to the combustor dimensions [1]. Unfortunately, the various processes taking place within the combustion zone are highly complex and a detailed theoretical treatment is precluded at this time [1]. Until more information is available, suitable parameters for relating combustion performance to combustor dimensions and operating conditions can be derived only using very simplified models to represent the combustion process [1]. One such model starts from that the total time required to burn a liquid fuel is the sum of the times required for fuel evaporation, mixing of fuel vapor with air and combustion products, and chemical reaction. The combustion efficiency (η_c) can be expressed by Eq. 2.19:

$$\eta_c = f(airflow\ rate\ )^{-1}(\frac{1}{evaporation\ rate} + \frac{1}{mixing\ rate} + \frac{1}{reaction\ rate})^{-1} \qquad (2.19)$$

In practical combustion systems, the maximum rate of heat release under any given operating conditions may be governed by either evaporation, mixing, or chemical reaction, but rarely by all three at the same time [1]. But, when the combustion process is in transition from one regime to another, two of the three key rates will participate in determining the overall combustion efficiency (η_c) .

2.4.4 Combustion Stability

In combustion parlance, the term "stability" is often used rather loosely to describe either the range of fuel/air ratios over which stable combustion can be achieved, also can be a measure

of the maximum air velocity the system can tolerate before flame extinction occurs [1]. For any type of combustion chamber there is both a rich and weak limit to the air/fuel ratio, beyond which the flame is extinguished [1]. An extinction is most likely to occur in flight during a glide or dive with the engine idling, when there is a high airflow and only a small fuel flow [1]. The range of air/fuel ratio between the rich and weak limits are reduced with an increase of air velocity. If the air mass flow is increased beyond a certain value, flame extinction occurs. The operating range defined by the stability loop must obviously cover the air/fuel ratios and mass flow of the combustion chamber [8]. The ignition process has weak and rich limits like those shown for stability in fig. 2.25.

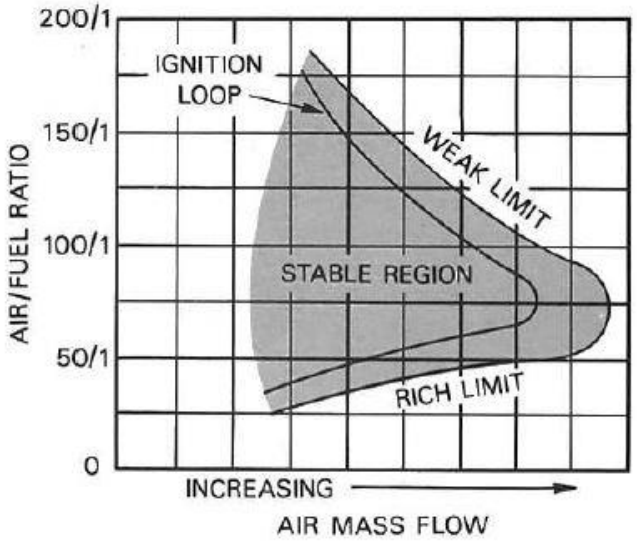

Figure 2.25 Combustion stability limits [44].

2.5 Combustion fundamentals

Combustion is perhaps described most simply as an exothermic reaction of a fuel and an oxidant. In gas turbine applications, the fuel may be gaseous or liquid, but the oxidant is always air [1]. Combustion occurs in many forms, not all of which are accompanied by flame or luminescence [1]. In this section will be given a general view about the combustion fundamentals.

2.5.1 Combustion flames

Types of flames

Most fundamental studies of flame combustion are performed using gaseous or prevaporized fuels. Furthermore, although a flame can propagate through a static gas mixture, it is usual to stabilize the flame at a fixed point and supply it with a continuous flow of combustible mixture. Under these conditions, flames can be classified in premixed and diffusion flames, depending

on whether the fuel and air are mixed before combustion, or mixed by diffusion in the flame zone [1]. Both types of flame can be further classified as laminar or turbulent, depending on the prevailing flow velocities [1].

In the systems burning liquid fuels, if the fuel is not completely vaporized before entering the flame zone, heterogeneous spray combustion may take place [1]. This process, involving diffusion flame burning of individual evaporating fuel droplets, may be superimposed on a premixed turbulent flame zone. However, if both reactants are in the same physical state, the combustion process is described as homogeneous [1].

Flammability limits

Not all fuel–air mixtures will burn or explode; flames can propagate through fuel–air mixtures only within certain limits of composition. If small amounts of combustible fuel gas or vapor are gradually added to air, a point will be reached at which the mixture just becomes flammable [1]. At this point, the percentage of fuel gas is called the *lower flammable limit, weak limit, or lean limit*. If more fuel is added, another point will eventually be reached at which the mixture will no longer burn [1]. At this point, the percentage of fuel gas is called the *upper flammable limit or rich limit*. For many fuels, the *weak limit* corresponds to an equivalence ratio of around 0.5, and the *rich limit* to an equivalence ratio of around 3 [1].

An increase in pressure above atmospheric usually widens the flammability limit of gases and vapours [1]. Even though the effect is usually less than that of pressure, the flammability range is also widened by an increase in temperature [1]. In the practically important range of pressures from 10 kPa to 5 MPa, the weak flammability limit is not strongly pressure dependent [1].

For liquid fuels, the formation of combustible mixtures is only possible within definite temperature limits. The lower temperature limit is taken as the minimum temperature at which the fuel's vapor pressure is enough to form the weak-limit volume concentration of vapor in air. And below this temperature, the mixture becomes too weak for flammability. The upper temperature limit corresponds to the rich-limit concentration, and a subsequent increase in temperature enriches the mixture to a condition of nonflammability [1].

The lowest temperature at which a flammable mixture can be formed above the liquid phase is called the flash point when quoted for atmospheric pressure. The ease with which enough vapor is formed to produce a flammable mixture depends on the vapor pressure of the fuel. Highly volatile fuels produce high vapor pressures that give low flash points [1].

2.5.2 Mixture ratios

The mixture ratio is an important parameter in a combustor system, because it affects the combustor´s performance, life span, efficiency and pollution characteristics. This parameter represents the ratio in which the fuel and air present in a system. In the premixed combustor system, there is only one mixture ratio throughout the entire combustion process. In the present non-premixed study case, there is an infinite range of ratios, that spreads from pure air to pure fuel. The mixture ratio can be defined through the FAR, the equivalent of ratio, through excess air and by the mixture fraction.

Fuel–air ratio (FAR) is commonly used in the gas turbine industry and refers to the ratio of fuel to the air at any given moment. Fuel–air ratio is the inverse of the AFR, and is expressed through Eq. 2.20:

$$FAR = \frac{m_f}{m_a} \tag{2.20}$$

In order to determine if a mixture is rich or lean, i.e., excess fuel or air respectively, an equivalence ratio (ϕ) is used, and is represented by Eq. 2.21:

$$\phi = \frac{FAR_{actual}}{FAR_{stoi}} = \frac{m_f/m_a}{(m_f/m_a)_s} \tag{2.21}$$

For all fuels, a value of ϕ < 1 indicates a lean mixture, whereas a value of ϕ > 1 indicates a rich mixture. The primary zone is typically rich, in order to promote reaction stability.

The mixture fraction (ξ) is a very useful variable in combustion modelling, in particular for diffusion flames, and is defined as the ratio by mass of mixture which originated from the fuel, as opposed to the oxidizer stream. This parameter is represented by Eq. 2.22:

$$\xi = \frac{m_f}{m_f + m_a} = \frac{m_f/m_f}{\frac{m_f}{m_f} + \frac{m_a}{m_f}} = \frac{1}{1 + AFR} \tag{2.22}$$

As we can verify with Eq. 2.22, in the air stream $\xi = 0$, and in the fuel stream $\xi = 1$.

2.5.3 Combustion Stoichiometry

Two components, the fuel and the oxidant, are required for combustion. In case of combustion of a hydrocarbon (C_xH_y) there is always formation of CO_2 and H_2O, and the complete stoichiometric reaction with oxygen is defined by Eq.2.23:

$$C_xH_y + \left(x + \frac{y}{4}\right) O_2 \rightarrow xCO_2 + \frac{y}{2} H_2O \tag{2.23}$$

There are two types of combustion, complete and incomplete reaction. The difference between these two types of combustion lies in the products of the reaction. In the complete combustion

is released CO_2, H_2O and energy and in the incomplete reaction is released CO_2, H_2O, intermediary products (CO, etc) and energy.

The air is composed in its majority of N_2 (76.8%), O_2 (23.2%), and small amounts of CO_2, argon and other traces of species. This means that for every mole of oxygen required for combustion, 3.78 mol of N_2 must be also introduced. N_2 does not alter significantly the O_2 balance, however it does have a major impact on the thermodynamics, chemical kinetics, and formation of pollutant in combustion systems [51]. This said, the complete stoichiometric relation for complete oxidation of a hydrocarbon fuel is represented in Eq. 2.24:

$$C_xH_y + \left(x + \frac{y}{4}\right)(O_2 + 3.76N_2) \rightarrow xCO_2 + \frac{y}{2}H_2O + 3.76\left(x + \frac{y}{4}\right)N_2 \quad (2.24)$$

Using the Eq. 2.24, the stoichiometric coefficients for each substance are calculated using Eq.2.25 – 2.28:

$$C: a_{CO_2} = x \quad (2.25)$$

$$H: 2a_{H_2O} = y \quad (2.26)$$

$$N_2: a_{n_2} = 3.76 * a_{O_2} \quad (2.27)$$

$$O_2: a_{O_2} = x + \frac{y}{4} \quad (2.28)$$

To calculate the number of moles of air to one mole of fuel, use the Eq. 2.29:

$$n_{air} = a_{O_2} * 4.76 = 4.76(x + \frac{y}{4}) \quad (2.29)$$

2.5.4 Adiabatic enthalpy, enthalpy of formation and enthalpy of combustion

The absolute enthalpy, also known as standardized enthalpy, is the sum of the enthalpy of formation (h_f) and the sensible enthalpy change (Δh_s). The enthalpy of formation considers the energy associated with the chemical bonds, while the sensible enthalpy change is associated only with the temperature [9]. Eq. 2.30 represents the absolute enthalpy at a temperature T:

$$\bar{h}_i(T) = \bar{h}^o_{f,i}(T_{ref}) + \Delta\bar{h}_{s,i}(T_{ref}) \quad (2.30)$$

, where $\bar{h}_{s,i} = \bar{h}_i(T) - \bar{h}^o_{f,i}(T_{ref})$.

The subscript *ref* presented in Eq. 2.30 refers to the standard reference state. Thus, the standard state temperature and pressure are $T_{ref} = 25^oC\ (298.15K)$ and $P_{ref} = P^o = 1\ atm\ (101{,}325Pa)$, respectively, which are consistent with Chemkin and NASA thermodynamic databases [52]. For the elements that are in their natural state, the enthalpy of formation is conventionally adopted as zero, and for enthalpy of formation other than the reference state, these are tabulated in many literatures.

The enthalpy of combustion (or enthalpy of reaction (Δh_R)) per mass of mixture (intensive properties), is given by Eq. 2.31, or in terms of extensive properties, which is given by Eq. 2.32:

$$\Delta H_R = h_{prod} - h_{reac} \tag{2.31}$$

$$\Delta H_R = H_{prod} - H_{reac} \tag{2.32}$$

2.5.5 Heat of combustion

The heat of combustion (Δh_c) is the energy released as heat when a compound undergoes complete combustion with oxygen and is symmetric to the enthalpy of reaction. There are two heating values; the Higher Heating Value (HHV), which is the heat of combustion calculated, with assumption that all the water in the products has condensed to the liquid sate, and the other heat value is called the Lower Heating Value (LHV) [9]. The calculation of the LHV, assumes that none of the water is condensed [9]. The standard state of the heating values for a variety of hydrocarbons are present in few literatures. These two heating values can be related by Eq.2.33:

$$HHV = LHV + h_v \times (n_{H_2O,out}/n_{fuel,in}) \tag{2.33}$$

2.5.6 Adiabatic flame temperature

For a combustion process that takes place adiabatically with no shaft work, the temperature of the products is referred to as the adiabatic flame temperature. This is the maximum temperature that can be achieved for given reactants. The maximum adiabatic flame temperature for a given fuel and oxidizer combination occurs with a stoichiometric mixture. The amount of excess air can be tailored as part of the design to control the adiabatic flame temperature [53].

In combustion studies, two types of adiabatic flame temperature can be used, depending on how the process is completed. These are constant volume and constant pressure. However, only the combustion at constant-pressure is relevant for this work, as GCT´s operate at constant pressure [9], and in this case the absolute enthalpy of the reactants at T_{ref} is equal to the absolute enthalpy at the final state ($T = T_{ad}\,, P = 1\ atm$).

The first law, represented by Eq. 2.35, is what defines this constant pressure adiabatic flame temperature (Eq. 2.34).

$$q_{cv} - w_{cv} = h_0 - h_i + \frac{1}{2}(v_0^2 - v_i^2) + g(z_0 - z_i) \tag{2.34}$$

$$h_{reac}(T_i, P) = h_{prod}(T_{ad}, P) \tag{2.35}$$

Another parameter of interest is the heat capacity (C). The heat capacity is defined as the ratio of heat added (or removed from an object), to the resulting temperature difference, as shown in Eq. 2.36:

$$C = \frac{Q}{\Delta T} \tag{2.36}$$

More heat is required from the system to achieve the same temperature change for an ideal gas at constant pressure, than it is required at constant volume. This is because at constant volume, all heat added is used to raise the temperature. The specific heat capacity at constant pressure (c_p) is represented by Eq. 2.37:

$$c_p = (\frac{\partial h}{\partial T})_p \tag{2.37}$$

The enthalpy rise requirement of a GTC is set by the cycle pressure ratio, by the properties of the working fluid and fuel, and by the material limitations [54], and all these factors are balanced in Eq. 2.38:

$$\frac{\dot{m}_f}{\dot{m}_a} = \frac{c_p}{Q_f}(T_3 - T_2) \tag{2.38}$$

2.6 Emissions

2.6.1 ICAO LTO cycle

The study in this work will consider the standards required for emission control, as well as the landing and take-off (LTO) cycles.

The International Civil Aviation Organization (ICAO) has promulgated regulations for civil subsonic turbojet/turbofan engines with rated thrust levels above 26.7 kN (6000 pounds) for a defined landing-take-off cycle (LTO), which is based on an operational cycle around airports [1]. LTO cycle refers to all the operations the aircraft carry out below 3000 ft (914.4 m) above field elevation over a specific range of certifiable operating conditions and includes four stages in terms of both engine power settings and typical time in each specific mode of operation (time-in-mode, TIM).

The ICAO LTO cycle is divided in four stages, as illustrated in figure 2.26. These stages are the following [9]:

1. Take-off: Average thrust setting from take-off release, to the point of main throttle back.
2. Climb: Thrust setting from the point of throttle back to the ICAO LTO cycle maximum altitude of 3000 ft [9].

3. Approach: Average thrust setting from the ICAO LTO cycle maximum altitude of 3000ft, over the touch down point at the end of the roll-out on the runway [9].
4. Taxi/Ground idle: This phase extends to the beginning of the take-off phase and the end of the approach phase [9].

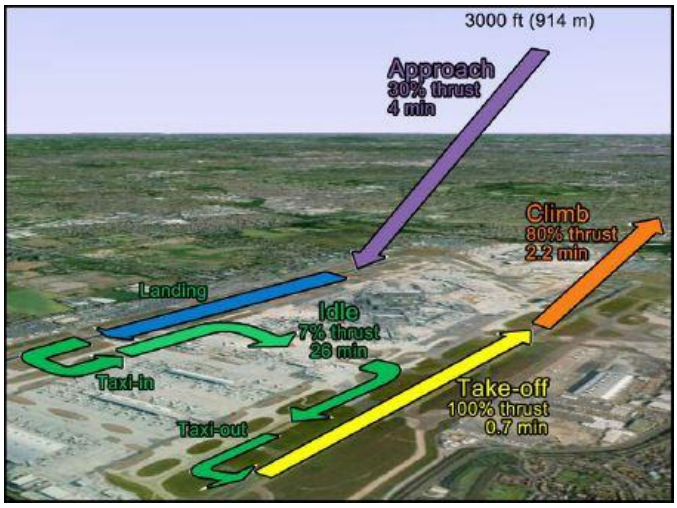

Figure 2.26 Standard ICAO LTO cycle. Adapted from [55].

Table 2.6 LTO cycle measurements for the CFM56-3 [56].

Mode	Power setting ($\%F_{00}$)	Time ($mins.$)	Fuel flow ($\frac{kg}{s}$)	EI ($\frac{g}{kg}$)			SN
				UHC	CO	NO_x	
Take-off	100	0.7	0.946	0.04	0.9	17.7	4
Climb out	85	2.2	0.792	0.05	0.95	15.5	2.5
Approach	30	4.0	0.290	0.08	3.8	8.3	2.5
Idle	7	26.0	0.114	2.28	34.4	3.9	2.2

Table 2.6 shows the typical power settings, as well as the time spent in each phase for ICAO´s LTO cycle.

The emissions during standardised LTO cycles are then reported as emission index (EIs) expressed as mass of pollutant emitted per unit mass of fuel burned. Fuel-based emission indices for the compound X are calculated according to Eq.2.39:

$$EI(X) = F_c * \left(\frac{M_X}{M_{CO_2}}\right) * \left(\frac{\Delta X}{\Delta CO_2}\right) \quad (2.39)$$

In Eq.2.39, F_c represents the CO_2 produced per kilogram of fuel consumed assuming complete combustion and given a particular hydrogen to carbon ratio. M_X and M_{CO_2} are the molecular weights of the compound X and CO_2, respectively, also ΔX and ΔCO_2 are the enhancements of

compound X and CO_2 within the plume, respectively. The EI_{NO_x} for an annular combustor is expressed by Eq 2.40:

$$\mathrm{EI} = 32 \times \mathrm{S_{NO_x}} \tag{2.40}$$

In Eq.2.40, S_{NO_x} defines the NO_x Severity Parameter, which is expressed in Eq.2.41:

$$\mathrm{S_{NO_x}} = \left(\frac{\mathrm{P_3}}{2965\mathrm{kPa}}\right)^{0.4} \times \mathrm{e}\left(\frac{\mathrm{T_3}-826\mathrm{K}}{194\mathrm{K}} + \frac{6.29-100*\mathrm{war}}{53.2}\right) \tag{2.41}$$

The emissions can be calculated by Eq. 2.42 and then compared with ICAO´s results for the CFM56-3 (see table 2.7).

$$Emission\ [g/kN] = EI\ [g/kg\ fuel] \times SFC\ [kg\ fuel/hr\ kN] \times Time\ in\ mode\ [hr] \tag{2.42}$$

Table 2.7 ICAO Gaseous Emissions Standards [1].

Emission $(\frac{g}{kN})$	Subsonic Turbojet/Turbofan Engines[13]	Supersonic Turbojet/Turbofan Engines
HC	19.6	$140(0.92)^{\pi_{00}}$
CO	118.0	$4550(\pi)_{00}^{-1.03}$
$\boldsymbol{NO_x}$	$32 + 1.6\pi_{00}$ $-1.04 + 2\pi_{00}(2007 + engines)$	$36 + 2.4\pi_{00}$

Eq. 2.42 shows that two methods are available to the engine manufacturer for reducing NO_x [1]. One is to make improvements to the combustor that reduce its emissions index (*EI*), and the other is to choose an engine cycle that yields a lower SFC. Since the CO and *UHC* levels of modern engines have been significantly reduced at all low-power conditions, and only NO_x is emitted in appreciable amounts at altitude cruise, in practice the emissions generated by aircraft engines consist primarily of NO_x [1].

Furthermore, if the data regarding the fuel flow was not available, it can be calculated by knowing the power output of the engine at take-off condition, which is 40 kW, and the LHV of the fuel, which in this case is kerosene and have the value of 43.1 MJ/kg, by Eq.2.43:

$$\dot{m}_{fuel} = \frac{P[kW]}{LHV_{fuel}[\frac{MJ}{kg}]} = \frac{40}{43.15} \approx 0.93[\frac{kg_{fuel}}{s}] \tag{2.43}$$

The ICAO standard for smoke measurement is expressed in terms of a smoke number (SN), which is related to the engine take-off thrust (F_{00}) by Eq. 2.44:

[13] Newly manufactured engines with rated take-off thrust greater than 26.7 kN [1].

$$SN = 83.6(F_{00})^{-0.274} \tag{2.44}$$

This expression is shown graphically in figure 2.27 and has the intention of eliminate any visible smoke from the engine exhaust. As smoke visibility depends on both the smoke concentration, as indicated by the value of SN, and on the viewing path length, the allowable SN of a high thrust engine is lower than for a low thrust engine because of its larger exhaust diameter [1].

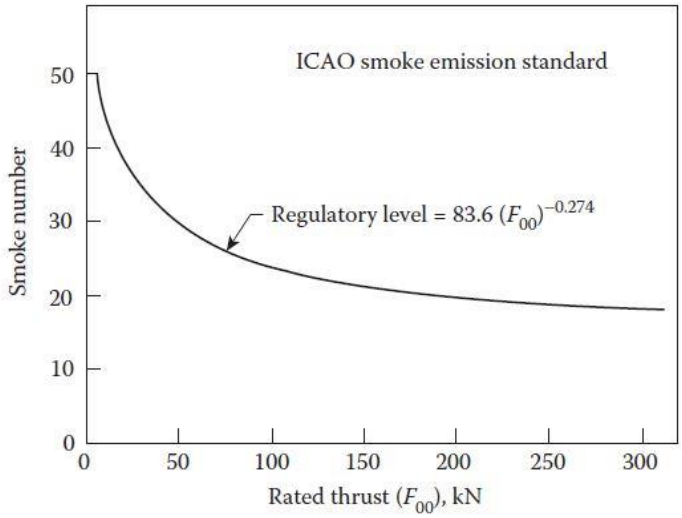

Figure 2.27 ICAO smoke emissions standards [1].

2.6.2 Mechanisms of Pollutant Formation

The concentration levels of pollutants in gas turbine exhausts can be related directly to the temperature, time, and concentration histories of the combustion process [1]. These vary from one combustor to another and, for any given combustor, with changes in operating conditions [1]. The nature of pollutant formation is such that the concentrations of CO and UHC are highest at low power conditions and diminish with an increase in power. By contrast, NO_x and smoke which are negligible at low-power settings and attain maximum values at the highest power condition [1]. These characteristic trends are shown in figure 2.28.

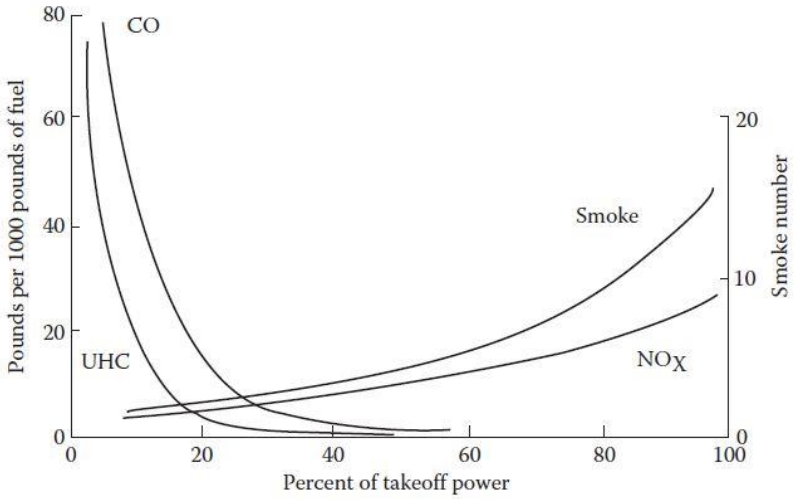

Figure 2.28 Emissions characteristics of gas turbine engines [1].

2.6.2.1 Carbon Monoxide

The mechanism of CO oxidation is slowly growing compared to the oxidation reactions of the hydrocarbons. In the absence of an atmosphere without radicals *H*, the main reactions involved in the oxidation are represented by Eq.2.45 and 2.46:

$$CO + O + M \rightarrow CO_2 + M \tag{2.45}$$

$$CO + O_2 \rightarrow CO_2 + O \tag{2.46}$$

Due to the presence of hydrogen and / or water (i.e. an atmosphere with radical H), OH radicals form during combustion and lead to oxidation of CO according to the reaction represented by Eq.2.47:

$$CO + OH \rightarrow CO_2 + H \tag{2.47}$$

Eq. 2.47 is considered the dominant reaction in the CO oxidation process and is dependent on the chemical equilibrium of CO, OH, H radicals during the combustion process. Eq. 2.45 and Eq.2.46 present lower weight at elevated temperatures [57]. The main reactions involved in the chemical equilibrium between these radicals and the molecules O_2, H_2O and H_2 are represented by Eq.2.48-2.51:

$$H + O_2 \rightleftharpoons OH + O \tag{2.48}$$

$$O + O_2 \rightleftharpoons H + OH \tag{2.49}$$

$$H_2 + OH \rightleftharpoons H + H_2O \tag{2.50}$$

$$H + O_2 + M \rightleftharpoons HO_2 + M \tag{2.51}$$

In addition to the reactions reported in the oxidation of CO, the following reaction represented by Eq. 2.52 also presents a route for the oxidation of CO [57].

$$CO + HO_2 \rightarrow CO_2 + OH \tag{2.52}$$

2.6.2.2 Unburned Hydrocarbons

The unburned hydrocarbons include fuel that emerges from the combustor in the form of drops or vapor, as well as the products of the thermal degradation of the parent fuel into species of lower molecular weight [1]. The UHC are normally associated with poor atomization, inadequate burning rates, the chilling effects of film- cooling air, or any combination of these. The reaction kinetics of unburned hydrocarbons formation are more complex than for carbon monoxide formation. However, it is generally found that those factors that influence CO emissions also influence UHC emissions and in much the same manner [1].

2.6.2.3 Smoke

Exhaust smoke is caused by the production of finely divided soot particles in fuel-rich regions of the flame that, in conventional combustors, are always close to the fuel spray [1]. These are the regions in which recirculating burned products move upstream toward the fuel injector, and local pockets of fuel vapor become enveloped in oxygen-deficient gases at high temperature [1]. In these fuel-rich zones, soot may be produced in considerable quantities [1].

Most of the soot produced in the primary zone is consumed in the high temperature regions downstream [1]. Thus, from a smoke viewpoint, a combustor may be considered to comprise two separate zones—the primary zone, which governs the rate of soot formation, and the intermediate zone (and, on modern high-temperature engines, the dilution zone also), which determines the rate of soot consumption [1]. The soot concentration observed in the exhaust gas is the difference between two large numbers [1].

Analysis of the soot found in exhaust gases consists mostly of carbon (96%) and a mixture of hydrogen, oxygen, and other elements [1]. CFD modelling of soot formation and oxidation within the combustion system in study is difficult because of the complexity of the physical and chemical processes involved, and because of the typical dimensions of the computational grids used for complex geometries [58]. Thus, soot modelling remains one of the greatest challenges to computational modelling of combustion products, and as it isn't a priority for this work, it will not be considered [9].

2.6.2.4 Oxides of Nitrogen

Most of the nitric oxide (NO) formed in combustion subsequently oxidizes to NO_2 [1]. For this reason, it is customary to lump NO and NO_2 together and express results in terms of NO_x, rather than NO [1]. It can be produced by two different mechanisms: thermal NO_x and prompt NO_x.

NO_x is also produced through the fuel-bond, but this is usually of less importance for normal fuels [58].

Thermal Nitric Oxide

This is produced by the oxidation of atmospheric nitrogen in high-temperature regions of the flame and in the post flame gases [1]. The process is endothermic, and it proceeds at a significant rate only at temperatures above around 1850K [1]. Most of the proposed reaction schemes for thermal NO utilize the extended Zeldovich mechanism, as represented in Eq. 2.53-2.56:

$$O_2 \leftrightharpoons 2O \tag{2.53}$$

$$N_2 + O \leftrightharpoons NO + N \tag{2.54}$$

$$N + O_2 \leftrightharpoons NO + O \tag{2.55}$$

$$N + OH \leftrightharpoons NO + H \tag{2.56}$$

The rate at which NO_x can be produced by Zeldovich reaction, can be estimated through the equilibrium concentration of O_2 in the post-flame zone, through Eq. 2.57:

$$\frac{d[NO]}{dt} = 6 \times 10^{16} T_{eq}^{-0.5} \exp\left(\frac{-69.090}{T_{eq}}\right) [O_2]_{eq}^{0.5} [N_2]_{eq} \quad [\frac{moles}{cm^3 sec}] \tag{2.57}$$

Prompt Nitric Oxide

It is known that during combustion of hydrocarbon fuels, the NO_x formation rate can exceed that produced from direct oxidation of nitrogen molecules (i.e., thermal NO_x) [59].

The presence of a second mechanism leading to NO_x formation was first identified by Fenimore [60] and was termed "prompt NO_x ". There is good evidence that prompt NO_x can be formed in a significant quantity in some combustion environments, such as in low-temperature, fuel-rich conditions and where residence times are short. Surface burners, staged combustion systems, and gas turbines can create such conditions [59]. At present, the prompt NO_x contribution to total NO_x from stationary combustors is small. However, as NO_x emissions are reduced to very low levels by employing new strategies (burner design or furnace geometry modification), the relative importance of the prompt NO_x can be expected to increase [59].

Prompt NO_x is most prevalent in rich flames. The actual formation involves a complex series of reactions and many possible intermediate species, as represented in Eq. 2.58-2.61:

$$CH + N_2 \rightleftharpoons HCN + N \tag{2.58}$$

$$N + O_2 \rightleftharpoons NO + O \quad (2.59)$$

$$HCN + OH \rightleftharpoons CN + H_2O \quad (2.60)$$

$$CN + O_2 \rightleftharpoons NO + CO \quad (2.61)$$

Several species resulting from fuel fragmentation have been suggested as the source of prompt NO_x in hydrocarbon flames (e.g., CH, CH_2,C, C_2H), but the major contribution is from CH (Equation 2.58) and CH, as shown in Eq.2.62:

$$CH_2 + N_2 \leftrightharpoons HCN + NH \quad (2.62)$$

The products of these reactions could lead to formation of amines and cyano compounds that subsequently react to form NO by reactions like those occurring in oxidation of fuel nitrogen, as shown in Eq.2.63:

$$HCN + N \rightleftharpoons N_2 + \cdots \quad (2.63)$$

2.6.3 Pollutants Reduction in Conventional Combustors

In the section 2.6.2, the attention was focused on the various mechanisms and processes involved in the formation of pollutant emissions and its regulation. Of equal interest and importance is the application of this knowledge to the problems of reduce pollutant emissions in practical combustion systems.

The main factors controlling emissions from conventional combustors may be considered in terms of primary-zone temperature and equivalence ratio, degree of homogeneity of the primary-zone combustion process, residence time in the primary zone, liner-wall quenching characteristics and fuel spray characteristics [1].

Carbon Monoxide and Unburned Hydrocarbons

The presence of these species in the exhaust gases is a manifestation of incomplete combustion [1]. Thus, all approaches to *CO* and UHC reduction are based on a common philosophy, which is to raise the level of combustion efficiency [1].

An effective method of achieving this is by redistributing of the airflow to bring the primary zone equivalence ratio closer to the optimum value of around 0.8 [1]. A higher equivalence ratio (up to around 1.05) would increase burning rates even further, but it would not yield lower emissions of *CO* and UHC because of lack of the oxygen that these species need in order to convert to CO_2 and H_2O [1]. Good fuel–air mixing in the primary zone is also essential for low *CO* and UHC [1]. Even when operating at the optimum equivalence ratio, poor mixing can produce local regions in which the mixture strength is either too fuel-lean to provide adequate

burning rates or so fuel-rich that there is insufficient O_2 to convert all the *CO* produced into CO_2 [1].

Another effective means of reducing *CO* and UHC is by using less liner wall-cooling air, especially in the primary zone [1].

Smoke

The factors governing smoke emissions are combustor inlet air temperature, pressure, and fuel spray characteristics [1]. The influence of inlet air temperature is complex because an increase in this parameter serves to accelerate both the soot-forming and the soot-burnout processes; the net result is usually a reduction in smoke [1].

The elimination of exhaust smoke is basically a matter of preventing the occurrence of fuel-rich pockets in the flame [1]. Injecting more air into the primary zone is always beneficial, especially if accompanied by more thorough mixing [1]. Unfortunately, this approach is somewhat limited in scope, owing to the adverse effect of an increase in primary-zone air on ignition and stability limits and on *CO* and UHC emissions at idle [1].

The design of the fuel injector and, in particular, the degree of premixing of fuel and air before combustion, have a very large influence on whether a given combustor will produce significant amounts of smoke [1].

Oxides of Nitrogen

In any attempt to reduce NO_x, the prime goal must be to lower the reaction temperature [1]. The second objective should be to eliminate hot spots from the reaction zone, as there is little point in achieving a satisfactorily low average temperature if the reaction zone contains local regions of high temperature in which the rate of NO_x formation remains high [1]. Finally, the time available for the formation of NO_x should be kept to a minimum [1].

Practical approaches to low NO_x in conventional combustors include the addition of more air into the primary combustion zone to lower the flame temperature, improved atomization increase in liner pressure drop to promote better mixing, thereby eliminating hot spots from the combustion zone, and reduction in combustor residence time [1]. Unfortunately, reductions in flame temperature and residence time lead to increased output of both *CO* and UHC [1]. In fact, as a generalization, it can be stated that any change in operating conditions or combustor configuration that reduces NO_x tends also to exacerbate the problems of *CO* and UHC, and vice versa [1].

2.7 Jet Fuel

In chapter 1 was presented the historic review of the fuels. Thus, the major aviation jet fuels were presented. Here this presents the physical and chemical properties of conventional jet fuels.

2.7.1 Types of Hydrocarbons

Conventional jet fuels consist of mixtures of hundreds of different hydrocarbons. It is common to classify the hydrocarbons present in jet fuel into four main groups: paraffinic, olefinic, naphthenic, and aromatic [15].

2.7.1.1 Paraffins

Paraffins are a hydrocarbon compound of C-atoms connected in a chain. The general chemical formula is formula C_nH_{2n+2} [15]. Here the *n* is the number of C-atoms, i.e. the carbon number, of the hydrocarbon [15]. The simplest hydrocarbon, methane, is in this class and it is represented in figure 2.29.

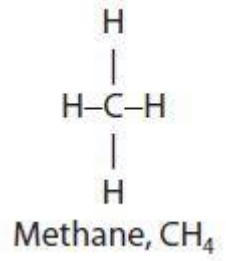

Figure 2.29 Example of the chemical structure of methane [1].

Alternative paraffin configurations, or *isoparaffins*, are in the form of branched chains, as represented in figure 2.30.

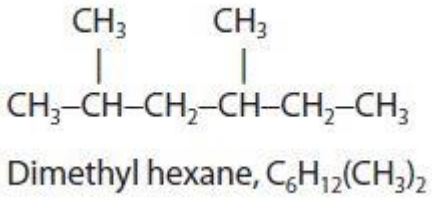

Figure 2.30 Example of the chemical structure of isoparaffins [1].

Current aviation fuels contain an average of 60% paraffins, depending on the source of the crude oil and the distillation process [1]. Compared to other hydrocarbon fuels, paraffins have the properties of higher gravimetric heat of combustion, lower density and freeze point, and a higher hydrogen-to-carbon ratio [15]. They also have high thermal stability, and combustion of paraffins is absent of exhaust smoke and deposition of coke [15].

2.7.1.2 Olefins

Olefins conform to the general formula C_nH_{2n}. As olefins are unsaturated, i.e., their molecules contain less than the maximum possible number of hydrogen atoms, they are very active chemically and readily react with a great many compounds to form resinous gums and rubber like materials [1]. For this reason, olefins are very undesirable in gas turbine fuels, and are found only in trace quantities [1].

Olefin molecules must contain at least two carbon molecules, and the lightest molecule is, therefore, C_2H_4, ethylene. More complex molecules of the olefin series are obtained by adding CH_2 [1].

Examples of more complex molecules of the olefins are illustrated in figure 2.31.

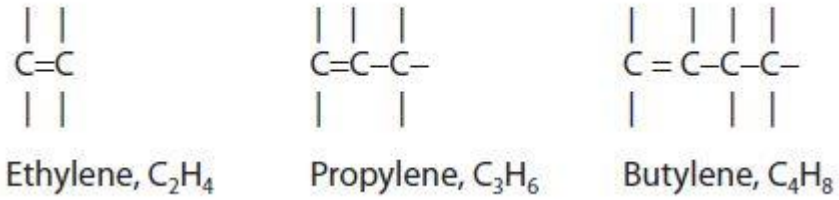

Figure 2.31 An example of the chemical structure of olefins [1].

2.7.1.3 Naphthenes

Naphthenes, are saturated hydrocarbons in which the carbon atoms are linked to form rings, as opposed to the chains of the paraffins. Single ring naphthenes have the chemical formula $(CH_2)_n$ [15]. Naphthenes has names identical to those of the paraffins that have the same number of carbon atoms, with the addition of the prefix “cyclo”. Figure 2.32 shows some examples of chemical structure of naphthenes.

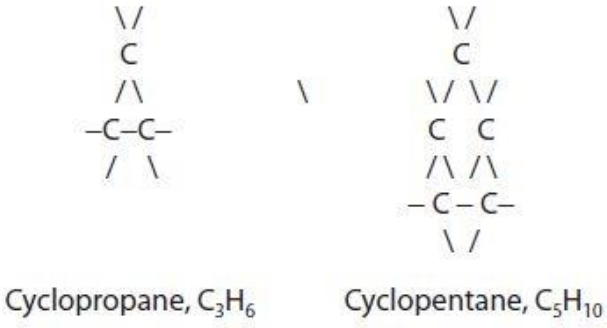

Figure 2.32 An example of the chemical structure of naphthenes [1].

Naphthenes are major constituents of jet fuel, i.e., about 25–35% [1]. As with paraffins, naphthenes have a good thermal stability, low tendency to form soot, and a high gravimetric heat of combustion [15]. They also aid in reducing the freezing point of the fuel, which is suitable in the high-altitude flights [61].

2.7.1.4 Aromatics

Aromatics are unsaturated compounds consisting of one or more 6 C-atoms as naphthenes, but with 3 double bonds distributed between every second C-atom. Although similar in structure to the naphthenes, they contain less hydrogen and, in consequence, their specific energy is appreciably lower. Aromatic compounds in fuel cause swelling of o-ring and this helps seal the high-pressure aircraft fuel system.

The chemical formula for monocyclic (which means they consist of only one carbon ring) aromatics is C_nH_{2n-6} [15]. The simplest member is benzene, in which each carbon atom carries only one hydrogen atom [1]. An illustration of the simplest aromatic, benzene, and the more complex, toluene [15] are shown in figure 2.33.

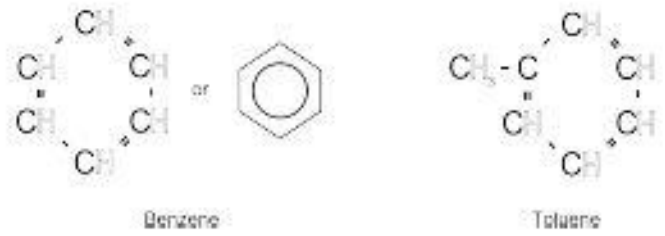

Figure 2.33 An example of the chemical structure of monocyclic aromatics [15].

More complex molecules of the aromatic group are obtained either by replacing one or more of the hydrogen atoms with hydrocarbon groups or by "condensing" one or more rings [1].

2.7.2 Fuel Properties

In a combustion chamber, the fuel must be injected, vaporized, and mixed with air before combustion can occur [1]. The extent to which these processes are limiting to combustion depends, to a very great extent, on the physical properties of the fuel [1].

2.7.2.1 Relative Density

The relative density d_r (formerly called specific density) of a fuel is related to its average boiling point and chemical composition. In general, it is highest for aromatics and lowest for paraffins, with naphathenes and olefins lying in between [1]. The relative density is easy to determine, and it provides a useful indication of hydrogen/carbon ratio, calorific value, and tendency toward carbon formation [1].

2.7.2.2 Distillation Range

The distillation range of a fuel is important because it largely determines the physical and combustion characteristics of the fuel and has a dominating influence on availability [1]. Availability is increased by widening the boiling range, either by lowering the initial boiling point, or both [1].

2.7.2.3 Vapor Pressure

The vapor pressure of a liquid is the pressure exerted by the vapor above its surface at a given temperature [1]. A high vapor pressure ensures rapid evaporation of fuel in the primary combustion zone [1].

On the other hand, low vapor pressure has advantages in terms of reduced pressure in unvented fuel tanks, lower fuel losses due to evaporation at high altitudes in vented tanks, and reduced fire hazard [1].

2.7.2.4 Flash Point

The flash point is defined as the lowest temperature at which a fuel gives off enough vapor to form a flammable mixture with air [1]. The flash point is directly related to vapor pressure; the higher the vapor pressure, the lower the flash point. In general, the flash point of kerosene provides a measure of its flammability, whereas that of heavier oils is an indication of their volatility. It is also useful for classifying fuels from the viewpoint of fire risk [1].

2.7.2.5 Volatility Point

The volatility of a fuel may be assessed from a knowledge of its distillation range, vapor pressure, and flash point. Increased volatility affects combustion performance by providing easier lightup, improved stability, and higher combustion efficiency [1].

2.7.2.6 Viscosity

Viscosity is a physical property that depends mainly on the chemical composition of the hydrocarbons contained in the fuel [62]. Viscosity has marked effect on the formation of a well-atomized spray and hence on the rates of fuel evaporation and combustion and affects the power required to pump the fuel through the fuel system [1].

2.7.2.7 Surface Tension

Usually there are no specification limits on surface tension for gas turbine fuels, but this property has a significant effect on fuel atomization, since, for both pressure and air blast atomizers $SMD \propto \sigma_F^{0.6}$ [1].

2.7.2.8 Freezing Point

The freezing point of the jet fuel is defined as the temperature at which the last wax crystals melt when warming the solidified fuel [1].

2.7.2.9 Specific Heat

The specific heat is an important property of the fuels burned in these aircraft. Paraffinic fuels are the most attractive in this regard because they have considerably higher specific heats than either naphthenic or aromatic fuels [1].

2.7.2.10 Latent Heat

The latent heat of evaporation at the average boiling point of the fuel may be related to relative density (d_r) and fuel temperature (T_f) by [1] Eq. 2.64:

$$L = \frac{360 - 0.39T_f}{d_r} (\ kJ/kg) \tag{2.64}$$

2.7.2.11 Thermal Conductivity

The thermal conductivity of a liquid petroleum fuel is given by [1] Eq. 2.65:

$$k = \frac{0.134 - 0.000063T_f}{d_r} (W/(m \cdot K) \tag{2.65}$$

Chapter 3

Numerical Modeling and Planning

Computational Fluid Dynamics (CFD) simulation provides a virtual laboratory to perform experiments in the early stages of design without building the physical apparatus [63]. Using the CFD simulation decrease the unit design costs as the number of unsatisfactory experimental devices also decrease. Simulations can be done by CFD modelling using commercial or own software with the same base. In this work, the CFD software used was ANSYS.

ANSYS is a software suit that spans the entire range of physics, providing access to lots of fields of engineering simulation that a design process requires. In particular, the module Fluent is appropriate for this work. Fluent's models are focused on fluids flow and chemical reactions, including a very good model to run a first-approach simulations of combustion systems [63].

The procedures for performing a simulation in ANSYS Fluent are the following [63]:

1. Design the geometry of the system.
2. Generate an appropriated mesh.
3. The physical modelling is defined. It is defined, for example, the equations of fluid motion, enthalpy, and species conservation.
4. Boundary conditions are defined, i.e. specifying the fluid behaviour and properties at all bounding surfaces of the fluid domain [63].
5. Analysis and visualization of the resulting solution.

3.1. Turbulence

Turbulent flows are characterized by fluctuating velocity fields. These fluctuations mix transported quantities such as momentum, energy, and species concentration, and cause the transported quantities to fluctuate as well [59]. For turbulent flows, the range of length scales and complexity of phenomena involved in turbulence make this process computationally expensive to simulate directly in practical engineering calculations. Instead, the exact governing equations can be time-averaged, ensemble-averaged, or otherwise manipulated to remove the resolution of small scales, resulting in a modified set of equations that are computationally less expensive to solve [59]. One of the best methods to analyse turbulent flows is to write the equations that represent conservation of mass, momentum, and species. A fluid can be defined as a substance that continually deforms, i.e., it flows under the action of a minor tangential force. The movement of these fluids is described by nonlinear differential equations known as Navier-Stokes equations.

3.1.1 Turbulence models

It is possible, in theory, to directly resolve the whole spectrum of turbulent scales using an approach known as direct numerical simulation (DNS) [59], in which the Navier- Stokes equations are numerically solved without need to use turbulence models. However, it is not feasible for practical engineering problems involving high Reynolds number flows [59]. For high Reynolds number flows, the cost becomes prohibitive.

There are, however, two other numerical simulation methods, not DNS, the Large Eddy Simulation (LES) and the Reynolds Average Navier-Stokes (RANS).

In the Reynolds Average Navier-Stokes (RANS) method the flow properties are decomposed into an average value and turbulence-related fluctuation. This method does not require the use of three-dimensional Navier-Stokes equations, it can be analysed axi-symmetrically, and thus does not need such thin meshes and consequently has less computational cost.

The Reynolds Averaged Navier-Stokes (RANS) equations are the following:

- Continuity:

$$\frac{\partial \bar{p}}{\partial t} + \frac{\partial}{\partial x_i}(\bar{p}\tilde{u}_i) = 0 \tag{3.1}$$

- Momentum:

$$\frac{\partial}{\partial t}(\bar{p}\tilde{u}_i) + \frac{\partial}{\partial x_j}(\bar{p}\tilde{u}_i\tilde{u}_j) - \frac{\partial}{\partial x_j}(\overline{pu_i''u_j''}) - \frac{\partial}{\partial x_j}\left[\mu\left(\frac{\partial \tilde{u}_i}{\partial x_j} + \frac{\partial \tilde{u}_j}{x_i} - \frac{2}{3}\partial_{ij}\frac{\partial \tilde{u}_i}{\partial x_i}\right)\right] = -\frac{\partial \bar{p}}{\partial x_i} \tag{3.2}$$

- Scalar transport:

$$\frac{\partial}{\partial t}(\bar{p}\widetilde{Y}_\alpha) + \frac{\partial}{\partial x_i}(\bar{p}\tilde{u}_i\widetilde{Y}_\alpha) + \frac{\partial}{\partial x_i}(\overline{pu_i''Y_\alpha''}) - \frac{\partial}{\partial x_i}(\Gamma_\alpha\frac{\partial \widetilde{Y}_\alpha}{\partial x_i}) = \widetilde{\omega}_\alpha \tag{3.3}$$

In laminar flow, the fluid stress is proportional to the rate of strain with the viscosity being a constant of proportionality [9]. In turbulent flow, the turbulent stress is related to the mean rate of strain through turbulent viscosity (μ_T). This is the so called Boussinesq's hypothesis, and is represented in Eq. 3.4:

$$-\overline{\rho u_i'' u_j''} = \mu_T\left(\frac{\partial \tilde{u}_i}{\partial x_j} + \frac{\partial \tilde{u}_j}{\partial x_i}\right) - \frac{2}{3}\bar{\rho}k\partial_{ij} - \frac{2}{3}\mu_T\frac{\partial \tilde{u}_k}{\partial x_k}\partial_{ij} \tag{3.4}$$

The turbulent viscosity is calculated from the kinetic energy of turbulence (k) and from the dissipation rate (ε) [9]; these are related through Eq. 3.5:

$$\mu_T = \bar{\rho}C_\mu\frac{k^2}{\varepsilon} \tag{3.5}$$

The transport equations for k and ε are used, and the scalar flux is set proportional to the mean scalar gradient [9], as shown in Eq. 3.6:

$$-\overline{\rho u_i'' \phi''} = \left(\frac{\mu}{\sigma} + \frac{\mu_T}{\sigma_T}\right)\frac{\partial \tilde{\Phi}}{\partial x_i} \tag{3.6}$$

For this study will be used ANSYS Fluent, and this software provides the following options of turbulence models:

1. Spalart-Allmaras model

The Spalart-Allmaras model is a relatively simple one-equation model that solves a modelled transport equation for the kinematic eddy viscosity [59] . This model was designed specifically for aerospace applications involving wall-bounded flows and has been shown to give good results for boundary layers subjected to adverse pressure gradients. It is also gaining popularity in the turbomachinery applications [59].

2. Standard, RNG, and Realizable $k-\varepsilon$ model

2.1 Standard $k-\varepsilon$ model

The simplest "complete models" of turbulence are the two-equation models in which the solution of two separate transport equations allows the turbulent velocity and length scales to be independently determined [59]. Robustness, economy, and reasonable accuracy for a wide range of turbulent flows explain its popularity in industrial flow and heat transfer simulations. It is a semi-empirical model, and the derivation of the model equations relies on phenomenological considerations and empiricism [59]. As the strengths and weaknesses of this model have become known, improvements have been made to the model to improve its performance. Two of these variants are available in ANSYS Fluent: the RNG $k-\varepsilon$ model and the realizable $k-\varepsilon$ model [59].

The standard $k-\varepsilon$ model is a semi-empirical model based on model transport equations for the turbulence kinetic energy (k) and its dissipation rate (ε). The model transport equation for k is derived from the exact equation, while the model transport equation for ε was obtained using physical reasoning and bears little resemblance to its mathematically exact counterpart [59].

2.2 RNG $k-\varepsilon$ model

It is similar in form to the standard $k-\varepsilon$ model, but includes the following refinements [59]:

1. The RNG model has an additional term in its ϵ equation that improves the accuracy for rapidly strained flows.

2. The effect of swirl on turbulence is included in the RNG model, enhancing accuracy for swirling flows.
3. The RNG theory provides an analytical formula for turbulent Prandtl numbers, while the standard $k-\varepsilon$ model uses user-specified, constant values.
4. While the standard $k-\varepsilon$ is a high-Reynolds-number model, the RNG theory provides an analytically derived differential formula for effective viscosity that accounts for low-Reynolds-number effects.

These features make the RNG $k-\varepsilon$ model more accurate and reliable for a wider class of flows than the standard $k-\varepsilon$ model [59].

The RNG-based $k-\varepsilon$ turbulence model is derived from the instantaneous Navier-Stokes equations, using a mathematical technique called "renormalization group" (RNG) methods [59]. The analytical derivation results in a model with constants different from those in the standard $k-\varepsilon$ model, and additional terms and functions in the transport equations for k and ε [59].

2.3 Realizable $k-\varepsilon$ model

The realizable $k-\varepsilon$ model [65] is a relatively recent development and differs from the standard $k-\varepsilon$ model in two important ways [59]:

1. This model contains a new formulation for the turbulent viscosity.
2. A new transport equation for the dissipation rate, ϵ, has been derived from an exact equation for the transport of the mean-square vorticity fluctuation [59].

The term "realizable" means that satisfies certain mathematical constraints on the Reynolds stresses, consistent with the physics of turbulent flows [59]. Neither the standard $k-\varepsilon$ model nor the RGN $k-\varepsilon$ model is realizable [59].

3 Standard and SST $k-\omega$ models

3.1 Standard $k-\omega$ model

The standard $k-\omega$ model in ANSYS Fluent is based on the Wilcox $k-\omega$ model [66], which incorporates modifications for low-Reynolds-number effects, compressibility, and shear flow spreading [59]. The Wilcox model predicts free shear flow spreading rates that are in close agreement with measurements for far wakes, mixing layers, and plane, round, and radial jets, and is thus applicable to wall-bounded flows and free shear flows [59]. The standard $k-\omega$ model is an empirical model based on model transport equations for the turbulence kinetic energy (k) and the specific dissipation rate (ω), which can also be thought of as the ratio of ε to k.

3.2 Shear-Stress Transport (SST) $k-\omega$ model

The shear-stress transport (SST) $k-\omega$ model was developed by Menter [67] to effectively blend the robust and accurate formulation of the $k-\omega$ model in the near-wall region with the free-stream independence of the $k-\epsilon$ model in the far field [59]. To achieve this, $k-\omega$ model is converted into a $k-\omega$ formulation.

The SST $k-\omega$ model is similar to the standard $k-\omega$ model is similar, the SST $k-\omega$ model, but includes the following refinements [59]:

1. The standard $k-\omega$ model and the transformed $k-\epsilon$ model are both multiplied by a blending function and both models are added together. The blending function is designed to be one in the near-wall region, which activates the standard $k-\omega$ model, and zero away from the surface, which activates the transformed $k-\varepsilon$ model. [59].
2. The definition of the turbulent viscosity is modified to account for the transport of the turbulent shear stress [59].
3. The modelling constants are different.
4. The SST model incorporates a damped cross-diffusion derivative term in the ω equation.

4 Transition $k-kl-\omega$ model

The $k-kl-\omega$ transition model [68] is used to predict boundary layer development and calculate transition onset. This model can be used to effectively address the transition of the boundary layer from a laminar to a turbulent regime [59].

5 Transition SST model

The transition SST model is based on the coupling of the SST $k-\omega$ transport equations with two other transport equations, one for the intermittency and one for the transition onset criteria, in terms of momentum-thickness Reynolds number [59].

6 v^2-f model

The v^2-f model is similar to the standard $k-\epsilon$ model but incorporates near-wall turbulence anisotropy and non- local pressure-strain effects [59]. A limitation of this model is that it cannot be used to solve Eulerian multiphase problems, whereas the $k-\epsilon$ model is typically used in such applications. The v^2-f model is a general low-Reynolds-number turbulence model that is valid all the way up to solid walls, and therefore does not need to make use of wall functions [59]. Although the model was originally developed for attached or mildly separated boundary layers, it also accurately simulates flows dominated by separation [59].

The distinguishing feature of the $v^2 - f$ model is its use of the velocity scale, $\overline{v^2}$, instead of the turbulent kinetic energy, k, for evaluating the eddy viscosity [59]. $\overline{v^2}$, which can be thought of as the velocity fluctuation normal to the streamlines, has shown to provide the right scaling in representing the damping of turbulent transport close to the wall, a feature that k does not provide [59].

7 Reynolds stress models (RSM)

The Reynolds stress model is the most elaborate type of turbulence model that ANSYS Fluent provides [59]. Abandoning the isotropic eddy-viscosity hypothesis, the RSM closes the Reynolds-averaged Navier-Stokes equations by solving transport equations for the Reynolds stresses, together with an equation for the dissipation rate [59]. This means that five additional transport equations are required in 2D flows, in comparison to seven additional transport equations solved in 3D [59].

8 Detached eddy simulation (DES) model

ANSYS Fluent offers three different models for the DES simulation: the Spalart-Allmaras model, the realizable $k - \varepsilon$ model, and the SST $k - \omega$ model [59].

In the DES approach, the unsteady RANS models are employed in the boundary layer, while the LES treatment is applied to the separated regions [59]. The LES region is normally associated with the core turbulent region where large unsteady turbulence scales play a dominant role. In this region, the DES models recover LES-like subgrid models. In the near-wall region, the respective RANS models are recovered [59].

DES models have been specifically designed to address high Reynolds number wall bounded flows, where the cost of a near-wall resolving Large Eddy Simulation would be prohibitive [59]. The difference with the LES model is that it relies only on the required resolution in the boundary layers [59]. The application of DES, however, may still require significant CPU resources and therefore, as a general guideline, it is recommended that the conventional turbulence models employing the Reynolds-averaged approach be used for practical calculations [59].

The DES models are often referred to as the LES/RANS hybrid models combine RANS modelling with LES for applications such as high-Re external aerodynamics simulations. In ANSYS FLUENT, the DES model is based on the one-equation Spalart-Allmaras model, the realizable $k - \varepsilon$ model, and the SST $k - \omega$ model. The computational costs, when using the DES models, is less than LES computational costs, but greater than RANS.

9 Large eddy simulation (LES) model

In LES, large eddies are resolved directly, while small eddies are modeled [59]. This model falls between DNS and RANS in terms of the fraction of the resolved scales, as shown in figure 3.1.

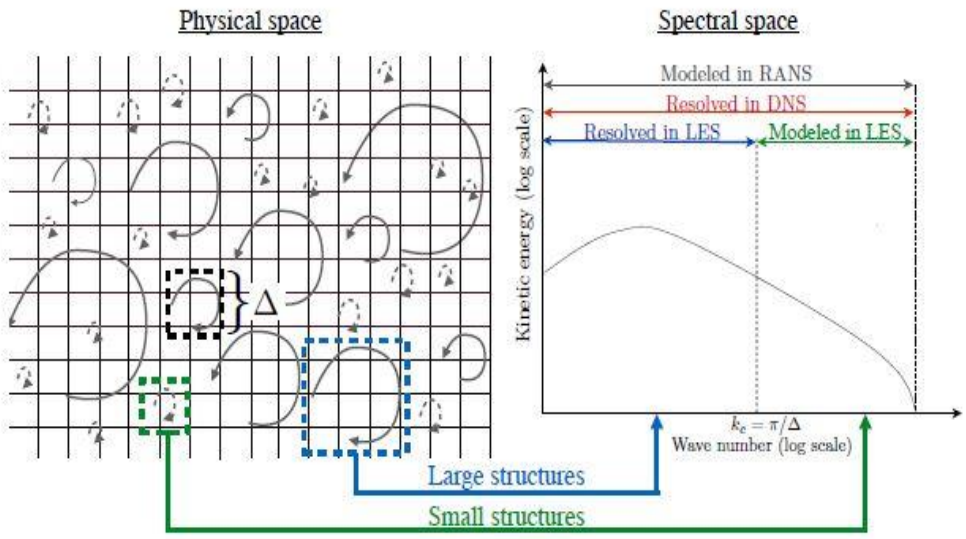

Figure 3.1 Comparison of DNS, LES and RANS simulation techniques on an idealized non-reacting homogeneous and isotropic turbulent flow. Δ stands for the LES filter size. All turbulent structures are modelled in RANS (solid and dashed arrows). All turbulent structures are resolved in DNS (solid and dashed arrows). Only large turbulent structures are resolved in LES (solid line arrows) while structures smaller than the filter size Δ are modelled (dashed line arrows) [69].

The rationale behind LES can be summarized as follows [59]:

- Momentum, mass, energy, and other passive scalars are transported mostly by large eddies.
- Large eddies are more problem dependent. They are dictated by the geometries and boundary conditions of the flow involved.
- Small eddies are less dependent on the geometry, tend to be more isotropic, and are consequently more universal.
- The chance of finding a universal turbulence model is much higher for small eddies.

The equations solved in LES are formally developed by "filtering" the Navier-Stokes equations to remove the small spatial scales and are named as "filtered" Navier-Stokes Equations. These equations describe the evolution of the large eddies and contain the subgrid-scale stress[14] tensor that represents the effects of the unresolved small scales.

A filtered variable is defined by Eq. 3.7.

[14] The subgrid-scale stresses resulting from the filtering operation are unknown and require modeling [59]. The subgrid-scale turbulence models in ANSYS Fluent employ the Boussinesq hypothesis [97] as in the RANS models [59].

$$\bar{\phi}(x) = \int_{\mathcal{D}} \phi(x')G(x,x')dx' \tag{3.7}$$

In Eq. 3.7, $\mathcal{D}$ is the fluid domain, and G is the filter function that determines the scale of the resolved eddies [59].

In ANSYS Fluent, the finite-volume discretization itself implicitly provides the filtering operation, as shown in Eq. 3.8:

$$\bar{\phi}(x) = \frac{1}{V}\int_{v} \phi(x')dx', x' \in v \tag{3.8}$$

In Eq.3.8, V is the volume of a computational cell [59].

The filter function, $G(x,x')$ is, represented in Eq.3.9.

$$G(x,x') = \begin{cases} \frac{1}{V} & ,x' \in v \\ 0 & ,x' \, otherwise \end{cases} \tag{3.9}$$

The LES capability in ANSYS Fluent is applicable to compressible flows. For the sake of concise notation, however, the theory is presented here for incompressible flows [59].

Filtering the Navier-Stokes equations, obtains Eq. 3.10 and Eq.3.11.

$$\frac{\partial \rho}{\partial t} + \frac{\partial}{\partial x_i}(\rho \bar{u}_i) = 0 \tag{3.10}$$

$$\frac{\partial}{\partial t}(\rho \bar{u}_i) + \frac{\partial}{\partial x_i}\left(\rho \bar{u}_i \, \bar{u}_j\right) = \frac{\partial}{\partial x_j}\left(\sigma_{ij}\right) - \frac{\bar{p}}{\partial x_i} - \frac{\partial \tau_{ij}}{\partial x_j} \tag{3.11}$$

In Eq.3.11, σ_{ij} represents the stress tensor due to molecular viscosity defined by the Eq.3.12.

$$\sigma_{ij} = \left[\mu\left(\frac{\partial \bar{u}_i}{\partial x_j} + + \frac{\partial \bar{u}_j}{\partial x_i}\right)\right] - \frac{2}{3}\mu \frac{\partial \bar{u}_l}{\partial x_l}\delta_{ij} \tag{3.12}$$

The τ_{ij} is the subgrid-scale stress defined by Eq.3.13.

$$\tau_{ij} = \rho\overline{u_i u_j} - \rho \bar{u}_i \bar{u}_j \tag{3.13}$$

3.1.2 Regimes of turbulent combustion

In order to derive models for turbulent combustion, a physical approach is required [9]. This approach is based on the comparison of the various time scales present in turbulent combustion [9]. The Damkohler number, as represented in Eq.3.14, is important because it compares the turbulent (τ_t) with the chemical (τ_c) time scales.

$$Da = \frac{\tau_t}{\tau_c} \tag{3.14}$$

When the Damkohler number is very large $(Da \gg 1)^2$, the flame front is thin and its inner structure is not affected by turbulence, which at most can wrinkle the flame surface [70]. This occurs when the Kolmogorov scales, which are the smallest turbulence scales, have a τ_t greater than τ_c, which means that the turbulent motions are too slow to affect the flame structure [9].

3.1.3 Choosing a Turbulence model

The choice of turbulence model depends on considerations such as the physics encompassed in the flow, the established practice for a specific class of problem, the level of accuracy required, the available computational resources, and the amount of time available for the simulation [59].

For the present study, the selected model was the LES due to the following characteristics:

1. First, the largest scales are usually the more energetic which means that the majority of the flow kinetic energy is resolved in LES [69].The impact of the small scales modelling is then limited from an energy point of view. Large scale structures are mainly controlled by walls geometry and influence mean flame features such as turbulent flame stabilization and position [69]. In the other hand, the small scales are less affected by the combustor geometry and are more isotropic. Therefore, a more universal and reliable modelling of small turbulent scales is possible in LES.
2. Another advantage compared to the RANS approach is the possibility to use the knowledge of resolved scales to model smaller ones [69].
3. Finally, as the LES filter size Δ is basically controlled by the grid size Δ_x, a mesh refinement operation is enough to increase the resolution of the resolved field and decrease the contribution of sub-grid scale (SGS) models. The resolution directly depends on the size of the mesh that can be afforded. LES tends to DNS when the mesh is sufficiently refined to capture all the length scales of the reactive flow [69].

However, this model has the following disadvantages:

1. LES still requires substantially finer meshes than those typically used for RANS calculations.
2. LES must be run for a sufficiently long flowtime to obtain stable statistics of the flow being modelled.
3. The computational cost involved with LES is normally orders of magnitudes higher than that for steady RANS calculations in terms of memory (RAM) and CPU time.
4. High-performance computing is a necessity for LES.

3.2 Model construction

As occurs with many other studies, it is very difficult to obtain the blueprint of a given combustor, due to confidentially that the GTE manufacturing companies tend to maintain. This case was no exception, the CFM56-3 combustor was provided by TAP. To obtain an accurate model of the combustor's geometry to make the mesh that will be used in simulations, a 3D scan had to be performed followed by CAD design.

3.2.1 The scanning process

The scanning of the combustor chamber was made by Jonas Oliveira [9]. In his thesis is explained that the 3D scanning device used was the Artec Spider which was provided by UBI. The Artec Spider has an outstanding accuracy for small objects and offers unlimited possibilities in reverse engineering. The scanning of the combustor was held at UBI while the scanning of the fuel injectors and the dome, were held at TAP facilities [9]. Figure 3.2 represents the 3D model combustor.

Figure 3.2 3D model combustor, obtained from the post-processing step in Artec Studio 9.2 [9].

3.2.2 Geometry construction

All the details present in the combustor were represented in figure 3.3 and figure 3.4, including the combustor walls, the dome, the dilution holes, fuel injectors and the primary/secondary swirlers. Table 3.1 shows the combustor model boundary names/type, numbered in figure 3.3 and 3.4.

However, due to the existing symmetry, only a quarter section of this combustor was used for simulation purposes to decrease the simulation time [9]. There is a fuel injector within the five

fuel injectors, that supply a richer mixture to the combustor. Figure 3.5 represents this quarter section, shading with its base alloy material, Nickel.

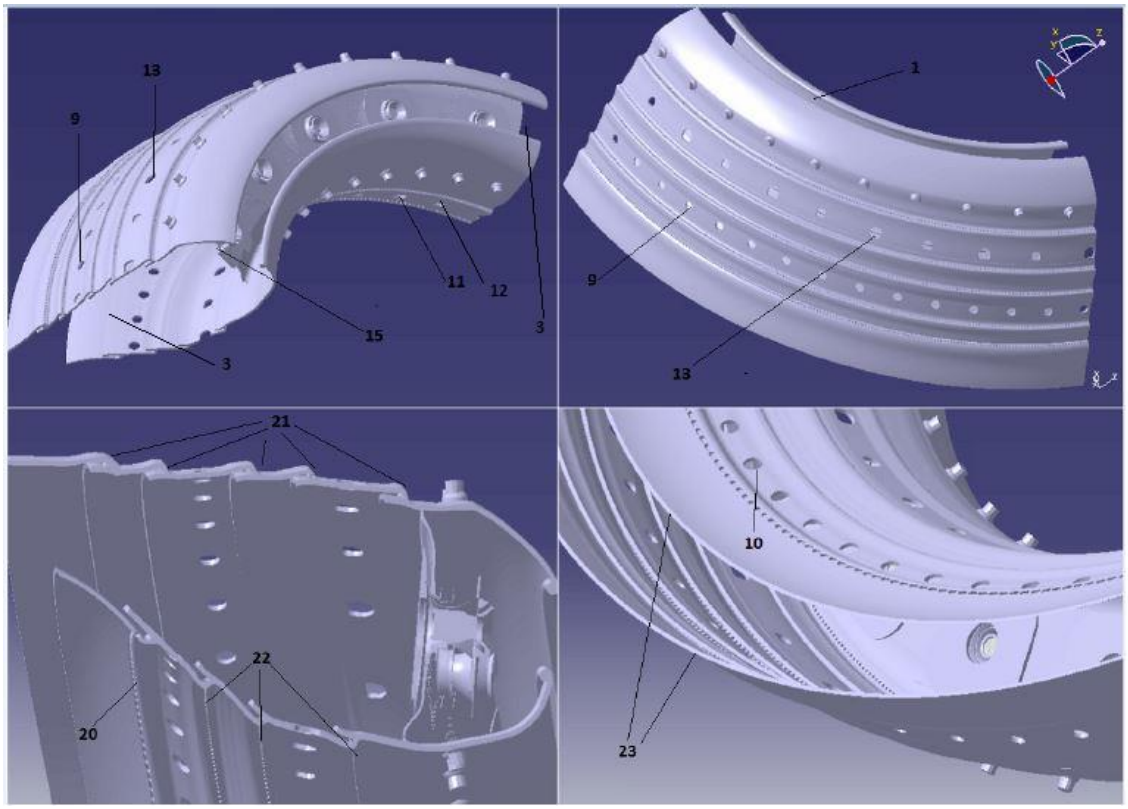

Figure 3.3 Views of the CAD combustor model section used in the simulations. Adapted from [9].

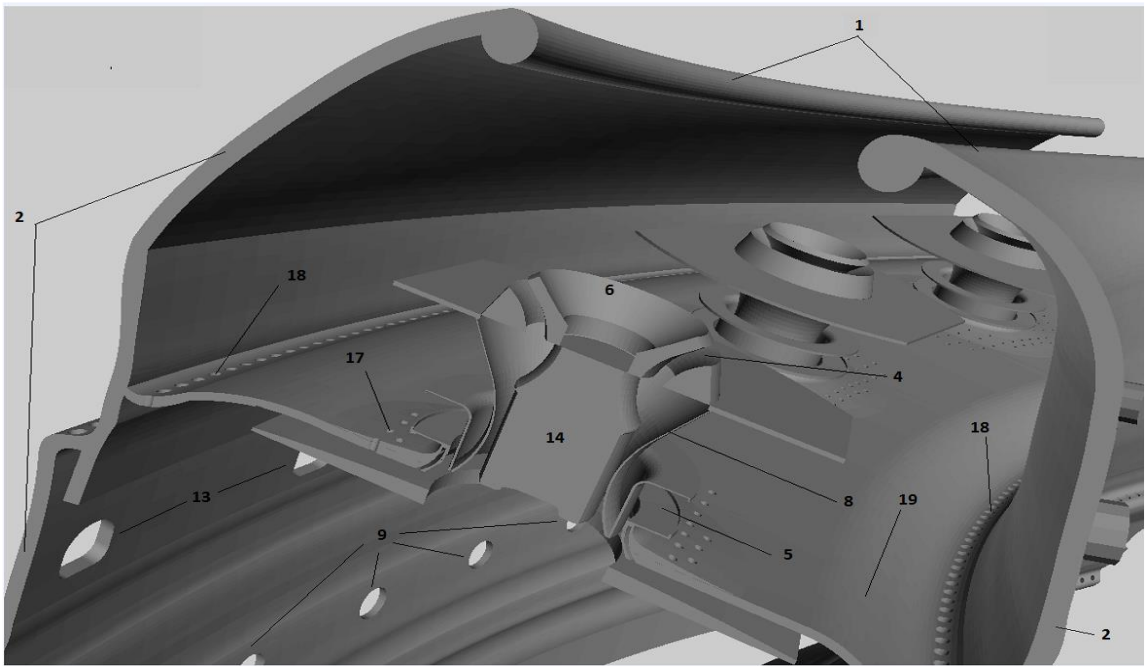

Figure 3.4 Close up on the primary and secondary swirlers, along with the placement of the fuel [9].

Table 3.1 Combustor model boundary names/type. Adapted from [9].

Numbered selection names		Correspondent figure	Boundary type
1	Top	**D.1 · D.2**	---
2	Walls	**D.2**	**Wall**
3	Symmetry[15]	**D.1**	**Wall**
4	Swirler 1	**D.2**	**Mass-flow inlet**
5	Swirler 2	**D.2**	**Mass-flow inlet**
6	Swirl cone inlet	**D.2**	**Wall**
8	Swirl cone	**D.2**	**Wall**
9	Mix	**D.1**	**Mass-flow inlet**
10	Mix2	**D.1**	**Mass-flow inlet**
11	Mix3.1	**D.1**	**Mass-flow inlet**
12	Mix3.2	**D.1**	**Mass-flow inlet**
13	Mix4	**D.1 · D.2**	**Mass-flow inlet**
14	Fuel inj	**D.2**	**Mass-flow inlet (fuel)**
15	Fuel inj rich	**D.1**	**Mass-flow inlet (fuel)**
17	Dome holes	**D.2**	**Wall**
18	Dome holes 1	**D.2**	**Mass-flow inlet**
19	Dome	**D.2**	**Wall**
20	Dil 1.1	**D.1**	**Mass-flow inlet**
21	Dil 2	**D.1**	**Mass-flow inlet**
22	Dil 2.1	**D.1**	**Mass-flow inlet**
23	Bottom	**D.1**	**Pressure-outlet**

[15] Use of symmetry boundary conditions is not permitted in LES [59]. Ansys Fluent [59] recommend use either a few sets of translational periodics or pressure inlet/outlet boundary conditions or walls if appropriate.

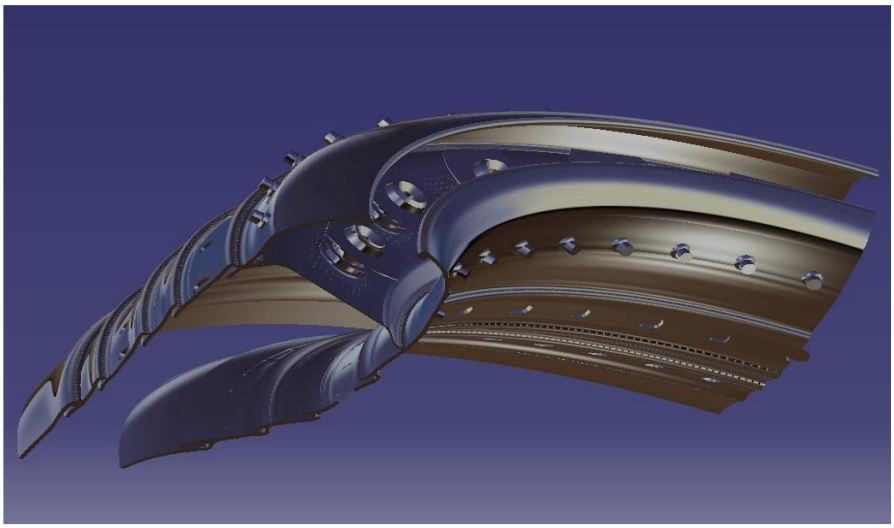

Figure 3.5 Quarter section of the combustor CAD model, shading with a Nickel alloy [9].

3.2.3 Generation of the Numerical Mesh

The mesh generation was performed using *HELYX-OS,* which is based on *SnappyHexMesh*. This software has some advantages, as a quicker mesh generation time and a user-friendly software which enables the user to better refine any given part of the mesh [9]. HELYX-OS is an OpenFoam program, and it is not available for Windows in the free version [9]. Thus, Linux is the operating system in which HELYX-OS can be freely handled.

Generating the mesh is the most important aspect in a CFD simulation, a poorly refined mesh will compromise the final results, since a too refined mesh will lead to an increase in processor and memory usage, hence an increase in time. It is therefore necessary to optimize all aspects of the mesh so that there is a good relationship between mesh size, the use of the computer and optimal simulation results [64].

The mesh that was used in this work, was obtained following the following steps:

Before setting the parameters for generating the mesh, each of the boundaries/surfaces from the model, has to be converted into the STL format in CATIA V5. After this step, these STL files are still not ready to be imported to HELYX-OS, because these STL files were created in Windows, and Linux requires its own STL format (Binary format). Blender[16] was used in the Linux system to import the STL files into the Windows format and convert them into a Linux STL format; this step has to be performed separately for each STL file.

After all the STL files being converted, we now have everything to begin the mesh generation setup [9]. First it was necessary to choose a base mesh spacing, in this case was chosen the

[16] Blender is a free and open-source 3D computer graphics software toolset used create, among others, animated films and 3D printed models.

value of 0.009. This value was chosen because it was noticed that decreasing this value, no improvements were observed in the mesh. Then the STL files are imported and the box indicating that the model was created in mm, has to be checked. For each of these STL's, the refinement level and layer addition have to be defined.

The next step is to choose the value of the refinement level. The refinement level defines how much refinement is performed with respect to the base mesh, and the higher the refinement level, finer will be the mesh around the selected surface [9]. The most important components for the simulation, in this case as air inlets and injectors, were more refined. Other regions were kept at a relatively low refinement level, so that the mesh did not have an excess of cells, without it being necessary. Although the refinement of the other components was lower, it was possible obtain a mesh refinement.

The layer addition tab is very important to study how and where to introduce layers in order to achieve the desired y^+ value. Layer addition is composed by four parameters; Number of layers (n_l), final layer thickness (δ_f), layer minimum thickness and layer stretching (δ_s).

Number of layers (n_l), is the number of layers which are intended to add to push away the mesh from the surface, in order to get a better quality mesh in that region [9]. The final layer thickness (δ_f) is the ratio between the layer in contact with the surface of the model and the Surface Cell Size (SCS) of the model surface [9].

The minimum layer thickness was left in blank in order to induce a constant layer growth and avoid a conflict of parameters, which in turn avoids errors within the mesh generation [9]. The last parameter is layer stretching (δ_s) and is defined as the expansion rate of the layers starting from the surface [9]. The value of this parameter was left with the default value that the software presents.

A feature angle has been chosen, which refines within the limits of each component, and ensures that the mesh can be "smoother" when moving from component to component. In the zones tab, was selected "Boundary "and enable de cell zone for all the boundary type. Although the tutorials explain well, it took a lot of trial and error to reach the final parameters. The parameters used are shown in table 3.2.

Table 3.2 Mesh sizing setting parameters.

Boundary Type	Refinements level	Number of layers, n_l	Final Layer thickness, δ_f	Stretching of the layer, δ_s	Feature angle
Swirlers	6	6	0.06	1.25	30
Air mass inlets	4	4	0.08	1.25	30
Fuel mass inlets	6	6	0.06	1.25	30
Pressure outlet	4	4	0.08	1.25	
Walls	4	4	0.08	1.25	
Symmetry	4	4	0.08	1.25	

The last step in the mesh setup is to define a point where a mesh cell will exist. To do this, it was needed to select a point in space inside the volume of the combustor. The material point was the coordinates: x=-0.1301mm, y=0.0792mm and z=0.0225mm. This step will then define a mesh within the closed boundaries of the model combustor. If this step was not taken the software creates a box around the combustor and refined out of the combustor to the limits of that box. The setup is then concluded, and the mesh generation can now commence. HELYX-OS will start iterating and will only create a mesh. Final mesh can be seen in figure 3.6.

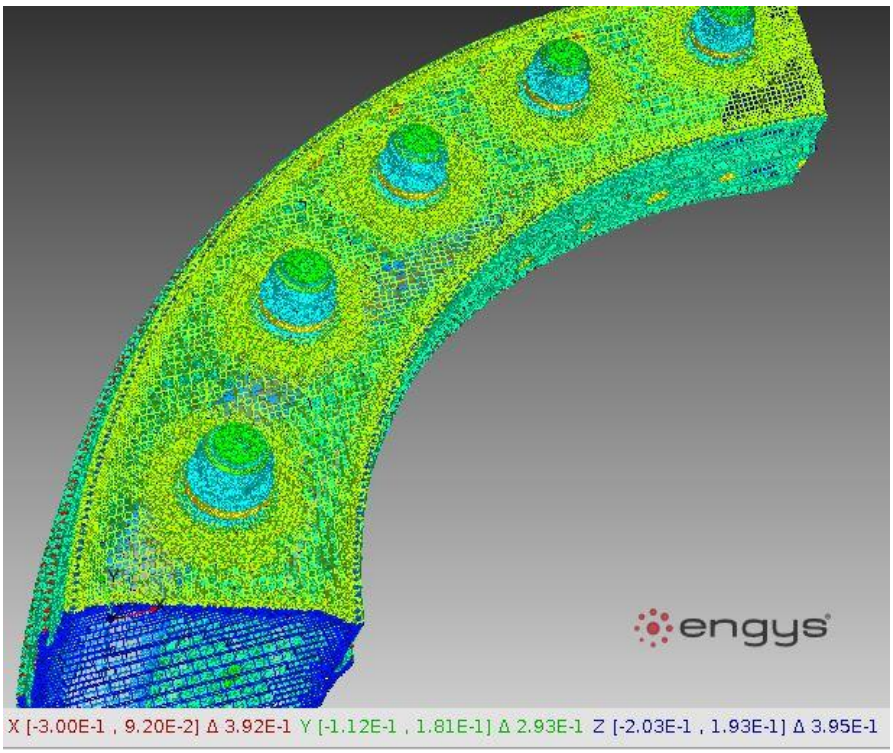

Figure 3.6 Final mesh, Software HELYX-OS.

A check mesh was made after creating a mesh, and no error was encountered, as shown in figure 3.7.

As can be seen in figure 3.8, the mesh has more than 4 million points and took about 8000 seconds to calculate.

```
Checking geometry...
    Overall domain bounding box (-0.2995214949 -0.1116225014 -0.2025369931) (0.09197850513 0.1814399986 0.1929005069)
    Mesh has 3 geometric (non-empty/wedge) directions (1 1 1)
    Mesh has 3 solution (non-empty) directions (1 1 1)
    Boundary openness (1.079897896e-14 1.484497954e-14 2.698703556e-14) OK.
    Max cell openness = 2.509727258e-16 OK.
    Max aspect ratio = 1.000000142 OK.
    Minimum face area = 1.977538922e-08.  Maximum face area = 8.100000048e-05.  Face area magnitudes OK.
    Min volume = 2.780914109e-12.  Max volume = 7.290000043e-07.  Total volume = 0.005435712597.  Cell volumes OK.
    Mesh non-orthogonality Max: 25.23940588 average: 13.26075066
    Non-orthogonality check OK.
    Face pyramids OK.
    Max skewness = 1.000000071 OK.
    Coupled point location match (average 0) OK.

Mesh OK.

End
```

Figure 3.7 Check mesh.

Statistics	
Points	4093842
Cells	2353474
Faces	8739826
Internal Faces	6861770
Boundary Patches	27
Point Zones	0
Face Zones	0
Cell Zones	0

Cell Types	
Hexahedra	1910631
Prisms	0
Wedges	0
Pyramids	0
Tet Wedges	0
Tetrahedra	0
Polyhedra	442843

Figure 3.8 Statistics of the mesh.

3.3 Choosing the jet fuels

The jet fuels selected for this study were Jet A, Jet B and TS-1. Table 3.3 shows the properties of these jet fuels.

The RP-3 jet fuel has not been chosen for this study due to the lack of information.

Table 3.3 Conventional Jet Fuel Properties. Adapted from [1].

Property	Jet A/Jet A-1	Jet B	TS-1
Approximate formula[17]	$C_{11}H_{21}$	$C_{8.5}H_{17}$	$C_{12}H_{23}$
$\boldsymbol{H/C}$ **ratio**	1.91	2.00	1.95
Boiling range, (℃)	165-265	60-240	175-275
Freeze Point, max, (℃)	Jet -A: -40 Jet-A1: -47	-62	-50
Flash Point, min, (℃)	38	-23	28
Net Heat of Combustion, max, $(\boldsymbol{MJ/kg})$	43.15	43.15	43.2
Specific gravity, $\boldsymbol{16}$ ℃**,max**	0.81	0.76	0.81
Average composition			
Aromatics $(\boldsymbol{vol}\%)$	18	10	3
Naphthenes	35	29	58
Paraffins	45	59	39
Olefins	2	2	
Sulfur $(\boldsymbol{ppm})$	490	370	20

3.4 Simulation set up

The software used to perform this simulation was ANSYS Fluent 16.2. Before starting the simulation in Ansys, it is necessary to transform the mesh format with the code *foamMeshToFluent*, which writes out the *OpenFoam* mesh in ANSYS Fluent mesh format.

When initiating ANSYS Fluent, a window named Fluent Launcher is displayed. Here it is necessary to ensure that 3D dimension is checked, and it is required enable the option of single or double precision. If double precision is enabled, the solution will be slower, but the results will be more accurate. Running with double precision, resulted in roughly 4 times more time then running the simulation in single precision. For this fact, it was enabled the single precision.

Once ANSYS Fluent is launched, the quality of the mesh must be checked as this greatly affects the solution's convergence and results. Then, some important aspects regarding mesh quality are displayed; these are the aspect ratio, orthogonal quality and mesh skewness.

Figure 3.9 shows the maximum values obtained regarding the aspect ratio and mesh skewness and the minimum orthogonal quality.

[17] For illustration of average carbon number, not designed to give accurate H/C ratios [1].

```
Mesh Quality:

Minimum Orthogonal Quality =  8.16497e-01
(Orthogonal Quality ranges from 0 to 1, where values close to 0 correspond to low quality.)

Maximum Ortho Skew =  1.83503e-01
(Ortho Skew ranges from 0 to 1, where values close to 1 correspond to low quality.)

Maximum Aspect Ratio =  1.73205e+00
```

Figure 3.9 Command window of ANSYS Fluent with the report quality.

3.4.1 Models

ANSYS Fluent is a very versatile code, and so there are a variety of models that can be chosen depending on the necessity of the simulation. For this setup, six models were used:

1. Energy model – This model must be activated as this regards the energy related to the temperature change within the combustion process or heat transfer [9].
2. Viscous Model - As discussed in section 3.1.3, the model chosen was the LES and all constants were maintained. WALE was enabled, because it is the sub-model recommended by the User´s Guide of ANSYS Fluent [59] to the combustion.
3. Radiation model[18] - It was chosen the Discrete Ordinates (DO) radiation model, because produces a more accurate solution than the P1 radiation model, but its drawback is a higher CPU cost [59].
4. Species model - This model has to be enabled to ANSYS Fluent model the mixing, transport and combustion of chemical species [9]. Due to the importance of this model for this work, the inputs will be explained in detail [9].

The first step was select non-premixed combustion, since it describes the combustor system in study. Regarding the PDF creation, it was selected the inlet diffusion. The inlet diffusion option includes the diffusion flux of species at the flow inlet. In *chemistry tab*, chemical equilibrium is selected for state relation. The non-adiabatic was enabled in the energy treatment so that the model considers any loss or gain due to chemical reactions. In the model settings, the operating pressure and the Fuel Stream Rich Flammability limit (FSRFL) are displayed in table D.2 and D.1 (see Appendix D), respectively. The FSRFL is a value larger than 10% of the stoichiometric mixture fraction can be used. The stoichiometric values of Jet A, Jet B and TS-1 are calculated using the Eq.2.42.

The specification of the fuel species name and concentration is done in the *boundary tab*. In the present tab, the oxidizer species and concentration, as well as the temperatures of the oxidizer and the fuel have to be introduced. The oxidizer was considered composed only by

[18] Many combustion simulations tend to ignore the effect of radiation in the calculations, because the governing radiative transfer equation is of integro-differential nature which makes the analysis difficult and computationally expensive [98].

nitrogen and oxygen with concentrations of 0.78992 and 0.21008, respectively. As for the fuel temperature, this gives respect to the flashpoint of each fuel, which is presented in table D.1 (see Appendix D). Just like the operating pressure, the oxidizer temperature varies through the GTE's power setting, and the values of this parameters are presented in table D.2 (see Appendix D).

In table *tab*, *Automated Grid Refinement* was enabled. Finally, the PDF table can be calculated and Fluent will calculate and display the result as how many species created and can be check under the *Materials*.

5. NO_x - This model has to be enabled to ANSYS Fluent display information regarding NO_x formation when the solution is calculated. Here Thermal and Prompt NO_x [19] has to be selected, and the species that are present in the fuel must also be chosen. *Partial-equilibrium* must be chosen in the *Thermal tab* as this predicts the *O* radical concentration required for thermal NO_x prediction [59]. The fuel carbon number as well as its equivalence ratio must be introduced, and *temperature* is important to be selected in the PDF mode as this will enable the turbulence-chemistry interaction [59].
6. Discrete Phase Model- This model simulates the dispersion of spherical particles. In this model, it is calculated the heat and mass transfer to/from them. The type of injection chosen was solid cone and the option of the number of particles per injector was 2000. The diameter of each particle was changed to 1×10^{-5} meters. Fuel injection temperature inserted was the flashpoint of fuels, present in table D.1 (Appendix D), and the components of the injection direction vector were also defined. Figure 3.10 illustrates the cone injector geometry.

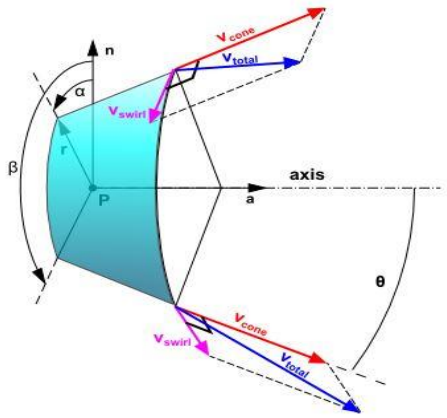

Figure 3.10 Cone injector geometry [59].

[19] The selection of Thermal and Prompt NO_x models is justified in the section 2.6.2.4.

3.4.2 Boundary Conditions

As was said in the section 3.2, the manufacturers maintain most of their GTE's technical information confidential. For this reason, was extremely difficult achieve the total $\dot{m}_a$ that is ducted through the fan stage, and practically no information is provided regarding this aspect.

Ribeiro's work [71] encountered the solution for this problem. Ribeiro investigated the thermodynamic model of the CFM56-3, using *GasTurb*, which is a powerful cycle program used for simulating the most common types of GTE's. It was obtained through the Ribeiro's work [71] important aspects regarding each stage of the GTE, namely $\dot{m}_a$, temperature and pressure, at full power. The relevant information of this work is presented in table D.3 (see Appendix D).

Only $1/4$ of the combustor is studied, for that reason the boundary conditions where determined by dividing by four the total $\dot{m}_a$ and $\dot{m}_f$, and from the overall AFR. The typical values for GTE's operating AFR are stated by Bryn Jones [72] and are between 33-40 at 100% power, and approximately 100 at 7% power. The overall AFR calculated in this work was 43.6 at full power, which represents a difference of 7% from the upper limit stated by Bryn Jones [72]. In order to achieve an AFR between the stated values, the total $\dot{m}_a$ would have to be reduced; thus, it was opted to use the calculated AFR as this used all of the air obtained from Ribeiro's work [71].

The first step was then to ensure that at the PZ, the AFR was at stoichiometric conditions [9]. The total $\dot{m}_f$ is divided with the 5 fuels injectors, and 10% more fuel was considered in the richer fuel injector than the remaining four [9].

The $\dot{m}_a$ that enters the PZ is done through the primary and secondary swirlers, and as so its $\dot{m}_a$ can then be determined [9]. Knowing the overall AFR and fuel flow, it is possible to determine the total $\dot{m}_a$ and then calculate the total cooling $\dot{m}_a$, by subtracting the PZ $\dot{m}_a$ from the total $\dot{m}_a$ [9]. The determination of which percentage of cooling $\dot{m}_a$, to apply in each boundary was only possible through an extensive trial and error approach through the simulations, in which the aim was to achieve the exit temperature [9]; this temperature is presented in table D.3 (see Appendix D). The percentage of cooling air that is applied to each boundary was known when the exit temperature was achieved [9]. The boundary conditions for the remaining power settings were then similarly determined from this reference [9]. The relevant data for the boundary condition while burning Jet A are presented in table 3.4, and table D.6 and D.7 (see Appendix D) show these values when burning TS-1 and Jet B, respectively.

Table 3.4 Mass flow inlet (kg/s) for each boundary, at its respective power setting, while burning Jet A.

Boundary condition	Name	Air mass flow (kg/s) to each Fuel Power (%)				Cooling air flow (%)
		100	85	30	7	
Mass flow inlet	Domes holes 1	0.0124	0.0129	0.0091	0.0026	0.1851
Mass flow inlet	Dil.1.1	1.4719	1.5282	1.0742	0.3034	21.9534
Mass flow inlet	Dil.2	2.9439	3.0564	2.1483	0.6074	43.9068
Mass flow inlet	Dil.2.1	1.6682	1.7320	1.2174	0.3438	24.8805
Mass flow inlet	Mix	0.2943	0.306	0.2148	0.0607	4.3907
Mass flow inlet	Mix 2	0.2943	0.306	0.2148	0.0607	4.3907
Mass flow inlet	Mix 3.1	0.0049	0.0051	0.0036	0.0010	0.0732
Mass flow inlet	Mix 3.2	0.0049	0.0051	0.0036	0.0010	0.0732
Mass flow inlet	Mix 4	0.0098	0.0102	0.0072	0.0020	0.1464
Mass flow inlet	Swirler	1.7052	1.4494	0.5115	0.11907	---
Mass flow inlet	Swirler 2	1.7052	1.4494	0.5115	0.11907	---
Mass flow inlet	Fuel inj.	0.1819	0.1546	0.05457	0.0127	---
Mass flow inlet	Fuel. Inj. rich	0.05011	0.0426	0.01503	0.0035	---
	Total $\dot{m}_a$	10.1152	9.8600	5.916	1.6200	---
	Total cooling $\dot{m}_a$	6.7048	6.9611	4.8929	1.3819	$\approx$ **100**
	Fuel flow ($\dot{m}_f$)	0.2320	0.1972	0.0696	0.0162	
	Overall AFR	**43.6**	**50**	**85**	**100**	
	PZ AFR	**14.7**				

Three types of boundary conditions were applied; mass flow inlet's, pressure-outlet and walls. These boundaries are distinguished in table 3.1. Still in the boundary condition settings, the direction of the flow is set to normal to boundary for all the boundaries. In the *thermal tab*, the stream temperature has to be introduced accordingly these being air inlets or fuel inlets [9]. In the *species tab*, the *Mean Mixture Fraction* has to be set to unity, when injecting fuel (fuel injectors) and the *Pollutant NO mass Fraction* and the *Mixture Fraction Variance* were maintained [9].The *wall* boundaries were remained at default settings and the *exit gauge pressure* was set to zero as this considers the system pressure at the exit to be the operating pressure[20] [9]. In the DPM *tab*, the reflect type is assumed at the walls with both coefficients of restitution equal to 1.0 and the escape type is assumed at all flow boundaries [59].

[20] This means that there is no pressure loss within the combustor, which is what engineers aim for [9].

3.4.3 Solution Methods, Solution Controls and Monitors

Large eddy simulation involves running a transient solution from some initial condition, on an appropriately fine mesh, using an appropriate time step size [59]. The solution must be run long enough to become independent of the initial condition and to enable the statistics of the flow field to be determined [59].

The following are suggestions to follow when running a large eddy simulation [59]:

1. Start by running a steady state flow simulation using a Reynolds-averaged turbulence model, for example RSM. Run until the flow field is reasonably converged. It will create a much more realistic initial field for the LES run [59]. Additionally, it will help in reducing the time needed for the LES simulation to reach a statistically stable mode. The solution control parameters for flow courant number, explicit relaxation factor (ERF) and under-relaxation factor (URF) and the solutions methods that were used in this simulation are presented in table D.4 and table D.5 (see Appendix D), respectively.
2. When the LES is enabled, ANSYS Fluent will automatically turn on the unsteady solver option [59]. It is needed to set the appropriate time step size and all required solution parameters.
3. Run LES until the flow becomes statistically steady. The best way to see if the flow is fully developed and statistically steady is to monitor forces and solution variables at selected locations in the flow [59].
4. Before restart the solution, it is necessary enable Data Sampling for Time Statistics in the Run Calculation task page. With this option enabled, ANSYS Fluent will gather data for time statistics while performing a large eddy simulation [59]. When Data Sampling for Time Statistics is enabled, the statistics collected at each sampling interval can be postprocessed and you can then view both the mean and the root-mean-square values in ANSYS Fluent [59].

The parameters used are presented and explained in detail in the following sections of this chapter.

3.4.3.1 Solution methods

Spatial Discretization

The recommended choice for momentum equation is the Bounded Central Difference scheme, especially for complex geometries and flows [73], as the case of the present work. The Bounded Central Difference scheme is slightly more dissipative but is substantially more robust and is therefore frequently the optimal choice [73]. With LES, Least Square Cell Based gradient method is essential in ANSYS Fluent, as it allows a better representation of the second derivative of the velocity field that is required for the model formulation (von Karman length scale) [73].

It was selected Coupled to the Pressure-Velocity Coupling. This solver is the recommended by ANSYS [59] when large time steps are used to solve the transient flow.

Temporal Discretization

The Bounded Second Order Implicit formulation was selected to temporal discretization. This solver provides better stability and improves accuracy [59].

Table 3.5 shows the original settings against the new settings adopted for the solution controls used in LES simulation.

Table 3.5 Solution method parameter setting, used in LES simulation.

Parameters	Original	New setting
Pressure-Velocity Coupling	SIMPLE	Coupled
Gradient	Green-Gauss Cell Based	Least Square Cell Based
Pressure	Standard	PRESTO!
Momentum	First Order Upwind	Bounded Central Difference
Pollutant no	First Order Upwind	Second Order Upwind
Discrete Ordinates	First Order Upwind	Second Order Upwind
Energy	First Order Upwind	Second Order Upwind
Mean Mixture Fraction	First Order Upwind	Bounded Central Difference
Transient	First Order Upwind	Bounded Central Difference

3.4.3.2 Solution controls

The default values for the solution controls are considered too aggressive for the type of combustion system in study [59], and as so, most of these values had to be reduced. In the Coupled, it was needed to specify the Courant number, in the Solution Controls task page. Eq.3.15 represents the Courant -Friedrichs-Levy. For a stable and efficient calculation, the Courant number should not exceed a value of 20-40 in most sensitive transient regions of the domain [59].

$$Courant\ Number = \frac{U\Delta t}{\Delta x} \tag{3.15}$$

Many errors appeared, and it was only by trying various settings for the solution controls and reducing the URF´s, that these were overcome.

Table 3.6 shows the original settings against the new settings adopted for the solution controls.

Table 3.6 Solution control parameters for flow courant number, explicit relaxation factor (ERF) and under-relaxation factor (URF), used in LES simulation.

Parameters	Original value	New value
Flow Courant Number	200	1
ERF: Momentum	0.75	0.3
ERF: Pressure	0.75	0.3
URF: Density	1	0.3
URF: Body Force	1	0.5
URF: Pollutant NO	0.9	0.6
URF: Energy	1	0.3
URF: Temperature	1	0.3
URF: Discrete Ordinates	1	1
URF: Mean Mixture Fraction	1	0.6
URF: Discrete Phase Sources	0.5	0.5

3.4.3.3 Monitors

The purpose of the *monitors* is to display the value for a certain parameter and then check if it is converging [59]. For the monitoring of the calculation process, the residual of convergence criteria used was *Absolute*.

3.4.4 Solution initialization and Calculation set-up

The option *standard initialization,* provided by ANSYS Fluent, was selected because this option proved that the initial values were adequate, and the solution was converging smoothly and relatively quickly. In the Run simulation page task, time step size, Max Iterations/Time Step and the Number of Time steps need to be set.

Max Iterations/Time Step sets a maximum for the number of iterations per time step [59].

The time step size (Δt) is the magnitude of time step [59]. To model transient phenomena properly, it is necessary to set Δt at least one order of magnitude smaller than the smallest time constant in the system being modelled [59].

The duration of the simulation can be determined beforehand by estimating the mean flow residence time in the solution domain (L/U, where L is the characteristic length of the solution domain and U is a characteristic mean flow velocity) [59]. Knowing the duration of the simulation and the smallest time constant in the system being modelled, which is the ratio between smallest edge length (Δx) and characteristic mean flow velocity, it is possible to know the Δt and the number of time steps, represented in Eq. 3.16:

$$Number\ of\ Time\ steps = \frac{Duration\ of\ the\ simulation}{\frac{\Delta x}{U}} \tag{3.16}$$

To improve the convergence of the transient calculations, the Extrapolate Variables option on the Run Calculation task page has been enabled. This option instructs ANSYS Fluent to predict the solution variable values for the next time step using a Taylor series expansion, and then inputs that predicted value as an initial guess for the inner iterations of the current time step [59].

Regarding the calculation set-up, it is of good practice to first *check case* before the calculation process starts, as this ensures that there are no errors within the case, and the model is ready to be simulated [74].

Chapter 4

Results

The present chapter presents the results for the parameters that were intended to simulate, for the combustion of conventional jet fuels in the CFM56-3 combustor, throughout ICAO's LTO cycle. A total of 12 simulations compose the results, four simulations to each jet fuel.

This chapter will start with an evaluation of convergence, regarding the quality of the numerical solution; an evaluation of the y^+ to make sure that this parameter is between the recommended range and an evaluation of the combustor's exit temperature. The emissions, which are the primary goals for this study, are finally presented separately for each fuel, throughout the mentioned power cycle.

4.1 Convergence

There are three indicators that convergence has been reached [59]:

1. The residuals have decreased to a sufficient degree [59].

The solution has converged when the Convergence Criterion for each variable has been reached. The default criterion is that each residual will be reduced to 10^{-3}, except the energy residual, for which the default criterion is 10^{-6} .

2. The solution no longer changes with more iterations [59].

3. The overall mass, momentum, energy, and scalar balances are obtained [59].

A way of checking if the residuals tolerance are correct, and the solution completely converges, is through the mass imbalance. The net imbalance should be less than 0.5 % of the net flux through the domain when the solution has converged, i.e., the flow that enters the system should be equal to that going out [59]. In the present study, the mass imbalance obtained was $E^{-3}\%(\approx 0)$, which is a strong proof that the solution is completely converged and therefore correct, for the problem setup.

4.2 Y^+

The wall y^+ is a non-dimensional number similar to local Reynolds number, determining whether the influences in the wall-adjacent cells are laminar or turbulent, hence indicating the part of the turbulent boundary layer that they resolve [75]. It is the ratio between the turbulent and laminar influences in a cell [75].

The subdivisions of the near-wall region in a turbulent boundary layer can be summarized as follows [59]:

1. y^+< 5: in the viscous sublayer region.
2. 5 < y^+< 30: buffer region.
3. 30 < y^+< 300: Fully turbulent portion or log-law region.

Very close to the wall, viscous damping reduces the tangential velocity fluctuations, while kinematic blocking reduces the normal fluctuations [75]. Towards the outer part of the near-wall region, however, the turbulence is rapidly augmented by the production of turbulent kinetic energy due to the large gradients in mean velocity [75].

Accurate presentation of the flow in the near-wall region determines successful prediction of wall-bounded turbulent flows. Values of y^+close to the lower bound (y^+ ≈30) are most desirable for wall functions whereas y^+ ≈1 are most desirable for near wall modeling [76].

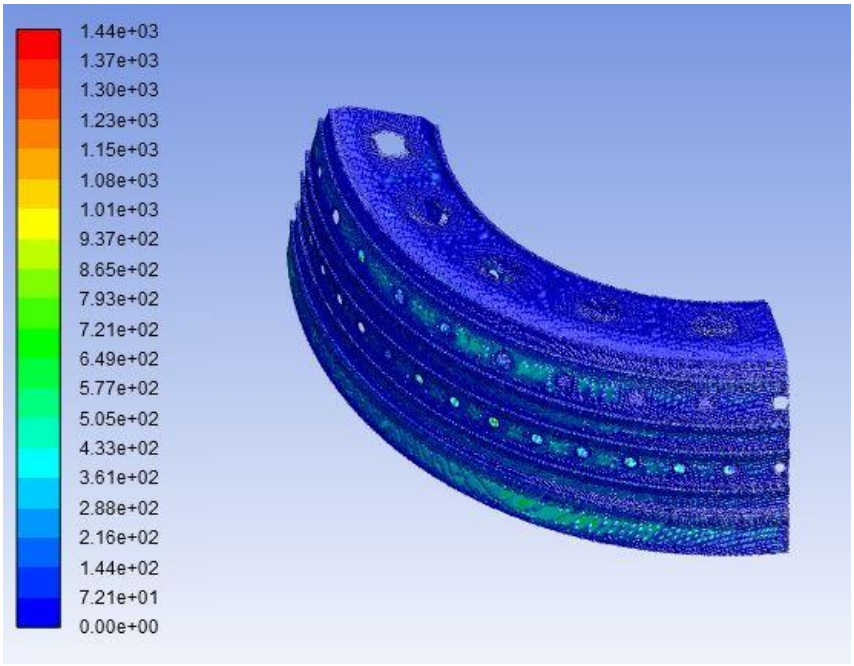

Figure 4.1 y^+ regarding the walls of the combustor.

The average value obtained was 94. In figure 4.1 is possible to see that there are some zones that acquire a high y^+ value. This means that the mesh in these zones needs to be more refined,

but as the use of the computer was already on the limit, it would be more difficult to be refined as the desired areas. In addition, it is a complex geometry of the model combustor, which makes it more difficult to develop a more refined mesh.

However, this parameter is not important because in this study is not considered the heat transfer.

4.3 Validation Results

All the results presented in this chapter were validated by comparing with ICAO's emissions measurements, presented in table 2.6. Results of this comparison can be observed in figures 4.2, 4.3 and 4.4.

The pollutant emissions of most concern for the aircraft gas turbine are oxides of nitrogen (NO_x), carbon monoxide (*CO*), unburned hydrocarbons (UHC) and smoke. The concentration levels of these pollutants can be related directly to the temperature, time, and concentration histories of the gases within the combustor [77]. These histories vary from one combustor to another and, for any given combustor, with changes in operating conditions [77]. The nature of pollutant formation is such that the concentrations of carbon monoxide and unburned hydrocarbons are highest at low-power conditions and diminish with increase in power. In contrast, oxides of nitrogen are insignificant at low power settings and attain maximum values at the highest power condition.

Analysing figures 4.2, 4.3 and 4.4 it can be concluded that the behaviour regarding the amount of NO_x emissions produced throughout ICAO's LTO cycle was expected. However, UHC and *CO* emissions resulted in an erratic behaviour. This behaviour disagreement is explained in section 4.5.2.

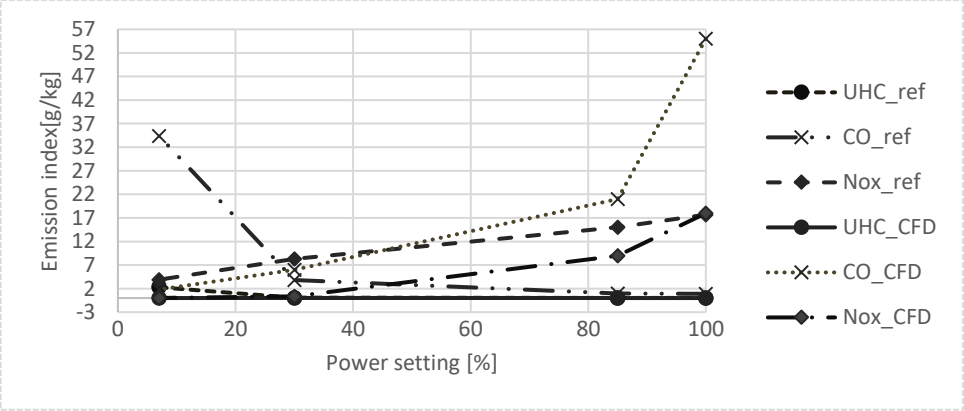

Figure 4.2 Results validation: ICAO's measures vs CFD calculations while burning Jet A.

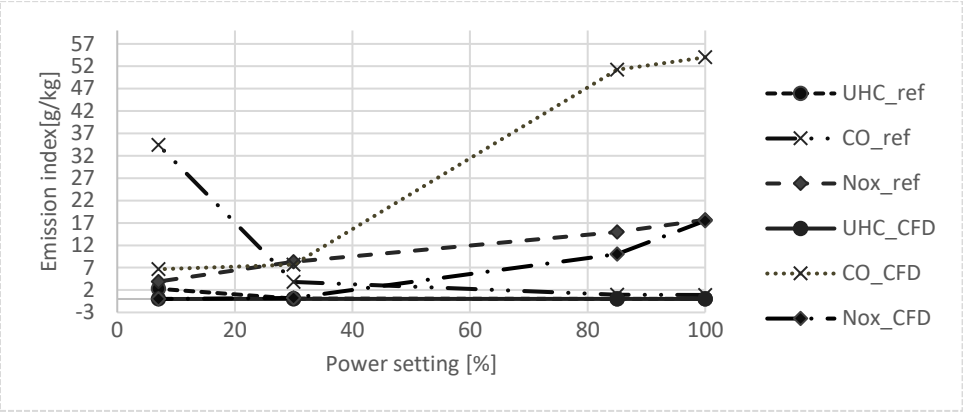

Figure 4.3 Results validation: ICAO's measures vs CFD calculations while burning Jet B.

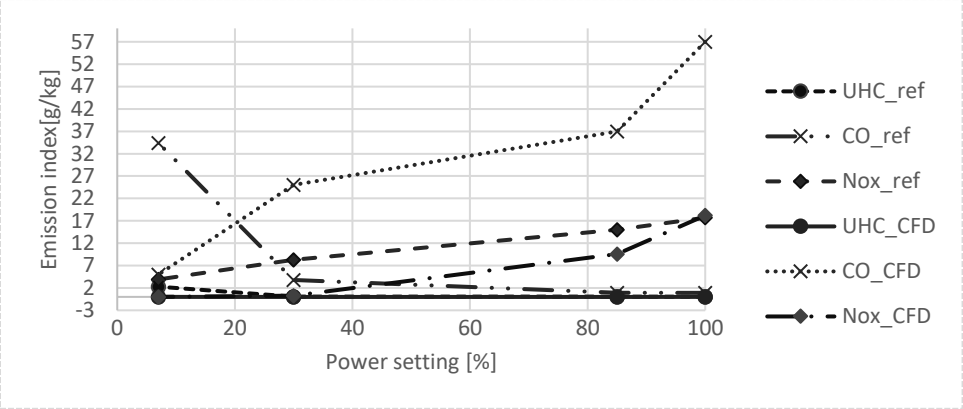

Figure 4.4 Results validation: ICAO's measures vs CFD calculations while burning TS-1.

4.4 Combustor exit temperature

As referred in the section 3.4.2, the reference temperature for this work is 1650K, present in table D.3 (see Appendix D) obtained from Ribeiro's work [71]. As can be seen in the figure 4.5, this temperature was not reached. The reference temperature could be achieved by reducing the overall AFR, but it was opted to maintain the boundary conditions calculated in the section 3.4.2, because these were considering the total $\dot{m}_a$ of the CFM56-3 combustor, at full power.

Jet B and TS-1 presented similar temperatures for all the power settings. At 30% power, all the jet fuels presented the same combustor exit temperature. Analysing figure 4.5, it is also possible to see that Jet A presented the highest exit temperature at full power.

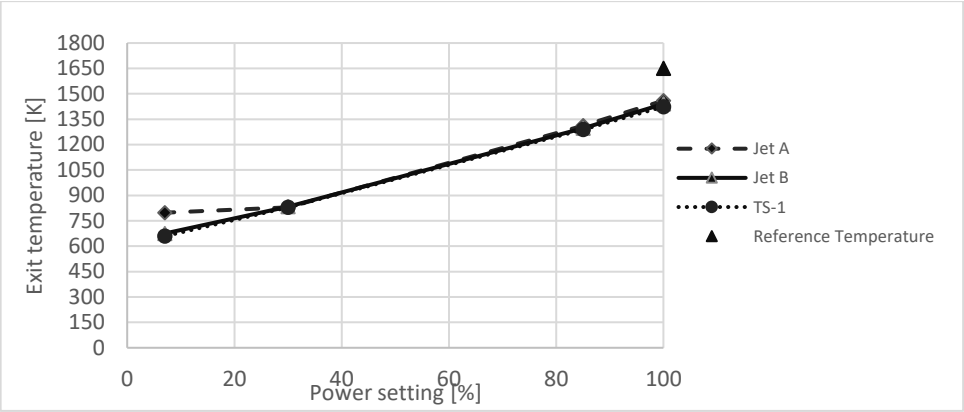

Figure 4.5 Combustor exit temperature throughout ICAO's LTO cycle, while burning Jet A, Jet B and TS-1.

Analysing figure 4.6 and 4.7, it is possible to notice a variation of the hot zones within the combustion chamber, and this will affect some zones of the gas turbine, reduce the life of turbine blades and vanes and influence the engine performance. The temperature pattern factors are controlled by a few geometrical parameters such as liner front-end air passages, primary air holes, atomizer characteristics and air swirl number and dilution zone geometrical configuration.

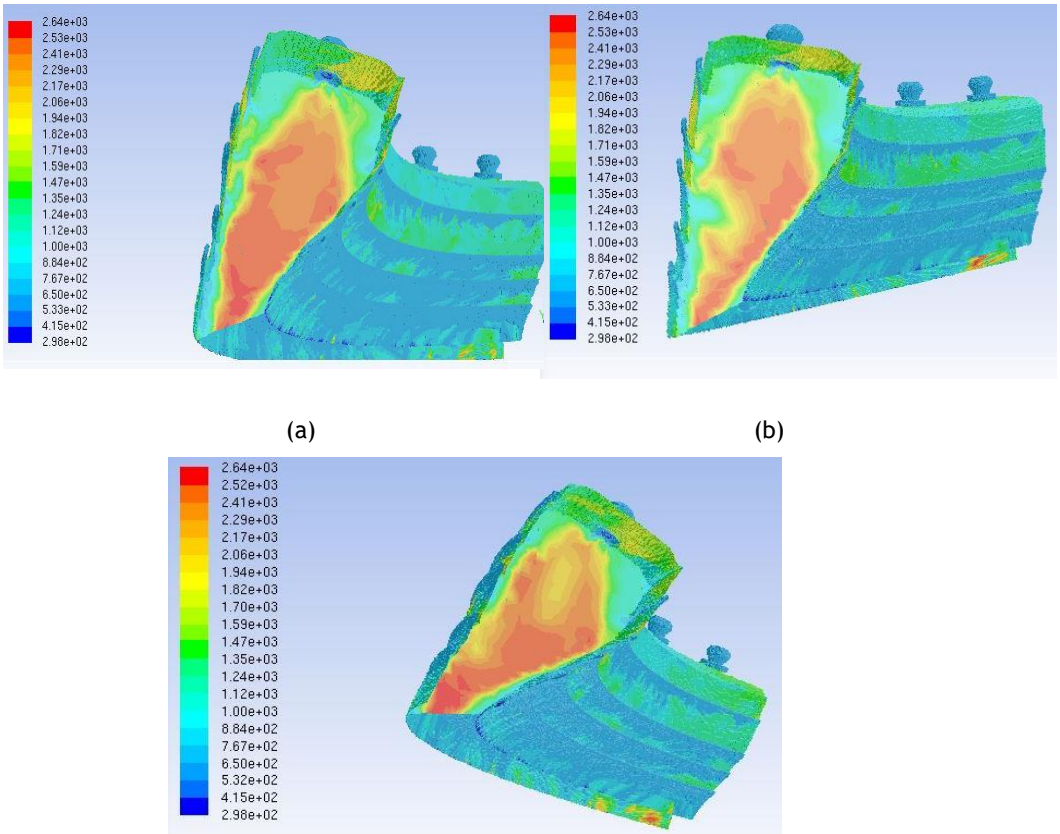

(a) (b)

(c)

Figure 4.6 Contours of the cross section temperature (K), while burning Jet A (a), Jet B (b) and TS-1 (c), at full power.

Analysing figures 4.6 and 4.7, it can be concluded that as power setting increases, so does the high temperature zone, because more fuel is being burned.

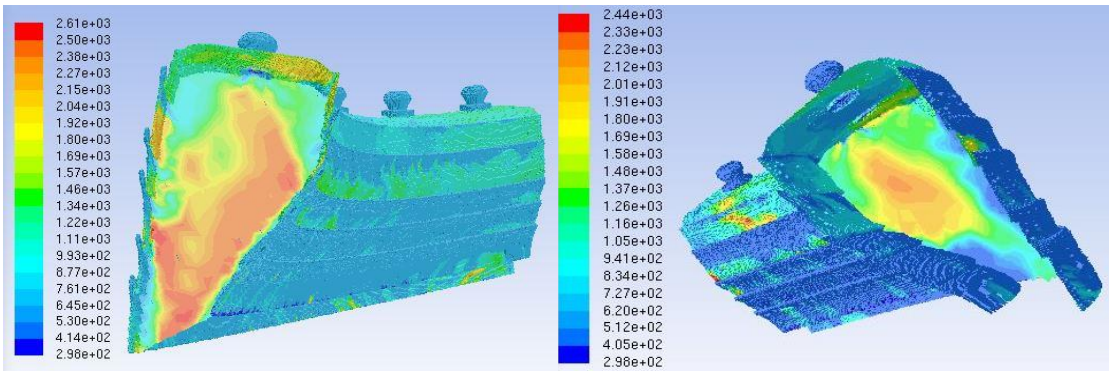

(a) (b)

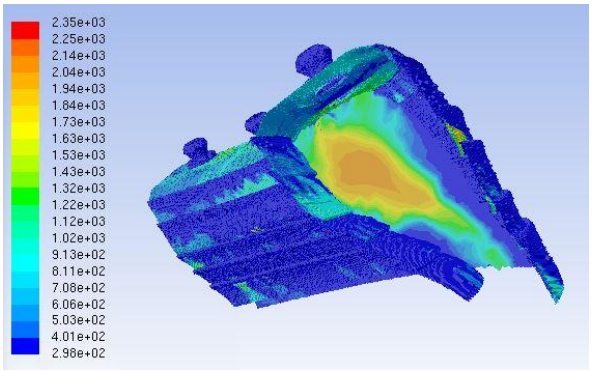

(c)

Figure 4.7 Contours of the cross section temperature (K), while burning TS-1, at 85% power (a), at 30% power (b) and at 7% power (c).

4.5 Emission Analyses

All the results presented in this section were obtained using Eq.4.1:

$$\frac{Emission\ flow\ rate\left[\frac{kg}{s}\right]\times 1000}{Inlet\ \dot{m}_f\left[\frac{kg}{s}\right]} \tag{4.1}$$

In equation 4.1, the emission flow rate was obtained by reporting the emission *Flow rate* in Ansys Fluent. The values used for the total $\dot{m}_f$ at the inlet are present in tables 3.4, D.6 and D.7. The results are presented in the form $g[\,Emissions]/kg[fuel]$, which allows comparing with the ICAO´s reference data.

4.5.1 Oxides of nitrogen

As referred in the section 4.3.1, oxides of nitrogen emissions are insignificant at low power settings and attain maximum values at the highest power condition.

As can be seen in figure 4.8, NO_x emissions represented a little margin of error from ICAO's reference values. However, in general, it was obtained a good approach to the reference values.

Still, in figure 4.8, it can be verified that Jet A presented the lowest value of EI (NO_x) at cruise and TS-1 presented the highest value of EI (NO_x), at take-off. All the fuels presented similar values of EI (NO_x), at approach and idle. Overall, it is possible to conclude that Jet B presented the lowest values of EI (NO_x) at take- off, approach and idle.

The results of EI (NO_x), present in figure 4.8, consider the thermal NO_x and prompt NO_x that reached the combustor's exit.

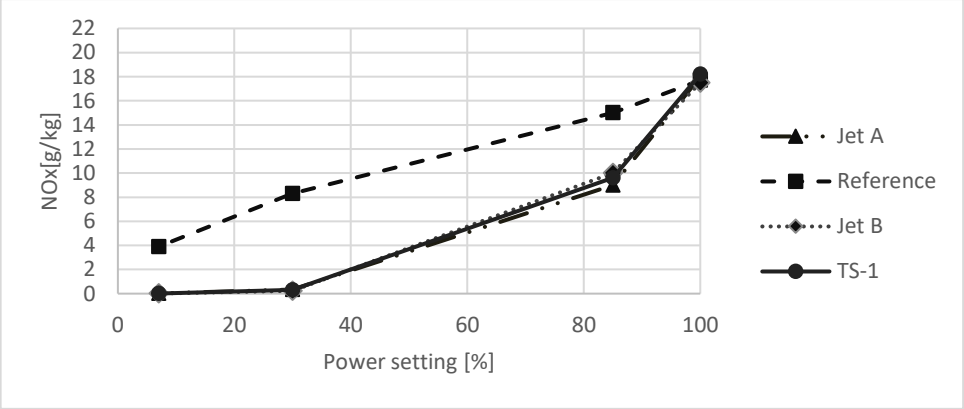

Figure 4.8 EI results of NO_x, resultant from the combustion of Jet A, Jet B and TS-1, throughout ICAO's LTO cycle.

As said in the section 2.6.2.4, and as can be seen in figure 4.9, the thermal NO_x is the leading mechanism for NO_x formation at the highest temperatures of the PZ, and prompt NO_x is only formed in fuel rich regions. Also, it can be observed that the concentration of prompt NO_x is higher in the region of the richer fuel injector, and just accounted for 2% of the total NO_x formed in the combustor. This percentage did not vary with the type of jet fuel.

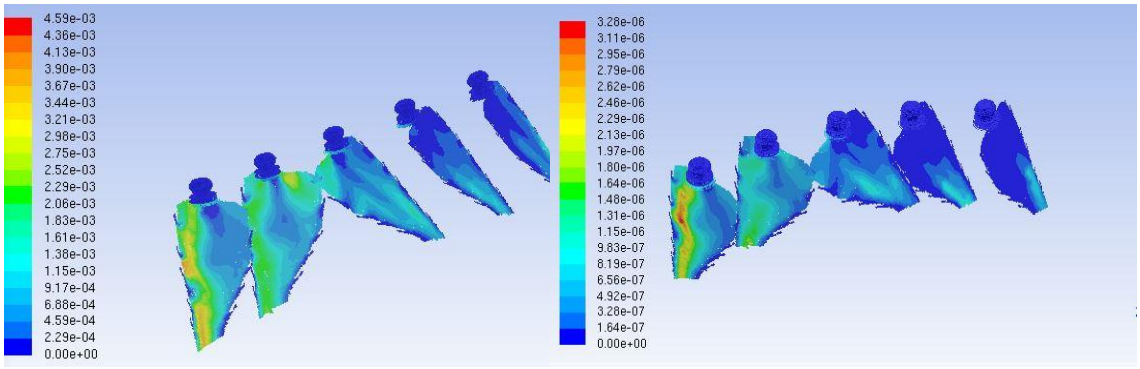

(a) (b)

Figure 4.9 Contours of thermal NO_x concentration [kg/kg] (a) and prompt NO_x concentration [kg/kg] (b), while burning Jet A, at full power.

The high peak temperatures are located within the PZ, as can see in figures 4.6 and 4.7, but the oxidation occurs mainly in the post flame zone area, in which the concentration of the radicals O and OH are sufficient for the process to occur [78]. This statement is proved by analysing figure 4.10; here it can be seen that the major concentrations of NO_x, are in the post-flame zone, and near the combustor's exit.

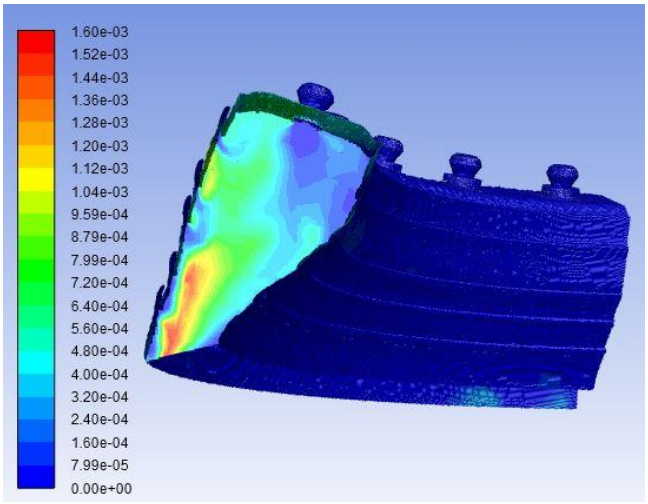

Figure 4.10 Contours of NO_x concentration [kg/kg] at 85% power, while burning Jet A.

More contours of NO_x are present in Appendix E.

4.5.2 Carbon monoxide and Unburned hydrocarbons

Carbon monoxide and unburned hydrocarbons are generally emitted in aircraft exhaust as result of incomplete combustion of jet fuel.

CO emissions are greatly related to fuel atomization, as the small fuel particles can be more easily mixed with the air, which in turn enhances combustion efficiency. *CO* are generally

formed due to the lack of oxygen to complete the reaction to CO_2, and from the dissociation of this last if the mixture present in the combustion zone is stoichiometric [1].

Unburned hydrocarbons include fuel that emerges at the combustor exit in the form of droplets or vapor, as well as the products of the thermal degradation of the parent fuel into species of lower molecular weight, such as methane and acetylene [77]. They are normally associated with poor atomization, inadequate burning rates, the chilling effects of film-cooling air, or any combination of these [77]. Increase in engine power setting usually reduces the emission of unburned hydrocarbons, partly through improved fuel atomization but mainly through the effects of higher inlet air pressure and temperature, which together enhance chemical reaction rates in the primary combustion zone [77].

As explained in the section 4.3, carbon monoxide and unburned hydrocarbons emissions indices are highest at low power settings where combustor temperatures and pressures are low, and combustion is less efficient [79].

As can be seen in figure 4.11 and 4.12, the results obtained present an irregular behaviour. The explanation for this behaviour was found in the EMICOPTER project [80]. The chemical model used was empirical, as presented in section 3.4.1. They are based on empirically determined constants along with engine specific conditions (pressures, temperatures, mass flow rates, Air-Fuel Ratio) [80]. These models are typically used for NO_x emissions and can correlate known historical NO_x emissions for a specific combustor [80]. The weakness is that it is not possible to capture consistent trades between NO_x and other pollutants (*CO*, UHC), which makes empirical models inadequate for use in designing both combustor geometries and optimal operating and flying conditions [80].

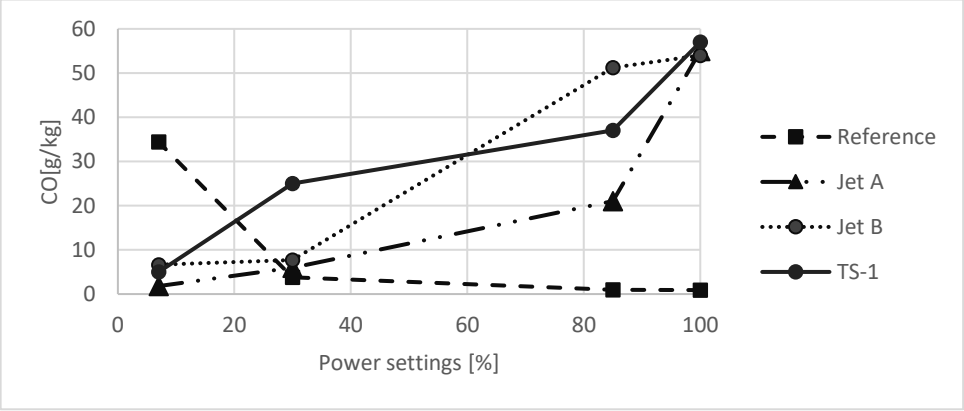

Figure 4.11 EI results of *CO*, resultant from the combustion of Jet A, Jet B and TS-1throughout ICAO's LTO cycle.

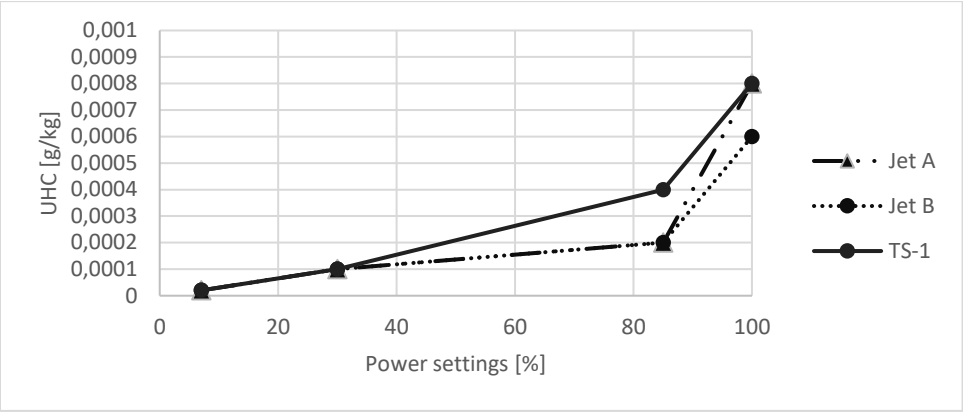

Figure 4.12 EI results of UHC, resultant from the combustion of Jet A, Jet B and TS-1, throughout ICAO's LTO cycle.

An effective approach to analyse the effect of varying operating conditions on pollutant emissions is to integrate the modelling of the combustor and gas turbine performance with a detailed model of pollutants formation [80]. Detailed models are based on the coupling detailed fluid dynamics and kinetics with the aim to describe the formation of pollutants formation during combustion [80]. Detailed models are in principle predictive numerical tools and thus do not need any tuning parameters [80].

Despite the continuous increase in computing power and speed, the direct coupling of detailed kinetics and complex CFD is a very difficult task, especially when considering the typical dimensions of the computational grids used for complex geometries and industrial applications [80].

Analysing figure 4.11, all the fuels maximum *CO* EI predicted throughout the cycle differ with the maximum reference values. Thus, all the fuels minimum *CO* EI predicted throughout the cycle differ with the minimum reference values. Still, in figure 4.11, it can be verified that Jet A presented the lowest value of EI(*CO*) at cruise, approach and idle.

Analysing figure 4.12, it can be verified that Jet B presented the lowest EI (UHC) at full power and TS-1 presented the highest EI(UHC), at cruise. Still, in figure 4.12, it can be verified that all the fuels presented the same EI(UHC) values at approach and idle.

Another weakness of the empirical model is that they do not necessarily completely capture the physics of the problem. Thus, this fact affects the prediction of the different pollutants in a specific way, being *CO* and UHC more sensitive than NO_x to turbulent mixing and fluid dynamics in general [80]. As an example, the quenching effect due to the cooling air near the walls on *CO* oxidation reactions cannot be captured with this kind of models, as can be seen in figure 4.13. *CO* emissions are, at least partially, the effect of *CO* from the primary zone being entrained in the cool air along the liner where it fails to oxidize because of the low temperatures [80].

More contours of *CO* are present in Appendix E.

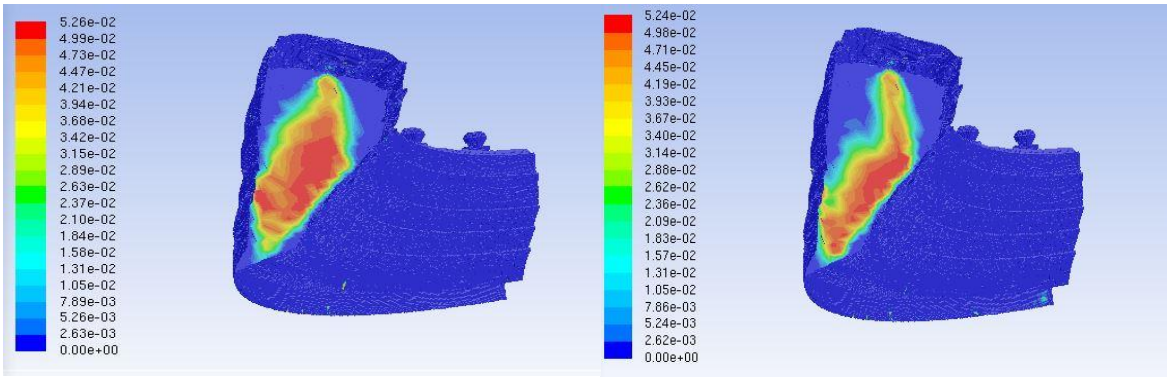

(a) (b)

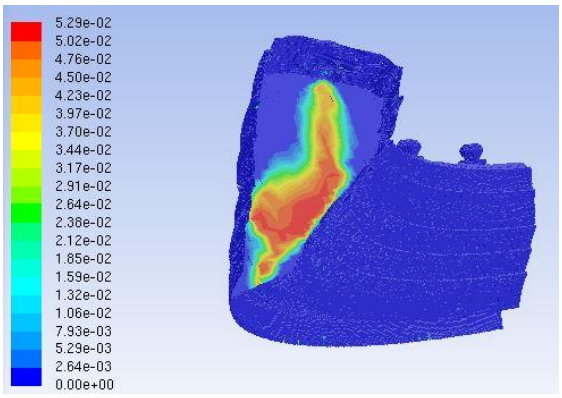

(c)

Figure 4.13 Contours of *CO* concentration [kg/kg] at full power, while burning Jet A (a), TS-1 (b), and Jet B(c).

4.5.3 Carbon dioxide

Carbon dioxide is recognised as the main greenhouse gas, has a primary role in the Earth's climate warming [16]. Typically, the EI (CO_2) from modern aircraft engines is 3160 ± 60 g/kg_{fuel} for complete combustion (e.g., Penner et al. [81]; Lee et al. [82]) [16]. However, some studies reported that EI (CO_2) decreases slightly at low thrust because incomplete combustion may result in a relative increase of *CO* and hydrocarbons in the exhaust (e.g., Anderson et al. [83]; Stettler et al. [32]) [16].

Analysing figure 4.14, it can be verified that the results agree with what was said previously, and the emission data indicate that the EI of CO_2 was the largest among the emissions considered; this behaviour is expected as CO_2 along with H_2O makes up a great part of the exhaust gases.

Still, in figure 4.14, it can be verified that TS-1 presented the lowest value of EI (CO_2) throughout the entire ICAO's LTO cycle. Jet A presented the highest values of EI (CO_2), throughout the entire ICAO's LTO cycle.

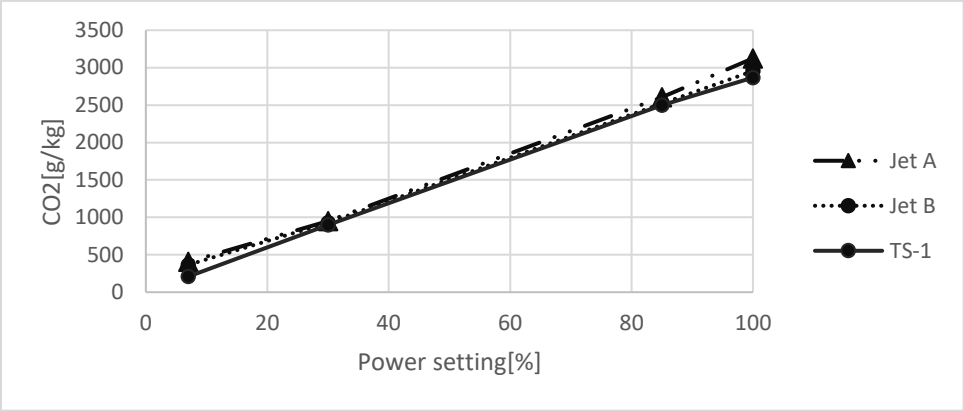

Figure 4.14 EI results of CO_2, resultant from the combustion of Jet A, Jet B and TS-1, throughout ICAO's LTO cycle.

In figure 4.15, it can be verified that CO_2 is formed mostly in the flame zone and extends to the post-flame zone, which agrees with Lieuwen et al. [58].

By comparing the CO_2 contours (figure 4.15) with the temperature contours (figure 4.6), the regions with the highest concentration of CO_2 correspond to the regions where the temperatures are higher. This behaviour is expected because the CO_2 production increases with increasing temperature, validating the simulation.

More contours of CO_2 are present in Appendix E.

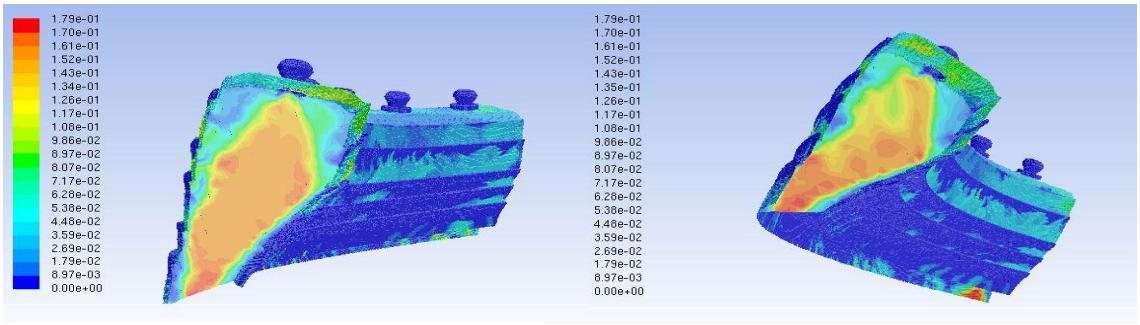

(a) (b)

Figure 4.15 Contours of CO_2 concentration [kg/kg] at full power, while burning Jet A (a) and TS-1 (b).

Chapter 5

Conclusions

Throughout the study, knowledge of combustion, thermodynamics and turbulence were acquired. It was possible to understand the combustion process and the formation of pollutants in annular chambers and to deepen the knowledge about the turbulence model used as well as the other models. In this study, knowledge about chemistry was also acquired, due to the fuels used (Jet A, Jet B and TS-1).

It was possible to increase the knowledge of the software used, such as ANSYS Fluent, which was used for the numerical study, Blender that was used to convert the STL to binary and the HELYX-OS that was used for the construction of the mesh.

Some problems were emerging throughout the work, such as the refinement of the mesh and the malfunction of the chemical model used.

Although a very refined mesh with excellent quality was obtained, a high y^+ value was obtained. This will only be overcome by refining the maximum layer creation values, but this needs more RAM available on the machine, which would lead to a higher CPU cost. Also, it is a complex geometry of the model combustor, which makes it more difficult to develop a more refined mesh.

Regarding numeric simulation, it was found divergence problems that were solved after a lot of research and an extensive trial and error approach to finding the correct solution controls. It was also necessary to calculate time step size and number of steps.

Regarding the results, the NO_x emissions represented a little margin of error from ICAO's reference values. However, in general, it was obtained a good approach to the reference values.

CO and UHC emissions exhibit erratic behaviour, and after some research was found the reason; It was due to the chemical model used. The model used was empirical. The empirical models are used for correlating experimental data on pollutant emissions in terms of all the relevant parameters. The empirical models predict NO_x emissions correctly, but the *CO* and UHC emissions they do not have a good prediction. It is because the chemical reactions governing the formation of UHC and *CO* are highly complex.

The solution found, which can be performed in future work, is to use a detailed chemical model. The EMICOPTER project developed and validated a fully approach, which integrates CFD simulations with a detailed mechanism able to predict the formation of pollutants [80].

In the doctoral thesis "Prediction of pollutants in gas turbines using Large Eddy Simulation" was developed a new methodology for the prediction with LES of NO_x and *CO* in realistic industrial configurations. This new methodology is based on a new strategy for the description of chemistry, using Analytically Reduced Chemistry (ARC) and combined with the Thickened Flame model (TFLES).

Overall, it was concluded that Jet B presented the lowest values of EI (NO_x) at take-off, approach and idle.

Jet A presented the highest values of EI (NO_x) at approach and idle.

Also, it was concluded that Jet B and TS-1 presented the lowest and highest values of EI (*CO*), respectively, at take-off and approach.

Jet A and Jet B presented the lowest and highest values of EI (*CO*), respectively, at cruise and idle.

TS-1 presented the highest values of EI(UHC) at take-off and cruise. All fuels presented the same values of EI (*UHC*) at approach and idle.

Regarding the values obtained from EI (CO_2), Jet A presented the highest values throughout the entire ICAO´s LTO cycle.

Table E.1 and E.2 (see Appendix E) summarize the main conclusions of the present work.

5.1 Future Works

CFD has a huge potential in offering solutions for problems that if were carried out experimentally, would be much more expensive and less practical in some situations.

Therefore, future developments in this area can be focused in the following items:

1. Study the correct heat transfer improving the mesh near wall.

2. Study the correct *CO* and UHC predations using detail chemical model.

3. Study different mechanisms of flame stabilization.

4. Study the influence of pressure and fuel atomization on NO_x formation.

5.Study the combustion and cooling performance in an annular combustor.

References

[1] Lefebvre, A.H. ,and Ballal, D. R. ," Gas turbine combustion" , third edition, CRC Press, Boca Raton, United States Of America, 2010.

[2] Muhammed, E., "Gas Turbine Fuels," last checked: 1.10.2019. [Online]. Available: https://prezi.com/xstmwvtocpxn/gas-turbine-fuels/. [Accessed 30 7 2019].

[3] The European Commission, "Climate change: commission proposes bringing air transport into EU emissions trading scheme," Brussels, Belgium, 2006.

[4] International Civil Aviation Organization, "Report of the independent experts on the 2006 NOx review and the establishment of medium and long term technology goals for NOx.," vol. 9, 2006.

[5] Jaravel, M. T., "Prediction Of Pollutants In Gas Turbines Using Large Eddy Simulation", PhD Dissertation, Institut National Polytechnique De Toulouse (Inp Toulouse): Doctorat De L'université De Toulousem Toulouse, France, 2016.

[6] ACARE, last checked: 1.10.2019 . [Online]. Available: http://www.acare4europe.com/. [Accessed 9 2013].

[7] Basher, A.L.M.F., "Optimum turbofan engine performance through variation of bypass ratio," *Jornal of Engineering and Development,* vol. 17, no. 1, 2013.

[8] Saravanamuttoo, H. I. H.,Rogers, G. F. C. ,and Cohen, H. , "Gas turbine theory" , fifth ed, Pearson Education, 2009.

[9] Oliveira, J. , *"CFD Analysis of the Combustion of Bio-Derived Fuels in the CFM56-3 Combustor" ,Master's Thesis,* Universidade da Beira Interior, Covilhã, Portugal, 2016.

[10] Davy, M.J.B.," Interpretative history of flight" , HM Stationery Off, 1948.

[11] Meher-Homji, C.B. , "The development of the junkers jumo 004b: The world's first production turbojet," in *ASME 1996 International Gas Turbine and Aeroengine Congress and Exhibition. American Society of Mechanical Engineers*, 1996.

[12] National Air and Space Museum, "Jumo 004B Engine," last checked: 1.10.2019. [Online]. Available: https://airandspace.si.edu/collection-objects/junkers-jumo-004-b-turbojet-engine. [Accessed 1 10 2018].

[13] General Electric, "TAPS II Combustor Final Report, Continuous Lower Energy, Emissions and Noise (CLEEN) Program," Federal Aviation Administration, 2014.

[14] Taylor, W. F. , "Aviation Fuel," Macmillan Encyclopedia of Energy, last checked: 1.10.2019 [Online]. Available: https://www.encyclopedia.com/environment/encyclopedias-almanacs-transcripts-and-maps/aviation-fuel. [Accessed 7 2 2019].

[15] Bering, R.,Buskov, K. , "Numerical Investigation of the Soot Initiated Formation of Ultra Fine Particles in a Jet Turbine Engine Using Conventional Jet Fuel," Master's Thesis, Alborg University, Aalborg, Copenhagen, Denmark 2012

[16] Masiol, M. and Harrison, R. M , "´Aircraft engine exhaust emissions and other airport-related contributions to ambient air pollution: A review'," *Atmospheric Environment*, vol. 95, pp. 409-455, May 2014.

[17] Nehru College of Aeronautics & Applied Sciences Kuniyamuthur, India, "Turbine Engine Fuel," last checked: 1.10.2019. [Online]. Available: https://sites.google.com/site/ncaaslecturenotes/gas-turbine-engine/unit-iv---fuel-systems/types-of-jet-fuel-its-characteristics. [Accessed 21 2 2019].

[18] Shell Global, "Shell Aviation Fuels," last checked: 1.10.2019 [Online]. Available: https://web.archive.org/web/20141219050306/http://www.shell.com/content/dam/shell/static/aviation/downloads/AeroShell-Book/aeroshell-book-2fuels.pdf. [Accessed 7 2 2019].

[19] Shell Global, “Civil Aviation Fuels,” last checked: 1.10.2019 [Online]. Available: https://www.shell.com/business-customers/aviation/aviation-fuel/civil-jet-fuel-grades.html. [Accessed 15 6 2019].

[20] Anderson, B.E.,Chen, G., Blake, D.R. , “Hydrocarbon emissions from a modern,” *Atmos. Environ,* vol. 40,no. 19, pp. 3601- 3612, 2006.

[21] Kinsey, J.S.,Hays, M.D., Dong, Y.,Williams, D.C.,Logan, R. , “Chemical characterization of the fine particle emissions from commercial aircraft engines during the Aircraft Particle Emissions eXperiment (APEX) 1 to 3.,” *Environ. Sci. Technol.,* vol. 45,no.8, p. 3415-3421.

[22] Kinsey, J.S., Dong, Y.,Williams, D.C.,Logan, R., “Physical characterization of the fine particle emissions from commercial aircraft engines during the aircraft particle emissions experiment (APEX) 1 to 3.,” *Atmos. Environ.,* vol. 44, p. 2147-2156., 2010.

[23] Timko, M.T., Onasch, T.B., Northway, M.J., Jayne, J.T., Canagaratna, M.R., Herndon, S.C., Wood,E.C., Miake-Lye, M.C., Knighton, W.B., “Gas turbine engine Emissions Part II: chemical properties of particulate matter.,” *J. Eng. Gas Turbines Power,* vol. 132, 2010.

[24] Whitefield, P.D., Lobo, P., Hagen, D.E.; Timko, M.T., Miake-Lye, R.C., Taylo, C., Ratliff G.,Lukachko, S., Sequeira, C., Hileman, J., Waitz, I., Webb, S., Thrasher, T.G., Ohsfeldt, M.R., Kaing,H. K., Essama, S.C., Summarizing and Interpreting Aircraft Gaseous and Particulate Emissions Data.ACRP Report 9., Washington, D.C.: Transportation Research Board, 2008.

[25] Lobo, P., Whitefield, P.D., Hagen, D.E., Herndon, S.C., Jayne, J.T., Wood, E C., Knighton, W.B.,Northway M.J., Miake-Lye R.C., Cocker D., Sawant A., Agrawal H., Miller J.W., The Development of Exhaust Speciation Profiles for Commercial Jet Engines, Final Report. Contract No. 04-344., Sacramento, CA.: California Air Resources Board, 2007.

[26] Onasch, T.B.,Jayne, J.T.,Herndon, S.,Worsnop, D.R.,Miake-Lye, R.C.,Mortimer, I.P. , “Chemical properties of aircraft engine particulate exhaust emissions.,” *J.Propul . Power,* vol. 25,no.5, pp. 1121- 1137, 2009.

[27] Chester, W. S., Michael, W. H.,Deborah. L. S.,David, P. H.,Mark, D. S. , “Chemical Composition of Exhaust from Aircraft Turbine Engines,” *Journal of Engineering: Gas Turb.Power* , vol. 114, no.1, pp. 111-115, 1992.

[28] Spicer, C.W.,Holdren, M.W.,Riggin, R.M.,Lyon, T.F., “Chemical composition and photochemical reactivity of exhaust from aircraft turbine engines,” *Geophys,* vol. 12, 1994.

[29] Patterson, J.,Noel, G.J.,Senzig, D.A., Roof, C.J., Fleming, G.G. , “Analysis of departure and arrival profiles using real-time aircraft data,” *J. Aircraft* , vol. 46,no.4, pp. 1094-1103, 2009.

[30] Khadilkar, H.,Balakrishnan, H. , “Estimation of aircraft taxi fuel burn using flight data 3078 recorder archives.Transport.,” *Res. Part D* ,vol.17, no.7, p. 532–537, 2012.

[31] Unique, “Aircraft NOx-Emissions within the Operational LTO Cycle,” 2004. [Online]. Available: http://www.zurich-airport.com/Portaldata/2/Resources/documents_unternehmen/umwelt_und_laerm/Technical_Report_Operational_Aircraft_Emissions_2004.pdf. [Accessed 8 2013].

[32] Stettler, M.E.J, Eastham, S., Barrett, S.R.H., “Air quality and public health impacts of UK airports. Part I: emissions.,” *Atmos. Environ.,* vol. 45, no.31,p. 5415–5424, 2011.

[33] Carslaw, D.C., Ropkins, K., Laxen, D.,Moorcroft, S. ,Marner, B.,Williams, M.L., “Nearfield commercial aircraft contribution to nitrogen oxides by engine, aircraft typ, and airline by individual plume sampling,” *Environmental Science and Tecnology,* vol. 42, no.6, pp. 1871-1876, 2008.

[34] Heland, J., Shafer, K.,, “Determination of major combustion products in aircraft products in aircraft exhausts by FTIR emission spectroscopy,” *Atmos. Environ.,* no. 32, pp. 3067-3072, 1998.

[35] Herndon, S.C., Jayne, J.T., Lobo, P., Onasch, T.B., Fleming, G., Hagen, D.E., Whitefield, P.D.,Miake-Lye, R.C., "Commercial aircraft engine emissions characterization of in-use aircraft at Hartsfield–Jackson Atlanta International Airport.," *Environ. Sci. Technol.,* vol. 42, no. 6, pp. 1877-1883, 2008.

[36] Starik, A. M., Lebedev, A.B., Savel'ev, A. M., Titova, N. S. ,and Leyland, P., "Impact of Operating Regime on Aviation Engine Emissions: Modeling Study," *Journal of Propulsion and Power,* vol. 29, no. 3, pp. 709-717, 2013.

[37] Mueller, M.E. ,and Pits, H. , "Large eddy simulation of soot evolution in an aircraft combustor," *Physis of Fluids,* vol. 25, no. 11, p. 110812, 2013.

[38] Mueller, M.E.,Blanquart, G. ,and Pitsch, H., "A joint volume -surface model of soot aggregation with the method of moments," *Proceedings of the Combustion Institute,* vol. 32, no. 1, p. 785—792, 2009.

[39] Martins, D., "Off-Design Performance Prediction of the CFM56-3 Aircraft", Master's Thesis, Lisboa: Instituto Superior Técnico,Lisboa, Portugal 2015.

[40] CFM, "CFM56-3 Basic Engine" *, B737-300. Formação Profissional TAP,* Revision 3, 1992.

[41] Aircraft Owners & Operator Guide , "CFM56-3 maintenance analysis & budget," *Aircraft Commerce,* no. 45, Apr/May 2006.

[42] Aubuchon, D.,Campbell, J., "CFM56-3 Turbofan Engine Description," Seneca College,Toronto, Canada, 2006.

[43] NPTEL, "Aircraft Engines and Propulsion System," last checked: 1.10.2019. [Online]. Available: https://nptel.ac.in/courses/112104117/chapter_5/4_31.html. [Accessed 1 2 2019].

[44] Rolls-Royce," The Jet Engine", 5th edition, England: The Technical Publications Department, Rolls- Royce plc, Derby, England.

[45] Smith, I. E. , "Combustion in Advanced Gas Turbine Systems," in *roceedings of an International Propulsion Symposium Held at the College of Aeronautics*, Cranfield,England, April 1967.

[46] Sethi, V. , " Introduction to design consideration and sizing methodologies in GTC´s ", in *Gas Turbine Combustion*, Cranfield University , short course, 2015.

[47] Queirós, P ., "Atomização e Combustão de Glicerina" Master's thesis, Instituto Superior Técnico, Lisboa ,Lisboa, Portugal, 2011.

[48] Kruger, S. , ""Hazardous area classification: liquid dispersion"," EE Publisher, last checked: 1.10.2019. [Online]. Available: http://www.ee.co.za/article/hazardous-area-classification-liquiddispersion. [Accessed 30 1 2019].

[49] Lefebvre, A. H. , "Atomization and sprays," *CRC press,* vol. 1040, no. 2756, 1988.

[50] Francis, R., "Investigation of Fuel Nozzle Technologies To Reduce Gas Turbine Emissions", University of Toronto, Toronto, Canada, 2015.

[51] Flagan, R.C. ,and Seinfeld, J.H. , "Fundamentals of air pollution engineering," *Courier Corporation,* NY, USA, 2013.

[52] Turns , S.R. , "An Introduction to combustion," *McGraw-hill New York,* vol. 287, 1996.

[53] Spakovszky, Z. S., "Adiabatic Flame Temperature," last checked: 1.10.2019 [Online]. Available: http://web.mit.edu/16.unified/www/SPRING/propulsion/notes/node111.html. [Accessed 4 2 2019].

[54] Waitz, I. A.,Gauba, G. ,and Tzeng, Y.S., "Combustors for micro-gas turbine engines," *Journal of Fluids Engineering,* vol. 120, no. 1, pp. 109-117, 1998.

[55] ICAO(International Civil Organization), "Environmental Protection (Annex 16)," in *Aircraft Engine Emission*, vol. 2, International Standards and Recommended Practises, ISBN 978-92-9231-123-0, 2008.

[56] ICAO, ""ICAO engine exhaust emissions data bank" CFM56-3-B1," *Tech. Rep.,* 2013.

[57] Nascimento, D. , Desenvolvimento de uma Câmara de Combustão para uma Turbina a Gás,Master's thesi, Instituto Superior Técnico, Lisboa ,Portugal, 2015.

[58] Lieuwen , T.C. ,and Yang, V. , “Gas turbine emissions,” *Cambridge University Press,* vol. 38, 2013.

[59] ANSYS, A. F., “ANSYS FLUENT 12.0/12.1 Documentation,” ANSYS, Inc, 2009.

[60] Fenimore, C. P. , “Formation of Nitric Oxide in Premixed Hydrocarbon Flames.,” in *13th Symp. (Int'l.) on Combustion*, The Combustion Institute, vol.13, no.1, 1971.

[61] Blakey, S., Rye, L., and Wilson, C. W., “Aviation gas turbine alternative fuels: A review,” *Proceedings of the Combustion Institute,* vol. 33, no.2, 2010.

[62] Goodger, E. M. , Transport Fuels Technology, Norwich, UK: Landfall Press, 2000.

[63] Fernández, J. M. I., “Study of Combustion Using a Computational Fluid Dynamics Software (ANSYS),” Universitat de Barcelona, Barcelona, Spain, 2015.

[64] Moreira, P., Influência do ângulo de injeção nas emissões de poluentes e temperatura de combustão, Master's Thesis, Universidade da Beira Interior, Covilhã,Portugal, 2016.

[65] Shih, T. H.,Liou, W. W.,Shabbir, A.,Yang, Z. ,and Zhu, J. , in *A New k- e Eddy-Viscosity Model for High Reynolds Number Turbulent Flows - Model Development and Validation.*, vol.24, no.3, 1995.

[66] Wilcox, D. C. , Turbulence Modeling for CFD, California: DCW Industries, Inc., La Canada, California,1998

[67] Menter, F. R. , “Two-Equation Eddy-Viscosity Turbulence Models for Engineering Applications.,” *AIAA Journal,* vol. 32, no. 8, August 1994.

[68] Walters, D. K. ,and Cokljat, D. , “A three-equation eddy-viscosity model for reynolds-averaged navier-stokes simulations of transitional flows.,” *Journal of Fluids Engineering,* vol. 130, December 2008.

[69] Mercier, R., "Turbulent combustion modeling for Large Eddy Simulation of non-adiabatic stratified flames", Master´s thesis, École Centrale Paris,Paris , France, 2015.

[70] Chatterjee, P., " A computational fluid dynamic investigation of thermoacustic instabilities is premixed laminar and turbulent combustion systems", Ph.D. dissertation, Virginia Polytechic Institute and State University, Virginia, USA, 2004.

[71] Ribeiro, P., “Análise de performance da Família de Motores de Avião CFM56,” *Master´s thesis, Instituto Superior de Engenharia de Lisboa,* Lisboa, Portugal2012.

[72] Jones, B. , “Gas turbine combustor, design and development,” in *Gas Turbine Combustion*, Cranfield University, short course, 2015,

[73] Menter, F.R. ,and ANSYS Germany GmbH, "Best Practice: Scale-Resolving Simulations in ANSYS CFD Version 1.0" , Ansys inc., 2012.

[74] Noor, M.,Wandel A. P.,and Yusaf, T. , “Detail guide for CFD on the simulation of biogas combustion in bluff-body mild burner,” in *Proceedings of the 2nd International Conference of Mechanical Engineering Research (ICMER 2013)*, Universiti Malaysia Pahang, Malaysia, 2013.

[75] Salim, M. , and Cheah, S.C. , “Wall y+ Strategy for Dealing with Wall-bounded Turbulent Flows,” in *Conference: International MultiConference of Engineers and Computer Scientists,IMECS*, vol.2, March 2009.

[76] Gerasimov, A. , "Modeling Turbulent Flows with FLUENT", Europe: ANSYS,lnc., 2006.

[77] Reeves, C.M.,and Lefebvre, A.H. , “Fuel Effects on Aircraft Combustor Emissions,” in *The American Society Of Mechanical Engineers*, New York, N.Y., 1986.

[78] Zeldovich, Y. B. , “The oxidation of nitrogen in combustion and,” *Acta Physicochim.URSS,* vol. 21, no. 4, 1946.

[79] Sutkus, D.J.Jr.,Baughcum, S.L.,DuBois, D.P. , Scheduled Civil Aircraft Emission Inventories for 1999: Database Dev. and Anal. NASA/CRm2001-211216., 2001.

[80] The European Commission, “Emicopter report summary,” last checked: 1.10.2019. [Online]. Available: http://cordis.europa.eu/result/rcn/143538_en.html . [Accessed 24 6 2019].

[81] Penner, J.E., Lister, D.H., Griggs, D.J., Dokken, D.J., McFarland, M., (Eds), Aviation and the Global Atmosphere, Chapter 7, Special Report of the Intergovernmental Panel on Climate Change, Cambridge University Press: Cambridge, England, 1999.

[82] Lee, D.S.,Pitari, G.,Grewe, V.,Gierens, K.,Penner, J.E.,Petzold, A.,Prather, M.J.,Schumann, U.,Bais, A.,Berntsen, T.,Iachetti, D.,Lim, L. L.,Sausen, R., "Transport impacts on atmosphere and climate: Aviation," *Atmos. Environ,* no. 44, p. 4678–4734, 2010.

[83] Wey,C.C.,Anderson,B.E.,Hudgins,C.H.,Wey, C.,Li-Jones, X.,Winstead,E.,Thornhill,L.,Lobo,P.,Hagen,D.,Whitefield,P.D.,Yelvington,P.E.,Herndon,S.C.,Onasch,T.B.,Miake-Lye,R.C.,Wormhoudt,J.,Knighton,B.,Howard,R.,Bryant,D.,Corporan,E.,Moses,C.,Holve,D.,Dodds,W.,, "Aircraft Particle Emissions eXperiment (APEX)," NASA/TM-2006-214382, 2006,ARL-TR-3903, 2006.

[84] Heland, J. ,and Schafer, K., "Analysis of aircraft exhausts with Fourier-transform infrared emission spectroscopy," *Appl. Optics,* vol. 36, no. 21, pp. 4922-4931, 1997.

[85] Popp, P.J., Bishop, G.A., Stedman, D.H., "Method for commercial aircraft nitric oxide emission meaurements.," *Environ. Sci. Technol.,* vol. 33, no.9, pp. 1542-1544, 1999.

[86] Herndon, S.C., Shorter, J.H., Zahniser, M.S., Nelson, D.D. Jr., Jayne, J., Brown, R.C., Miake-Lye, R.C., Waitz, I., Silva, P., Lanni, T., Demerjian, K., Kolb, C.E., "NO and NO2 emission ratios measured from in-use commercial aircraft during taxi and take-off.," *Environ. Sci. Tenhnol.,* no. 38, pp. 6078-6084, 2004.

[87] Herndon, S.C., Onasch, T.B., Frank, B.P., Marr, L.C., Jayne, J.T., Canagaratna, M.R., Grygas, J.,Lanni, T., Anderson, B.E., Worsnop, D., Miake-Lye R.C. , "Particulate emissions from in -use commercial aircraft.," *Aerosol Sci. Technol.,* vol. 39,no.8, pp. 799-809, 2005.

[88] Zhu, Y.,Fanning, E.,Yu, R.C.,Zhang, Q.,Froines, J.R., "Aircraft emissions and local air quality impacts from takeoff activities at a latge International Airport," *Atmos. Environ.,* vol. 45, no.36,p. 6526-6533, 2011.

[89] Fanning, E.,Yu, R.C., Lu, R.,Froines, J. , "Monitoring and Modeling of Ultrafine Particles and Black Carbon at the Los Angeles International Airport. Final Report.," *California Air Resource Board Contract,* pp. 04-325, 2007.

[90] Schummann, U. , "Formation, properties and climatic effects of contrails," *C.R. Physique,* vol. 6, no. 4/5, pp. 549-565, 2005.

[91] Herndon, S.C., Wood, E.C., Northway, M.J., Miake-Lye, R., Thornhill, L., Beyersdorf, A.,Anderson, B.E., Dowlin, R., Dodds, W., Knighton, W.B. , "Aircraft hydrocarbon emissions at Oakland international airport," *Environ. Sci. Technol,* vol. 43, no. 6, pp. 1730-1736, 2009.

[92] Klapmeyer, M.E. ,and Marr, L.C., "NOx and Particle Emissions from Aircraft and Support Activities at a Regional Airport," *Environ. Sci. Technol.,* vol. 46,no.20, pp. 10974-10981, 2012.

[93] Lobo, P.,Hagen, D.E. ,and Whitefield, P.D., "Measurement and analysis of aircraft engine PM emissions downwind of an active runway at the Oakland International Airport.," *Atmos. Environ.,* vol. 61, pp. 114-123, 2012.

[94] EASA TYPE-CERTIFICATE DATA SHEET, European Aviation Safety Agency, 2008.

[95] EUROCONTROL, last checked: 1.10.2019. [Online]. Available: https://ansperformance.eu/acronym/lto/. [Accessed 15 6 2019].

[96] GE Aviation , "The GEnx Commercial Aircraft Engine," last checked: 1.10.2019. [Online]. Available: https://www.geaviation.com/commercial/engines/genx-engine. [Accessed 30 1 2019].

[97] Hinze, J. O. , "Turbulence", New York: McGraw-Hill Publishing Co., 1975.

[98] Malalasekera, W.,Ibrahim, S.S.,Masri , A.R.,Gubba, S. R.,Sadasivuni, S. K. , "Large eddy simulation of premixed and non-premixed combustion," in *Proceedings of the 37th National & 4th International Conference on Fluid Mechanics and Fluid Power*, IIT Madras, Chennai, India, 2010.

[99] International Civil Aviation Organization, "Airport Air Quality," last checked: 1.10.2019 [Online]. Available: https://www.icao.int/publications/Documents/9889_cons_en.pdf . [Accessed 10 8 2019].

[100] Spakovszky, Z. S. , “Thermodynamics and Propulsion,” last checked: 1.10.2019 [Online]. Available: https://web.mit.edu/16.unified/www/SPRING/propulsion/notes/node27.html. [Accessed 13 9 2019].

Appendix A

A. Jet Fuel Properties

Table A.1 Some specification properties of Jet A and Jet A-1.

Property	Jet A	Jet A-1
Approximate formula[21]	$C_{11}H_{21}$	$C_{11}H_{21}$
H/C ratio	1.91	1.91
Boiling range, (℃)	165-265	165-265
Freeze Point, max, (℃)	-40	-47
Flash Point, min, (℃)	38	38
Net heat of combustion, max, (MJ/kg)	43.15	43.15
Density, 15℃, (Kg/m^3)	775-840	775-840
Viscosity, -20℃, max, (mm^2/s)	8	8
Critical pressure, (atm)	23	23
Smoke point, min, (mm)	18	19

[21] For illustration of average carbon number, not designed to give accurate H/C ratios [1].

Appendix B

B. Bibliographic Review

Table B.1 List of recent studies available in the literature reporting EIs during real aircraft operation [16].

Target; Period; Airport	Analyzed compounds	Sampling; Analytical		Engine thrusts (if know) or LTO phases	References
In service military and civil aircraft at various airports	CO_2, H_2O, CO, NO, N_2O	Measurements performed at distances of 20-40 m to the nozzle exit perpendicular to the exhaust flow via ground-based FTIR analysis		Various thrusts	[34] [84]
Various (90) in service aircraft: from gulfstream executive jets to Boeing 747-400s at London Heathrow Airport (UK)	$CO_2, CO, NO,$ hydrocarbons	The remote sensor positioned at ground level. Experimental: non-dispersive IR spectroscopy, dispersive UV spectrometer		Mix of idle, taxi-out and take-off modes	[85]
30 individual planes, ranging from TP to jumbo jets; August 2001; J.F. Kennedy Airport (USA)	CO_2, NO, NO_2	Measurements within 350 m of a taxiway and 550 m of a runway. Experimental: automatic (IR), TILDAS		Taxiway thrust and take-offs	[86]
In-use commercial aircraft; period: 2001-2003; Airports: J.F. Kennedy airport in New York City and Logan airport in Boston (USA)	Particulate matter, number concentration and size distributions	Extractive sampling of the advected plumes of aircraft using a novel approach, 200 m of an active taxiway and runway. Experimental: ELPI, CPC		Several different types of plumes were sampled, including approach (landing) and engine start-up in addition to idle, taxi, and take-off	[87]

Table B.1 List of recent studies available in the literature reporting EIs during real aircraft operation (continuation) [16].

Target; Period; Airport	**Analyzed compounds**	**Sampling; Analytical**	**Engine thrusts (if know) or LTO phases**	**References**
Real time data at Los Angeles International Airport (USA); Period: September 23-29, 2005	UFPs (diameter <100 nm), black carbon, PM2.5 mass, and chemical species (PAHs, butadiene, benzene, acrolein, formaldehyde)	At blast fence (140 m from the take-off) and five downwind sites up to 600 m from the take-off runway. Experimental: SMPS (DMA/CPC), aethalometers, E-BAM, automatic PAHs analyzer, canister, cartridge	-	[88] [89]
Impact of airport emissions at Zurich-Kloten airport (Switzerland); Period: June 2004 to July 2004	$NO, NO_2, CO, CO_2, VOCs$	Measurements with in-situ and open-path devices; COV samples taken directly within the plume of the engine, about 50–100m behind an aircraft, at a height of 1m. Experimental: FTIR; DOAS; canister [GC/FID]	-	[90]

Table B.1 List of recent studies available in the literature reporting EIs during real aircraft operation (continuation) [16].

Target; Period; Airport	**Analyzed compounds**	**Sampling; Analytical**	**Engine thrusts (if know) or LTO phases**	**References**
In-use commercial airfreight and general aviation at Oakland International Airport (USA); Period: August 20-29, 2005;	Formaldehyde, acetaldehyde, ethene, propene, and benzene	At the end of an active taxiway next to the main runway. Data collected on an ambient sampling manifold consisting of a 3.8 cm diameter tube, ~7 m long drawing ~150 slpm. Experimental: TILDAS; proton transfer reaction mass spectrometer measurements	Idle (taxiway/runway)	JETS/APEX-2 campaign; [91]
Emission of Roanoke Regional Airport in Virginia (USA); Period: July 2011 - February 2012	CO_2, NOx, particle number, BC	A mobile eddy covariance laboratory with a mast extending nearly 15 m above ground level and placed near active runways. Experimental: automatic devices, CPC, aethalometer	Idle/taxi and take-off	[92]
Real-time measurements of aircraft engine specific emissions at Oakland International Airport (USA); Period: August 26, 2005	CO_2, particle number concentration, size distributions, PM mass	100-300 m downwind of an active taxi-/runway. Experimental: Automatic IR, Cambustion DMS500, CPC, SMPS, MAAP	Normal LTO operations	[93]

Appendix C

C. Specifications of CFM56-3 engine

Table C.1 Specifications of CFM56-3 engine [94].

Engine	CFM56-3
Type	Dual rotor, axial flow, high bypass ratio turbofan
Compressor	1 fan, 3 LP, 9 HP
Combustor	annular
Turbine	1 HP, 4 LP
Control	hydro-mechanical + limited electronic
Length, cm	236.4
Width, cm	201.8
Height, cm	181.7
Dry weight, kg	1.954–1.966
Bypass ratio	5.9-6.0

Appendix D

D. Problem Set up inputs

Table D.1 Fuel stoichiometric ratios, flash point and LHV for the fuels in study [1] [9].

Jet Fuel	Jet A /Jet A-1	Jet B	TS-1
Stoichiometric AFR	14.7	14.9	14.7
Stoichiometric FAR	0.0680	0.0667	0.0680
FSRFL	0.0740	0.07338	0.0740
Flashpoint (K)	312	250.15	301.15
LHV (MJ/kg)	43.15	43.15	43.2

Table D.2 Oxidizer and temperature species model inputs values.

Power (%)	100	85	30	7
Oxidizer Temperature (K)	743.91	674.25	418.82	311.15
Operating Pressure (kPa)	2343.346	1981.730	655.804	101.325

Table D.3 Relevant data for the CFM56-3, obtained from Ribeiro´s work [71].

Station	$\dot{m}_{total}(\frac{kg}{s})$	$\dot{m}_{1/4}(\frac{kg}{s})$	$T(K)$	$P(kPa)$
Fan	314.82	---	288.15	101.325
HPC exit	51.52	12.86	743.91	2343.346
Combustor entry	51.51	10.36	743.91	2343.346
Combustor exit	42.58	10.64	1649.94	2226.179
HPT entry	45.727	11.432	1593.23	2226.179

Table D.4 Solution control parameters for flow courant number, explicit relaxation factor (ERF) and under- relaxation factor (URF), used in RANS simulation.

Parameters	Original value	New value
Flow Courant Number	200	1
ERF: Momentum	0.75	0.3
ERF: Pressure	0.75	0.3
URF: Density	1	0.3
URF: Body Force	1	0.5
URF: Turbulent Kinetic Energy	1	0.4
URF: Turbulent Dissipation Rate	1	0.4
URF: Turbulent Viscosity	1	0.4
URF: Reynolds Stresses	1	0.4
URF: Pollutant NO	0.9	0.6
URF: Energy	1	0.3
URF: Temperature	1	0.3
URF: Discrete Ordinates	1	1
URF: Mean Mixture Fraction	1	0.6
URF: Misture Fraction Variance	1	0.6
URF:Discrete Phase Sources	0.5	0.5

Table D.5 Solution method parameter setting, used in RANS simulation.

Parameters	Original	New setting
Pressure-Velocity Coupling	SIMPLE	Coupled
Gradient	Green-Gauss Cell Based	Least Square Cell Based
Pressure	Standard	PRESTO!
Momentum	First Order Upwind	Second Order Upwind
Turbulent Kinetic Energy	First Order Upwind	Second Order Upwind
Turbulent Dissipation Rate	First Order Upwind	Second Order Upwind
Reynolds Stresses	First Order Upwind	Second Order Upwind
Pollutant no	First Order Upwind	Second Order Upwind
Energy	First Order Upwind	Second Order Upwind
Discrete Ordinates	First Order Upwind	Second Order Upwind
Mean Mixture Fraction	First Order Upwind	Second Order Upwind
Misture Fraction Variance	First Order Upwind	Second Order Upwind

Table D.6 Mass flow inlet (kg/s) for each boundary, at its respective power setting, while burning TS-1.

Boundary condition	Name	Air mass flow (kg/s) to each Fuel Power (%)				Cooling air flow (%)
		100	85	30	7	
Mass flow inlet	Domes holes 1	0.0124	0.0129	0.0090	0.0026	0.1851
Mass flow inlet	Dil.1.1	1.4688	1.5313	1.0711	0.3034	21.9534
Mass flow inlet	Dil.2	2.9375	3.0626	2.1421	0.6067	43.9068
Mass flow inlet	Dil.2.1	1.6646	1.7355	1.2139	0.3438	24.8805
Mass flow inlet	Mix	0.2938	0.3063	0.2142	0.0607	4.3907
Mass flow inlet	Mix 2	0.2938	0.3063	0.2142	0.0607	4.3907
Mass flow inlet	Mix 3.1	0.0048	0.0051	0.0036	0.0010	0.0732
Mass flow inlet	Mix 3.2	0.0048	0.0051	0.0036	0.0010	0.0732
Mass flow inlet	Mix 4	0.0098	0.0102	0.0071	0.0020	0.1464
Mass flow inlet	Swirler	1.7015	1.4524	0.5101	0.1191	---
Mass flow inlet	Swirler 2	1.7015	1.4524	0.5101	0.1191	---
Mass flow inlet	Fuel inj.	0.1815	0.15492	0.0544	0.0127	---
Mass flow inlet	Fuel. Inj. rich	0.0500	0.03912	0.0150	0.0035	---
	Total $\dot{m}_a$	10.0934	9.8800	5.899	1.6200	---
	Total cooling $\dot{m}_a$	6.6904	6.9752	4.8788	1.3818	≈ 100
	Fuel flow ($\dot{m}_f$)	0.2315	0.1976	0.0694	0.0162	
	Overall AFR	43.6	50	85	100	
	PZ AFR	14.7				

Table D.7 Mass flow inlet (kg/s) for each boundary, at its respective power setting, while burning Jet B.

Boundary condition	Name	Air mass flow (kg/s) to each Fuel Power (%)				Cooling air flow (%)
		100	85	30	7	
Mass flow inlet	Domes holes 1	0.0123	0.0128	0.00903	0.0026	0.1851
Mass flow inlet	Dil.1.1	1.4617	1.5196	1.0711	0.3027	21.9534
Mass flow inlet	Dil.2	2.9235	3.0391	2.1422	0.6053	43.9068
Mass flow inlet	Dil.2.1	1.6566	1.7222	1.2139	0.3430	24.8805
Mass flow inlet	Mix	0.2924	0.3039	0.2142	0.0605	4.3907
Mass flow inlet	Mix 2	0.2924	0.3039	0.2142	0.0605	4.3907
Mass flow inlet	Mix 3.1	0.0049	0.0051	0.0036	0.0010	0.0732
Mass flow inlet	Mix 3.2	0.0049	0.0051	0.0036	0.0010	0.0732
Mass flow inlet	Mix 4	0.0097	0.0100	0.0071	0.0020	0.1464
Mass flow inlet	Swirler	1.7284	1.4691	0.51852	0.1207	---
Mass flow inlet	Swirler 2	1.7284	1.4691	0.51852	0.1207	---
Mass flow inlet	Fuel inj.	0.1819	0.15460	0.05457	0.01270	---
Mass flow inlet	Fuel. Inj. rich	0.05011	0.04260	0.01503	0.0035	---
	Total $\dot{m}_a$	10.1152	9.8600	5.9160	1.6200	--
	Total cooling $\dot{m}_a$	6.6584	6.9218	4.8789	1.3786	$\approx \mathbf{100}$
	Fuel flow ($\dot{m}_f$)	0.2320	0.1972	0.0696	0.0162	
	Overall AFR	43.6	50	85	100	
	PZ AFR	**14.9**				

Appendix E

E. Additional results

E.1 Resume of the results

Table E.1 Fuel that presents the highest EI value for each pollutant in each mode of engine operation.

Mode / EI(g/kg)	Take- off	Cruise	Approach	Idle
NO_x	TS-1 (18.2)	Jet B (10)	Jet A (0.33)	Jet A (0.02)
CO	TS-1 (57)	Jet B (51.23)	TS -1 (25)	Jet B (6.65)
UHC	Jet A and TS-1 (0.0008)	TS-1 (0.0004)	All the jet fuels present the same value (0.0001)	All the jet fuels present the same value (0.00002)
CO_2	Jet A (3124.3)	Jet A (2604.81)	Jet A (951.46)	Jet A (404.97)

Table E.2 Fuel that presents the lowest EI value for each pollutant in each mode of engine operation.

Mode / EI(g/kg)	Take- off	Cruise	Approach	Idle
NO_x	Jet B (17.5)	Jet A (9)	Jet B (0.23)	Jet B and TS-1 (0.01)
CO	Jet B (54)	Jet A (21.03)	Jet A (6)	Jet A (1.81)
UHC	Jet B (0.0006)	Jet A and Jet B (0.0002)	All the jet fuels present the same value (0.0001)	All the jet fuels present the same value (0.00002)
CO_2	TS-1 (2867)	TS-1 (2500)	TS-1 (899)	TS-1 (209)

E.2 CO_2 emissions

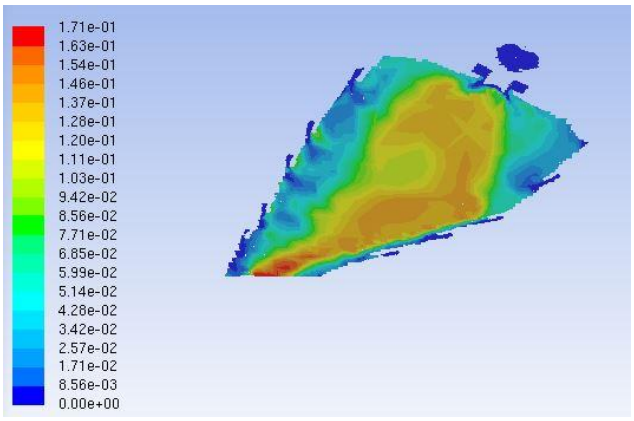

Figure E.1 Cross section contours of CO_2 concentration [kg/kg] at full power, while burning Jet B.

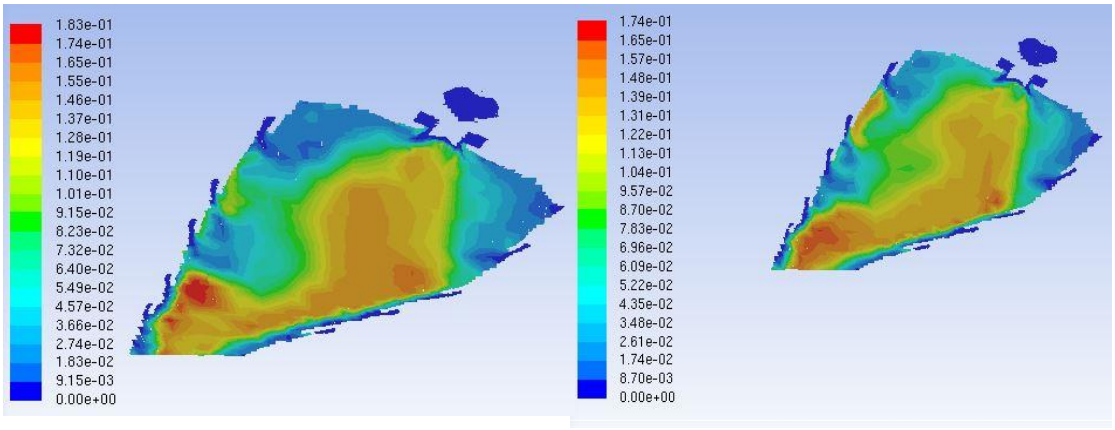

(a) (b)

Figure E.2 Cross section contours of CO_2 concentration [kg/kg] at 85% power, while burning TS-1 (a) and Jet B (b).

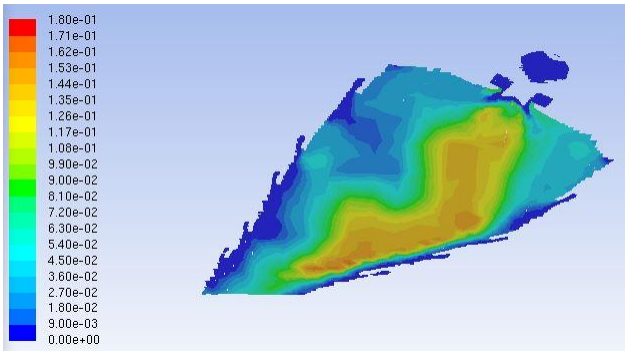

Figure E.3 Cross section contours of CO_2 concentration [kg/kg] at 30% power, while burning Jet B.

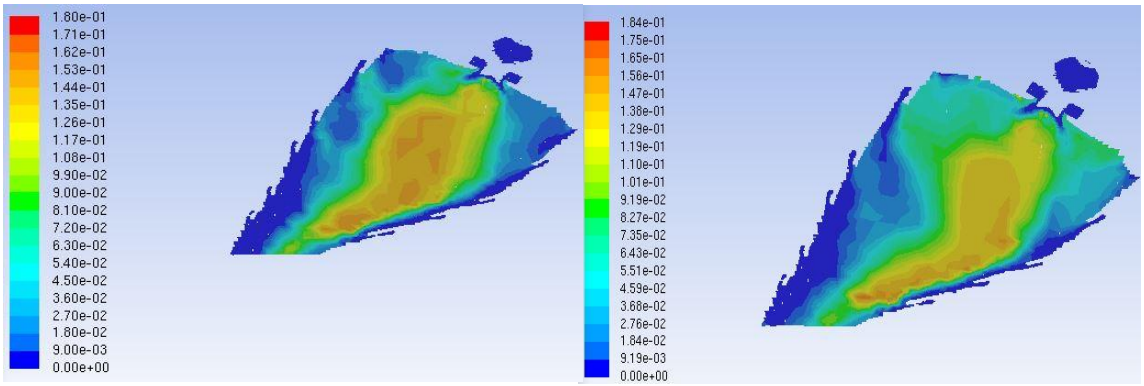

(a) (b)

Figure E.4 Cross section contours of CO_2 concentration [kg/kg] at 7% power, while burning, TS-1 (a) and Jet B (b).

E.3 *CO* emissions

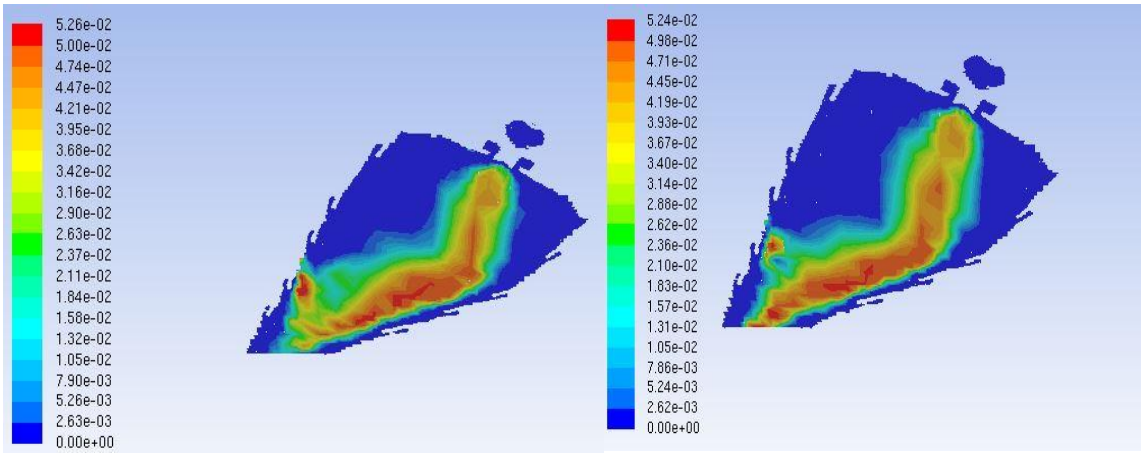

(a) **(b)**

Figure E.5 Cross section contours of *CO* concentration [kg/kg] at 85% power, while burning Jet B(a) and Jet A (b).

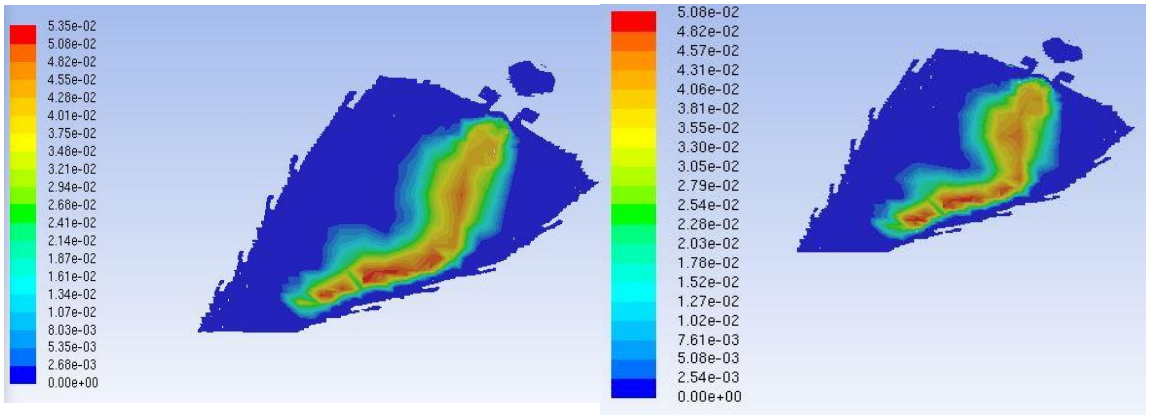

(a) (b)

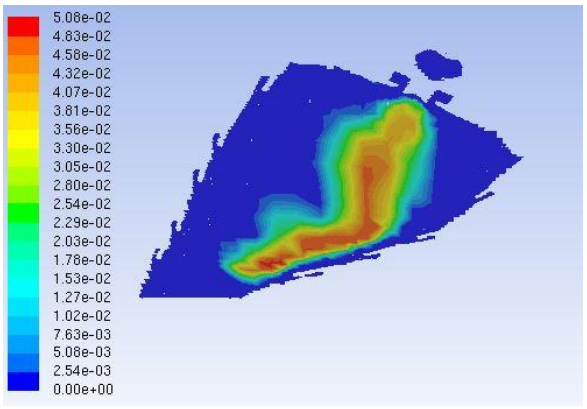

(c)

Figure E.6 Cross section contours of *CO* concentration [kg/kg] at 30% power, while burning Jet B (a), Jet A(b) and TS-1 (c).

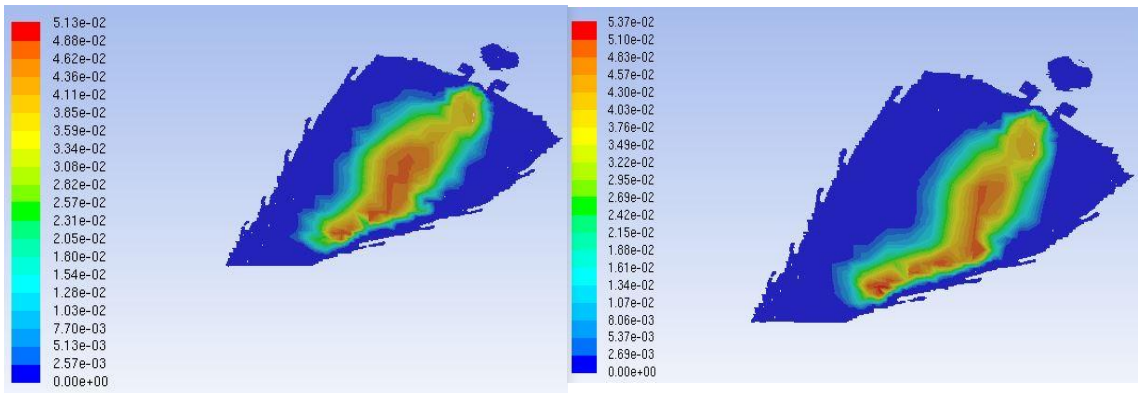

(a) (b)

Figure E.7 Cross section contours of *CO* concentration [kg/kg] at 7% power, while burning TS-1 (a) and Jet B (b).

E.4 NO_x emissions

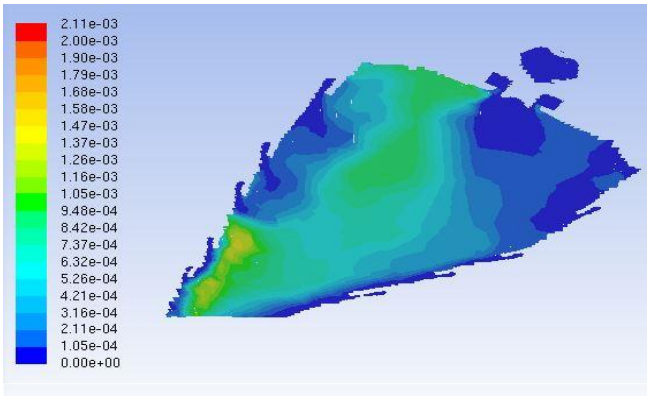

Figure E.8 Cross section contours of NO_x concentration [kg/kg] at 85% power, while burning Jet B.

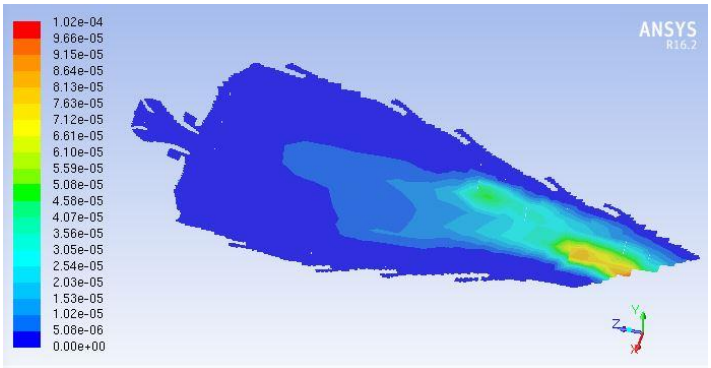

Figure E.9 Cross section contours of NO_x concentration [kg/kg] at 30% power, while burning Jet B.